EFFECT OF COATING MICROSTRUCTURE ON THE ELECTROCHEMICAL PROPERTIES OF CONTINUOUS GALVANIZED COATINGS ON PRESS HARDENED STEELS

EFFECT OF COATING MICROSTRUCTURE ON THE ELECTROCHEMICAL PROPERTIES OF CONTINUOUS GALVANIZED COATINGS ON PRESS HARDENED STEELS

By

CAITLIN ELIZABETH DEVER, B.Eng.

A Thesis
Submitted to the School of Graduate Studies
In Partial Fulfillment of the Requirements
For the Degree
Master of Applied Science

McMaster University

Masters of Applied Science (2018) McMaster University
(Materials Science & Engineering) Hamilton, Ontario

TITLE: Effect of Coating Microstructure on the Electrochemical Properties of Continuous Galvanized Coatings on Press Hardened Steels
AUTHOR: Caitlin Elizabeth Dever, B.Eng. (McMaster University)

SUPERVISOR: Dr. Joseph R. Kish and Dr. Joseph R. McDermid

NUMBER OF PAGES: xxv, 172

Abstract

In response to more stringent global CO_2 emissions, automotive manufacturers have increased the use of advanced high strength steels (AHSS). Ultra-high strength steels are often used within the body-in-white (BIW) for safety critical parts and structural reinforcements, such as roof rails and side impact beams. Currently, the most commonly used press hardened steel (PHS) grade for these applications is 22MnB5, with a typical composition of 0.22C-1.2Mn-0.25Si-0.005B (wt%). Automotive OEMs have expressed a desire to use Zn-based coatings as they are compatible with the current painting system and have the potential to provide robust cathodic protection. The steel blanks generally undergo direct hot press forming (DHPF) to achieve the necessary martensitic microstructure and target mechanical properties, but this presents challenges for Zn-coated 22MnB5. The adoption of Zn-based coatings within the automotive industry has been inhibited by the prospect of liquid metal embrittlement (LME) resulting from DHPF, as well as the desire to provide robust cathodic protection.

Previous literature has reported that a zinc ferrite (α-Fe(Zn)) coating with a global Zn content of at least 30 wt% will provide cathodic protection to the underlying substrate. The main goal of this work was to determine the microstructural evolution and electrochemical properties of galvanized (GI70 – 70 g/m^2/side) 22MnB5 substrates as a function of the annealing time at a typical austenization temperature of 900°C. It was found that the Zn-based coatings annealed at 700°C consisted to a mixture of small volume fraction of α-Fe(Zn) and Γ-Fe_3Zn_{10}. After heating to 900°C, the coating comprised varying

volume fractions of α-Fe(Zn) and Zn(Fe) liquid, which transformed to Γ-Fe_3Zn_{10} after solidification. The relative fraction of Γ-Fe_3Zn_{10} was found to decrease with increasing annealing time until the coating completely transformed to α-Fe(Zn) after annealing at 900°C for 240 s. GDOES results found that, when the sample was annealed at 900°C for 240 s, the global Zn content of the coating was less than 30 wt%. Coatings comprising varying fractions of Γ-Fe_3Zn_{10} were subjected to uniaxial tensile tests to determine how the coating microstructure affected the mechanical properties in comparison to the uncoated substrate material. It was found that the uncoated substrate material met the mechanical property requirements of $\sigma_{(UTS)min} \geq 1500$ MPa regardless of annealing time. However, $\sigma_{(UTS)}$ was found to decrease with increasing annealing times for the GI70 coated samples until the target mechanical properties were not met when the sample was annealed at 900°C for 180 s. This was attributed to increased coating thicknesses leading to a decrease in the martensitic cross-sectional area to support the load.

Furthermore, the coatings were subjected to a variety of electrochemical characterization techniques, including potentiodynamic and galvanostatic polarization scans, potentiostatic scans, and electrochemical noise tests. Potentiodynamic polarization scans indicated a higher driving force for cathodic protection when the coating contained some fraction of Γ-Fe_3Zn_{10}. Furthermore, a limiting current density for these samples was observed, demonstrating that Γ-Fe_3Zn_{10} corrodes at a slower rate in comparison to α-Fe(Zn). Galvanostatic polarization measurements indicated that, when the fraction of Γ-Fe_3Zn_{10} within the coating was below 15 vol%, the protective properties of the phase were not exhibited. XRD and TEM analysis revealed the formation of three corrosion products on the surface: simonkolleite, hydrozincite, and akaganeite. It was found that, when samples contained greater than 15 vol% Γ-Fe_3Zn_{10} in the coating, the predominant corrosion products were a combination of simonkolleite and hydrozincite. When the Γ-Fe_3Zn_{10} content was below this value, the dominant corrosion product was found to be akaganeite. Furthermore, substrate attack was observed on a sample annealed at 900°C for 420 s when the coating layer was intact, indicating that the α-Fe(Zn)-only containing coating obtained at this time does not provide cathodic protection.

Based upon the current results, it was determined that a minimum volume fraction of 15 vol% Γ-Fe_3Zn_{10} must be present within the coating layer to obtain robust cathodic protection. Furthermore, it was determined that the processing window to develop cathodically protective Zn-based coatings while mitigating LME is extremely narrow. This is a result of the fact that it is necessary for at least 15 vol% Γ-Fe_3Zn_{10} to be present within the coating microstructure at room temperature, which is liquid at the forming temperatures of 900°C. From the current findings, it was found that it is unlikely that a cathodically protective Zn-based coating can be obtained for DHPF steel parts using 22MnB5 as a substrate material. This is due to the high forming temperature resulting in liquefication of the coating and the rapid cooling rates necessary to achieve the target mechanical properties of $\sigma_{(UTS)min} \geq 1500$ MPa. Thus, it is recommended that the current substrate material be altered such that the part may be formed below the peritectic temperature of 782°C.

Acknowledgements

First and foremost, I would like to extend my deepest gratitude to my supervisors Dr. Joseph Kish and Dr. Joseph McDermid. Both have provided me with endless opportunities throughout my graduate studies. I sincerely appreciate their guidance, support, and encouragement. I am appreciative of their generosity, for they gave me the opportunity to present my work and meet industry members at international conferences. It was an honour and pleasure to be able to work with two talented professors on this research. I would also like to thank my supervisory committee member, Dr. Igor Zhitomirsky, for his constructive criticism and comments.

I would also like to thank many people for their training and technical knowledge. I would like to thank Chris Butcher (SEM training), Travis Casagrande (Auger training and FIB work), and Andreas Korinek (TEM work) from the Canadian Centre for Electron Microscopy, Victoria Jarvis (XRD training) and Dr. Jim Britten from the McMaster Analytical X-Ray Diffraction Facility, Doug Culley (GDOES) and Dr. Xiaogang Li from McMaster University, and Dr. Elizabeth McNally (ICP-OES) and Dr. Moisei Bruhis (technical support) from the Centre for Automotive Materials and Corrosion. I would also like to thank the members of my research group for their constant support and suggestions.

I would like to thank ArcelorMittal Dofasco for the provision of the steels used in this research, and the International Zinc Association – Galvanized Autobody Partnership (IZA-GAP) for their financial support.

Finally, I would like to thank my friends and family for their constant support.

Table of Contents

Table of Figures

Table of Tables

List of Abbreviations

AES	**A**uger **E**lectron **S**pectroscopy
AHSS	**A**dvanced **H**igh **S**trength **S**teel
AR	**A**s-**r**eceived
BSE	**B**ack**s**cattered **E**lectron
CE	**C**ounter **E**lectrode
CI	**C**onfidence **I**nterval
DHPF	**D**irect **H**ot **P**ress **F**ormed
DI	**Dei**onized water
EDS	**E**nergy **D**ispersive X-ray **S**pectroscopy
EELS	**E**lectron **E**nergy **L**oss **S**pectroscopy
FE	**F**ield **E**mission
FEG	**F**ield **E**mission **G**un
FIB	**F**ocused **I**on **B**eam
GA	**G**alv**a**nnealed
GI	**G**alvan**i**zed
GDOES	**G**low **D**ischarge **O**ptical **E**mission **S**pectroscopy
ICP-OES	**I**nductively **C**oupled **P**lasma – **O**ptical **E**mission **S**pectroscopy

LME	**L**iquid **M**etal **E**mbrittlement
OCP	**O**pen **C**ircuit **P**otential
OP-S	Active **O**xide **P**olishing **S**uspension, Colloidal Silica
PAT	**P**eak **A**nnealing **T**emperature
PHS	**P**ress **H**ardened **S**teel
RD	**R**olling **D**irection
SAM	**S**canning **A**uger **M**icroscope
SCE	**S**aturated **C**alomel **E**lectrode
SE	**S**econdary **E**lectron
SEM	**S**canning **E**lectron **M**icroscopy
TEM	**T**ransmission **E**lectron **M**icroscopy
TD	**T**ransverse **D**irection
UHSS	**U**ltra-**H**igh **S**trength **S**teel
WE	**W**orking **E**lectrode
XRD^2	Two-dimensional **X-r**ay **D**iffraction

List of Symbols

°C	Degrees Celsius
α-Fe(Zn)	Zinc ferrite
αFe	Ferrite
Å	Angstrom
A_0	Initial cross-sectional area
at%	Atomic percent
cm	Centimetre
ε	Engineering strain
E	Electrochemical potential
E_{corr}	Corrosion potential
E_{gc}	Corrosion potential for the galvanic couple
eV	Electron volt
F	Faraday’s constant, 96485 C/mol; Force
γFe	Austenite
ΔG	Gibbs free energy change
g	Grams
h	Hours

I	Current
i	Current density
i_{gc}	Current density for the galvanic couple
kN	Kilonewton
kPa	Kilopascals
keV/kV	Kiloelectron volts, Kilovolts
ΔL	Change in gauge length
L_0	Initial gauge length
μA	Microamps
μm	Micrometre/micron
m	Metre
mA	Milliamps
MPa	Megapascals
mV	Millivolts
N	Newton
n	Exchanged electrons
nm	Nanometre
Pa	Pascals
pH	Potential of hydrogen
σ	Engineering stress
s	Seconds

θ	Diffraction angle
TE	Total Elongation
UTS	Ultimate Tensile Strength
V	Volts
wt%	Weight percent

1 INTRODUCTION

1.1 The use of press hardened steels for automotive applications

The increasing demands for vehicle light-weighting while maintaining or improving passenger safety have increased the usage of ultra-high strength steels (UHSS) within the body-in-white (BIW). Due to their ultra-high strengths, UHSSs are used for structural reinforcement and anti-intrusion parts, such as B-pillars and roof rails [1, 2]. Typically, to economically fabricate complex shapes while producing high strengths, the parts are often direct hot-press formed (DHPF). Subsequent to DHPF, PHSs typically have ultimate tensile strengths (UTS) of at least 1500 MPa and total elongations (TE) of 5-6% [1, 2]. The most commonly used grade for the DHPF process is 22MnB5, with a standard composition of 0.22C-1.2Mn-0.25Si-0.005B (wt%) [2, 3]. Austenitization of these substrates is performed in an ambient atmospheric furnace at temperatures between 850°C-950°C. Following austenization, the parts are simultaneously stamped and die quenched with cooling rates in excess of 75°C/s [4]. The resultant substrate microstructure consists of lath martensite with small volume fractions of ferrite.

1.2 Development of corrosion resistant parts

Similar to other low C alloys, the 22MnB5 grade will corrode easily to red rust during typical environmental exposures, thereby decreasing its effective service life. For usage in automotive applications, corrosion resistance is essential to protect the exposed steel from aqueous corrosion while maintaining structural integrity. Metallic coatings are frequently used to obtain corrosion protection through the use of barrier type protection and cathodic protection. Currently, the Al-(9-11 wt%)Si system applied at 675°C has been the dominant continuously applied metallic coating [2]. During the DHPF process, the liquefied Al-Si coating reacts with the substrate to form a series of Fe-Al-Si intermetallics. Growing outward from the substrate, these include αFe(Al,Si) (Al and Si containing ferrite), Fe_2SiAl_2, $FeAl_2/Fe_2Al_5$ and Al_2O_3 [2, 5]. As these Fe-Al intermetallics are brittle and have been reported to have low forming limits, the coating forms microcracks during deformation [6, 7]. As the transformed Al-Si coating does not provide cathodic protection and only offers barrier corrosion protection, corrosion performance is severely decreased as a result of the microcracks [2, 4, 8].

Automotive companies have expressed strong interest in Zn-based coatings for DHPF steels due to the possibility of providing robust cathodic protection, good weldability, and compatibility with current paint systems [2]. Studies have been performed on the development of Zn-based coatings, such as Fe-Zn coatings [2, 8, 9], Zn-Al-Mg coatings [10, 11], and electrodeposited Zn-Ni coatings [12, 13], all of which have been reported to provide cathodic protection for the steel substrate [2, 4, 8, 11, 13]. However, the wide-spread usage of DHPF Zn-based coatings has been inhibited due to a number of factors [14]. In particular, these include microcracking during DHPF processes, the prospect of liquid metal embrittlement (LME), and questions arising in regards to the robustness of the provided cathodic protection [2]. These issues are resultant of the austentization temperatures between 850°C-950°C necessary for the 22MnB5 substrate and the requirement for extremely high cooling rates from the DHPF temperature to form the desired fully martensitic microstructure. At these austentization temperatures, the Zn coating goes through a peritectic reation at 782°C, separating into a high Zn-content Zn(Fe) liquid and a zinc-containing ferrite phase, commonly referred to a zinc-ferrite (α-Fe(Zn)) in the literature. When DHPF is performed above the peritectic temperature of 782°C, LME results from the presence of the Zn(Fe) liquid [2, 9, 15, 16].

It has often been stated that α-Fe(Zn) coatings that contain a minimum Zn content of 30 wt% are capable of providing cathodic protection [2, 4, 8], however, a robust processing window has yet to be established. In addition, the cathodic protection potential of high Zn-content α-Fe(Zn) coatings has yet to be widely accepted.

The main focus of this thesis was to assess how the coating microstructure evolved as a function of annealing time at 900°C, and how it affected the electrochemical properties with a focus on the potential for providing robust cathodic protection. Furthermore, the different coating morphologies were subjected to tensile testing to determine if they could, in fact, meet the required mechanical target properties of $\sigma_{(UTS)} \geq 1500$ MPa [1, 2]. Finally, the industrial objective of this thesis was to determine a processing window for DHPF whereby a robust cathodically protective coating could be obtained while mitigating LME.

2 LITERATURE REVIEW

2.1 Ultra-high strength steels in automotive applications

In response to more stringent global emission standards, advanced high strength steels (AHSS) have been developed to reduce CO_2 emissions by vehicle light-weighting without compromising passenger safety. Throughout the years, the fraction of AHSS in automotive applications has increased substantially. It has been reported that approximately 65% of the structural components used in the body-in-white (BIW) of the 2016 Chevrolet Malibu is comprised of AHSS, with 7% attributed to ultra-high strength steels (UHSS) [17], as seen in Figure 2.1 [18]. UHSS are typically used within the body-in-white (BIW) as structural reinforcements and anti-intrusion parts as they exhibit extremely high strengths [2], as seen in Figure 2.1 (b) [18].

To simultaneously achieve the high strengths and complex shapes necessary for safety related applications, UHSS undergo a process known as press forming or hot stamping. Currently, the most commonly used press hardened steel (PHS) grade for these applications is the 22MnB5 family of alloys with a standard composition of 0.22C-1.2Mn-0.25Si-0.005B (wt%). 22MnB5 is well suited to direct hot press forming (DHPF) due to the addition of B, which acts to harden the steel by retarding ferritic growth [2, 19]. Prior to forming, the microstructure is composed of a mixture of ferrite and pearlite. The alloys are austenitized at 850-950°C in a non-protective atmosphere furnace, after which the parts are simultaneously stamped and quenched with water-cooled dies to produce a fully lath martensitic microstructure. Some literature has reported that cooling rates of −25°C/s are sufficient for this transformation to occur [1, 2], however, it has been found that in order to avoid the bainitic transformation in deformed areas, cooling rates of at least −75°C/s are necessary [4]. Subsequent to stamping, the ultimate tensile strength (UTS) has been reported to be in excess of 1500 MPa [1, 2].

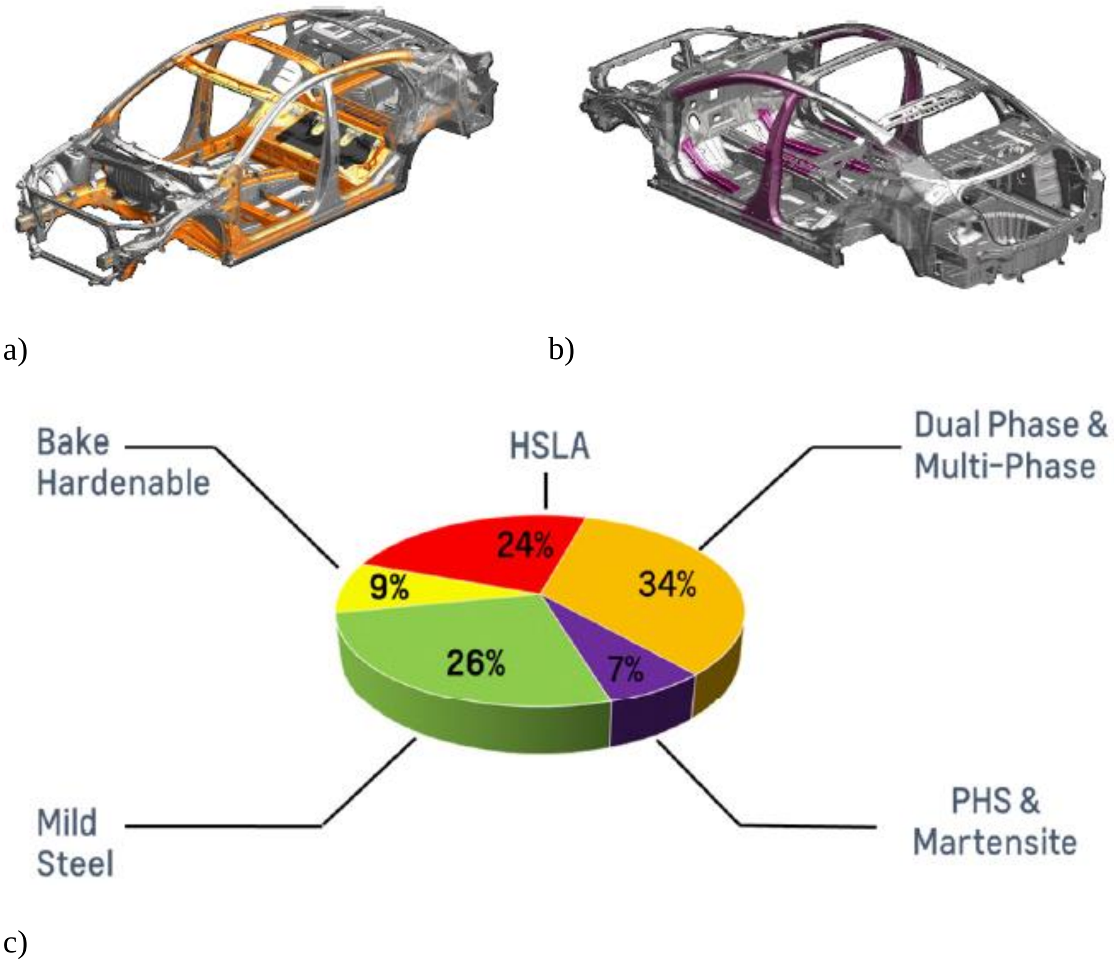

Figure 2.1: AHSS applications within the 2016 Chevrolet Malibu BIW including a) dual and multi phase, b) PHS and martensitic steels, and c) usage weight [18].

Owing to harsh road environments, these parts are extremely susceptible to corrosion. At present, the most commonly used metallic coating for corrosion protection on PHS is the Usibor® Al-(9-11wt%)Si; however, automotive manufacturers have expressed an interest in Zn-based coatings over the Al-Si coatings for a number of reasons. Al-Si coatings often suffer from cracking and interfacial debonding during forming due to their low forming limits [7]. These cracks are detrimental to the corrosion resistance as Al-Si coatings only provide barrier type protection, resultant of its electrochemical properties being in close proximity to that of the substrate material [2, 4].

Zn-based metallic coatings, in contrast, may protect the underlying substrate by one of two methods: barrier protection and galvanic protection [14]. With barrier protection, the coating layer acts to isolate the substrate from the corrosive environment. With galvanic protection, the Zn acts as a sacrificial anode for the steel substrate and preferentially corrodes even with small surface defects or damage (e.g. stone chips), thereby protecting the steel despite being damaged [20]. Corrosion protection is of an utmost importance for automotive applications, particularly for parts that come in contact with the external atmosphere. Continuous galvanizing is the most widely practiced means of providing metallic coating protection to PHS for both the Zn and Al-Si systems.

2.2 Continuous galvanizing

The Sendzimir-type continuous galvanizing process has been described by Marder [21], and designed process schematic by Silva [22] can be seen in Figure 2.2. The sheet is pre-cleaned using a 2% NaOH alkali solution to remove organic surface contaminants such as oils or other organic debris introduced during rolling. Often, this is followed by electrolytic cleaning to remove soils that are more tightly adhered to the surface such as iron fines and other non-organic debris. The sheet is then rinsed and dried using air to mitigate any remaining moisture being carried into the continuous annealing furnace. Once all pre-cleaning steps have been completed, the sheet enters an annealing furnace between 500-760°C, which has two functions: i) to heat treat the steel sheets such that the desired mechanical properties and microstructures can be achieved, and ii) oxide reduction. The iron oxides present on the steel surface are reduced using a N_2-(5-20%)H_2 atmosphere that uses a set dew point or oxygen partial pressure, ensuring that metallic iron comes in contact with the bath. The sheet is subsequently cooled to approximately 460°C so that it will not affect the bath temperature during dipping. Typical galvanizing bath compositions have dissolved Al contents between 0.15 and 0.2 wt%. Due to the addition of Al, an interfacial layer of $Fe_2Al_5Zn_x$ is formed at the steel/coating interface [23, 24]. This layer, often termed the inhibition layer by industry, delays the formation of brittle Fe-Zn intermetallics by providing a diffusion barrier between the bath and the substrate. For line speeds between 100-125 m/min, the dipping time generally ranges from 2 – 4 s [25]. After dipping, the sheet is removed from the bath and the coating weight is controlled through the use of air knives or gas wiping dies, which blow air or nitrogen. In the case of galvanized (GI) coatings, the steel is cooled and the zinc coating solidified. For galvannealed (GA) coatings, the steel is annealed subsequent to dipping to transform the coating layer into

Fe-Zn intermetallics. The present study will focus solely on GI coated PHS. After dipping, the sheet undergoes several quality control steps, including temper rolling, roller levelling, chromating/pre-phosphating, recoiling, and cutting.

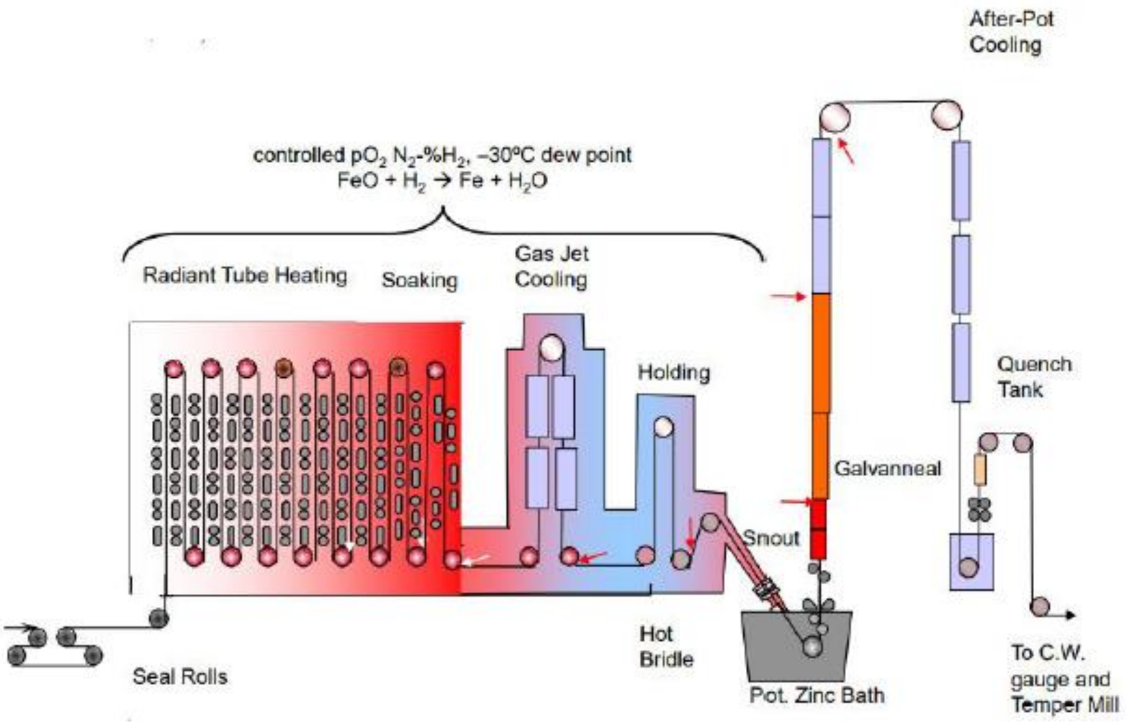

Figure 2.2: Schematic of the Sendzimir continuous galvanizing line [22].

2.3 Direct hot press forming

Two stamping processes have been developed for the simultaneous forming and quenching of metallic-coated PHS, as outlined in Figure 2.3 [2]: the direct and indirect press hardening processes. In the indirect process, the metallic coated PHS is formed to 90-95% of the final shape prior to heating. The pre-formed part is then heated to the austentizing temperature in the die and then quenched. Forming at low temperatures prevents liquid metal embrittlement (LME) from occurring. However, indirectly formed parts have several drawbacks, including increased springback and higher production costs due to the increased number of steps [2, 9, 26]. In the direct press hardening process, the metallic coated sheet is austenitized between 850°C-950°C and transferred immediately to the press, where it is simultaneously formed and quenched with cooling rates in excess of −25°C/s [1, 2] to a temperature of 200°C to avoid martensite tempering. However, other research has indicated that cooling rates must be at least −75°C/s to avoid bainitic transformations within the deformed areas [4]. After forming, the part predominantly consists of martensite with trace amounts of ferrite, and has an UTS of at least 1500 MPa. During DHPF, an ambient atmosphere is employed the furnace to form a mixed external ZnO-Al_2O_3 oxide on the coating which prevents Zn sublimation from occurring. This surface oxide is removed using sandblasting to improve contact resistance for spot welding [2].

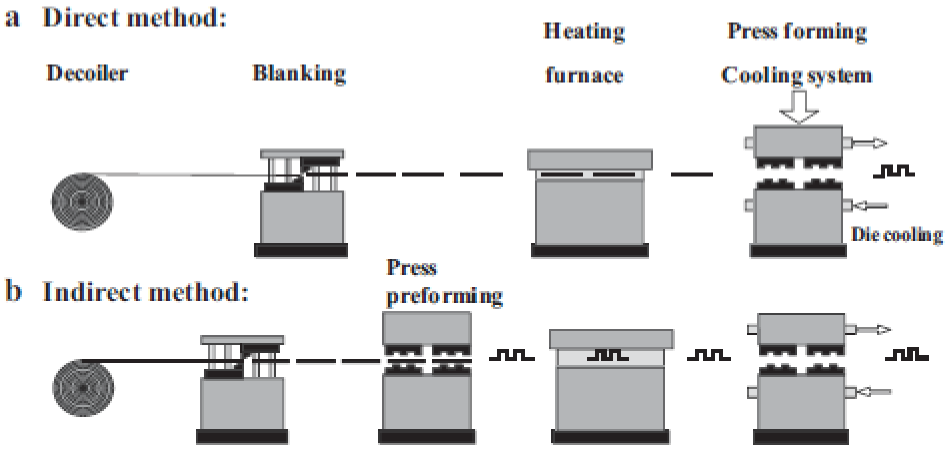

Figure 2.3: Schematic of the a) direct and b) indirect press forming methods [2].

2.4 Al-Si coatings

Currently, the Usibor® Al-(9-11wt%)Si is the most commonly used metallic coating for corrosion protection of hot stamped parts [2], which has been reported to have a melting point of 575°C [27]. Al-based coatings have proven to be an attractive coating option due to the low density, resistance to high temperature oxidation, good mechanical properties, and passivation in most environments [28]. During DHPF, the coating liquefies and reacts with the substrate material through outward diffusion of Fe, forming Al-Si-Fe intermetallics [29]. These Al-Si-Fe intermetallics, forming outward from the substrate, are as follows: αFe(Al,Si) (ferrite enriched with Al and Si in solid solution), Fe_2SiAl_2, $FeAl_2$/Fe_2Al_5 and Al_2O_3 [2, 5]. These layers can be seen in Figure 2.4 [2]. The formation of these intermetallics increases the melting point of the coating, resulting in a fully solid coating during forming [30]. Due to the reduced formability of the Al-Si-Fe intermetallics in comparison to the substrate material, the coating is prone to microcracking during deformation processes [6, 7], as seen in Figure 2.4 [2]. Previous literature has reported that the electrochemical properties of the Al-Si-Fe coating are in close proximity to that of the substrate material [2, 4, 8]. Electrochemical tests in a NaCl electrolyte, conducted by Maki et al. [31], found that Fe_2Al_5 preferentially corroded during the test as its electrochemical properties were slightly more active than the substrate. However, it was found that the electrochemical properties of the remaining coating were not significantly different from the substrate, and as a result Al-Si coatings obtained during DHPF are incapable of providing cathodic protection [31]. Thus, the microcracks that form during forming comprise the offered barrier protection, allowing for oxidation and corrosion of the substrate [7]. Furthermore, any uncoated regions of the substrate (ie. cut edges) would be susceptible to corrosion attack [2].

Work by Dosdat et al. [4] compared the corrosion resistance of GI and Al-Si coatings after hot stamping. It was found that the blister width for Al-Si coatings was larger than that found for GI coatings. Furthermore, the cut-edge corrosion resistance of Al-Si coatings was found to be poor in comparison to the GI coatings, owing to the lack of cathodic protection [4]. Thus, it can be stated that Al-Si coatings are vastly inferior to GI coatings after press hardening in regards to the offered corrosion protection when defects are present, ie. stone chips.

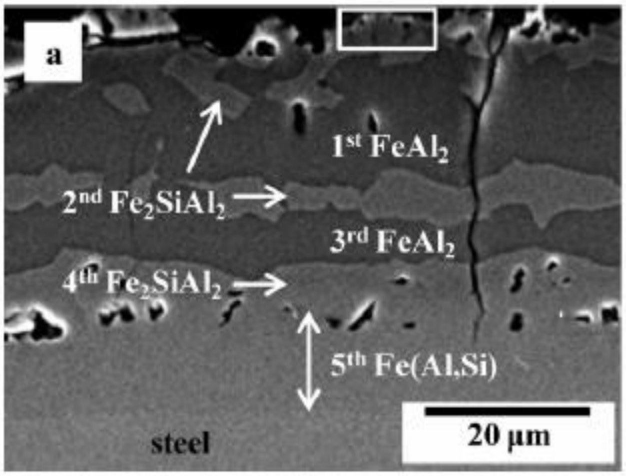

Figure 2.4: Cross-sectional SEM image of an Al-(9-11 wt%)Si coating annealed at 930°C for 300 s in air [2].

2.5 The microstructural development of Zn-based PHS coatings

As the corrosion resistance of the Al-Si coatings is comprised due to the formation of cracks during deformation processes, automotive manufacturers have expressed an interest in using Zn-based coatings instead as it has the potential to provide cathodic protection. The Fe-Zn phase diagram can be seen in Figure 2.5 [32]. The presence of the $Fe_2Al_5Zn_x$ interfacial layer in galvanized coatings delays the formation of the Fe-Zn intermetallics during dipping [23, 24]. As a result, the coating layer consists solely of metallic η-Zn [33]. Prior to undergoing DHPF, GI70 coatings have been found to have a typical thickness of 10 μm and consist of large grains [13]. Similar to the Al-Si system, the Zn coating liquefies during DHPF and reacts with the substrate to form a series of Fe-Zn intermetallics. Annealing of galvanized coatings at temperatures lower than 750°C gives rise to the formation of Fe-Zn intermetallics, including ζ-$FeZn_{13}$, δ-$FeZn_{10}$ and Γ-Fe_3Zn_{10}, as seen in Figure 2.5. While the phases that form can be predicted thermodynamically, atomic diffusion and subsequently kinetics must also be considered [33, 34].

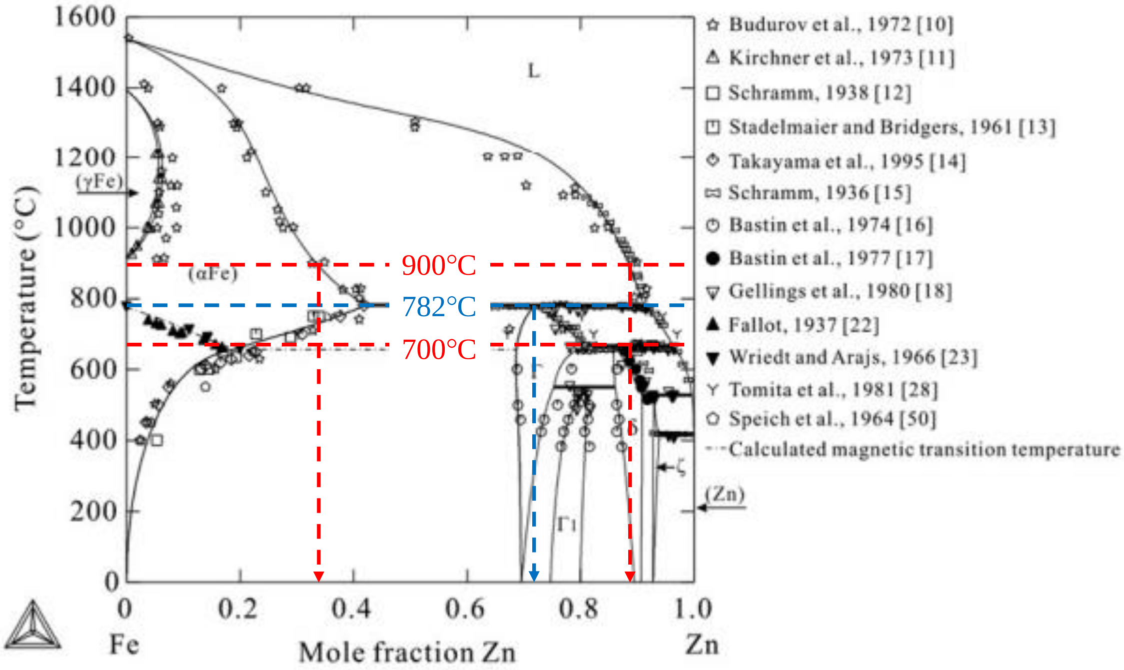

Figure 2.5: Fe-Zn phase diagram expressed in mole fraction [32].

Figure 2.6 [35] depicts the formation of Fe-Zn intermetallics on a GI70 as the annealing temperature is increased from 400°C to 900°C. Once the sample reached the annealing temperature, it was quenched immediately in water between steel plates. Under 500°C, the coating was found to contain η-Zn. The beginning of inhibition breakdown can be observed at 400°C, and near complete transformation of the coating at 450°C (Figure 2.6). At 500°C (Figure 2.6), both ζ-$FeZn_{13}$ and δ-$FeZn_{10}$ were detected; the $Fe_2Al_5Zn_x$ interfacial layer was not detected, indicating that it had broken down during the formation of Fe-Zn intermetallics. Once the steel reached 550°C (Figure 2.6), the coating had completely transformed to δ-$FeZn_{10}$. At 600°C and 650°C, both δ-$FeZn_{10}$ and Γ_1-Fe_5Zn_{21} were present (Figure 2.6). Once the sample had reached 700°C (Figure 2.6), the δ-$FeZn_{10}$ and Γ_1-Fe_5Zn_{21} intermetallics had completely transformed into Γ-Fe_3Zn_{10}. Thus, it can be stated that prior to passing through the peritectic temperature at 782°C [32], the coating has completely transformed into Γ-Fe_3Zn_{10}. Furthermore, the results indicated that δ-$FeZn_{10}$ was present beyond its thermodynamic stability, as determined in Figure 2.5 [32]. At 750°C and above (Figure 2.6), the coating layer consisted of Γ-Fe_3Zn_{10} and a high Zn-content ferrite, henceforth referred to as zinc ferrite (α-Fe(Zn)), with increasing annealing temperatures and holding times resulting in a decrease in the amount of Γ-Fe_3Zn_{10} present. As expected, the phases growing outward have an increasing Zn content. During DHPF, the coated sheet is heated above the peritectic temperature of 782°C to an austenitizing temperature between 850°C-950°C (Figure 2.6). Investigation of the Fe-Zn phase diagram, depicted in Figure 2.5 [32], indicates that in this austenitizing temperature range, α-Fe(Zn) is in equilibrium with a Zn-rich Zn(Fe) liquid. Rapid quenching of the blank to produce a fully martensitic microstructure results in solidification of the coating, transforming any residual liquid into Γ-Fe_3Zn_{10} as it passes through the peritectic point. As such, this phase forms islands within the coating layer and is present at the surface. Due to diffusional growth, α-Fe(Zn) grows inward until no liquid is present, creating a compositional gradient towards the steel/coating interface [36, 37].

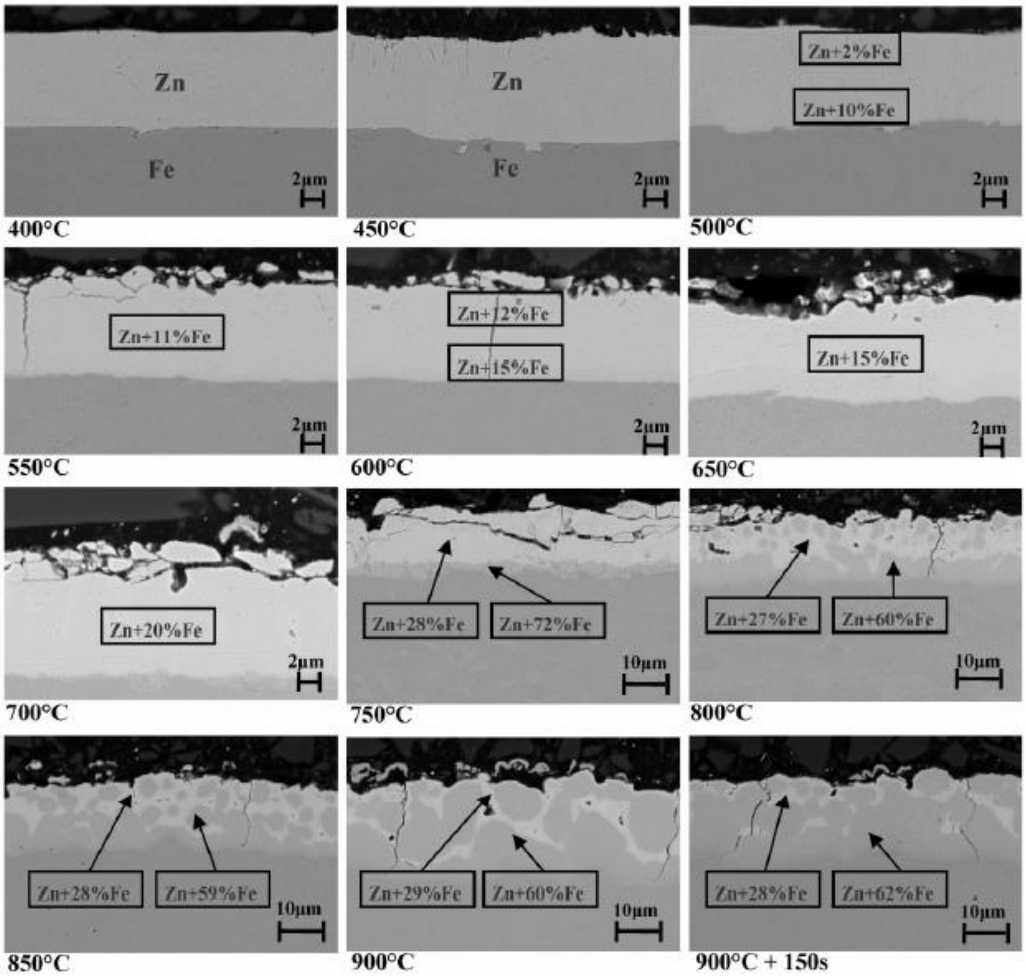

Figure 2.6: Cross-sectional view of GI70 coated steel undergoing a PHS annealing cycle [35].

Figure 2.7 displays a semi-infinite diffusion model with no Zn flux across a fixed surface, S_2. The speed of the interface between the growing α-Fe(Zn) phase and the Zn-rich austenite phase - γ-Fe(Zn) at S_1 can be calculated by equation (2.1) [37]. In this model, D_{Zn}^{γ} and D_{Zn}^{α} are the effective diffusion coefficients of Zn into the austenitic substrate and α-Fe(Zn), respectively, C_{Zn}^{γ} and C_{Zn}^{α} are the concentrations of Zn within the austenitic substrate and α-Fe(Zn), and $C_{Zn}^{\alpha/\gamma}$ and $C_{Zn}^{\gamma/\alpha}$ are the equilibrium conditions on either side of the coating/substrate interface. The concentration gradients, $\frac{\partial C_{Zn}^{\gamma}}{\partial x}$ and $\frac{\partial C_{Zn}^{\alpha}}{\partial x}$, were determined through the use of Fick's second law [38], as outlined in equation (2.2). *C* represents the Zn concentration, *D* is the effective diffusion coefficient of Zn, *t* is time, and *x* represents the spacial coordinate.

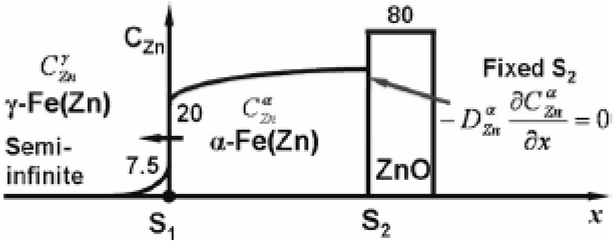

Figure 2.7: Semi-infinite Zn diffusion model at 900°C [37].

$$v\big|_{x=S_1} = \frac{D_{Zn}^{\gamma}\frac{\partial C_{Zn}^{\gamma}}{\partial x} - D_{Zn}^{\alpha}\frac{\partial C_{Zn}^{\alpha}}{\partial x}}{C_{Zn}^{\alpha/\gamma} - C_{Zn}^{\gamma/\alpha}} \tag{2.1}$$

$$\frac{\partial C}{\partial t} = D\frac{\partial C}{\partial x^2} \tag{2.2}$$

It has been found by Janik et al. that, as annealing times are increased, the amount of Zn content within the phase decreases [37]. This is in accordance with the above model. This can be seen in Figure 2.6 [35], where the sample annealed at 900°C for 150 s had an increased Fe content within α-Fe(Zn) in comparison to the sample that reached 900°C and was immediately quenched.

2.6 Press hardened galvanized steels annealed at 900°C

The high strength of PHS arises from the fully lath martensitic microstructure, which is achieved by annealing the galvanized sheets at 850°C-950°C and rapidly quenching. When annealing times are short, the coatings consist of a mixture of α-Fe(Zn) with some Γ-Fe_3Zn_{10}. Figure 2.8 depicts a typical cross-sectional view after press hardening a 22MnB5 steel with an initial GI70 coating annealed at 910°C for 360 s. Lighter areas within the coating correspond to Γ-Fe_3Zn_{10}, whereas the darker portions correspond to α-Fe(Zn). As annealing times increased, the thickness of the coating increased as a result of the counter-diffusion of Zn into the substrate [2, 13, 36, 37]. Furthermore, an increase in annealing time resulted in an eventual consumption of the Zn(Fe) liquid phase until no Γ-Fe_3Zn_{10} was present within the coating layer at room temperature. It was also found that further annealing at 910°C resulted in an enrichment of Fe within α-Fe(Zn) [13, 37].

During austentization at 910°C, a heterogenous oxide layer containing Al_2O_3, ZnO, and MnO has been found to form on the surface of the coating. This oxide layer was found to inhibit further evaporation of Zn during high temperature annealing [39]. The formation of Al_2O_3 has been attributed to the outward flux of dissolved Al from the interfacial layer, $Fe_2Al_5Zn_x$ [35], while the formation of MnO results from the outward lattice diffusion of Mn from the substrate [40, 41]. Moreover, these oxides prevent contact between the liquid

Zn coating and the dies during DHPF [2]. Figure 2.9 presents a typical low angle XRD spectrum of the oxide layers that formed as a result of annealing at 910°C. It should be noted that the Al_2O_3 fragments at higher temperatures due to the presence of Zn(Fe) liquid, and as the layer is thin and discontinuous, is not typically detected using XRD techniques [35, 42].

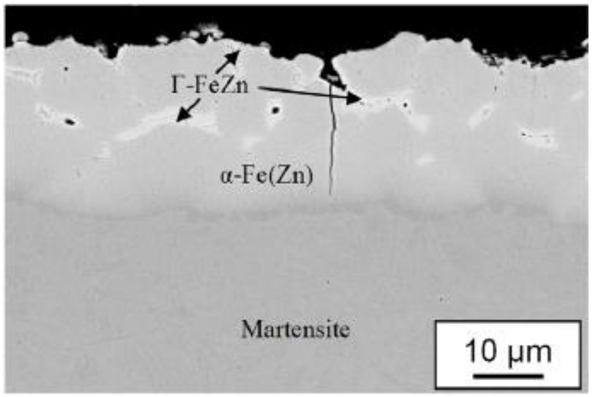

Figure 2.8: Cross-sectional SEM image of GI70 coating annealed at 910°C for 360 s after press hardening [43].

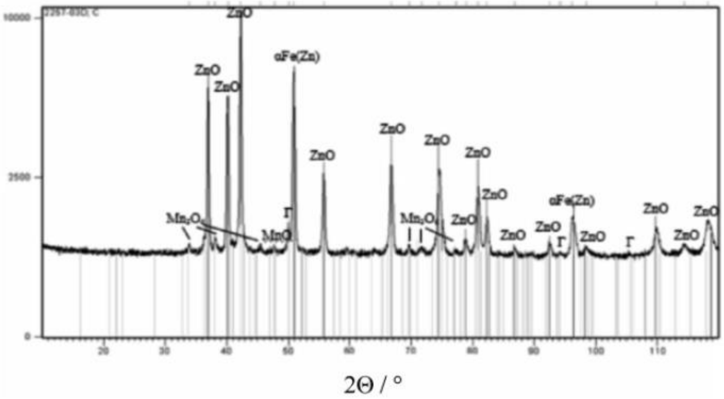

Figure 2.9: Low angle XRD spectrum of press hardened GI70 coated 22MnB5 at 910°C [35].

2.7 Cracking within the Zn layer

Cracking within Zn coatings can result due to many reasons, such as differing thermal expansions of the coating and substrate, pre-cracking as a result of friction or recently nucleated microcracks, liquid Zn penetrating the coating and resulting in LME, or enrichment of Zn on austenite grain boundaries that results in embrittlement [37]. Formability also plays a role in the cracking behaviour, and is influenced by texture, grain size, surface roughness, coating hardness, and the alloying elements within the Zn [44].

Perhaps the most detrimental of these cracking types is LME, which occurs during the application of stress to austenitized Zn-based PHS at higher temperatures [2, 36]. During high temperature forming processes, the liquid Zn penetrates the austenite grain boundaries, weakening the cohesion between grains and resulting in brittle intergranular fracture [9, 45]. The crack severity has been found by De Cooman et al. to be dependent on the strain path, friction during forming, and tensile stresses [36]. Tensile tests performed in the presence of a liquid Zn-based coating have found a decrease in both the fracture stress and deformation, as seen in Figure 2.10. Furthermore, LME has found to be linked to the steel grade used as a substrate material, and has been theorized to be due to the presence of C at the grain boundaries [36]. Work by Cho et al. [45] has found that the liquid Zn that penetrates the grain boundaries acts as a ferrite stabilizer. Due to the reduction in strength and strain hardening of ferrite in comparison to austenite, this often causes intergranular cracks to form.

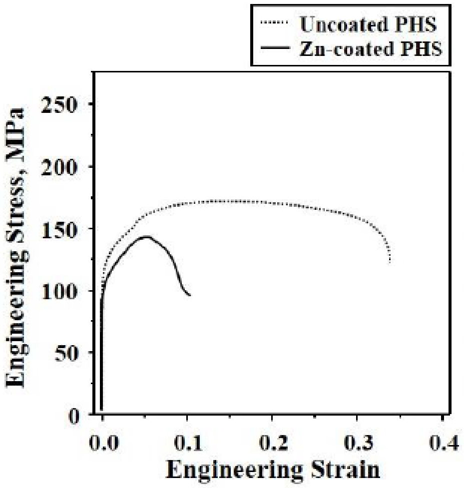

Figure 2.10: Influence of LME on the mechanical properties of a Zn-coated 22MnB5 PHS at 850°C [36].

There are currently three main models describing the mechanism behind LME, as seen in Figure 2.11 [36]: brittle fracture propagation, dislocation activity, and grain boundary diffusion. The first two assume that the crack-tip has already been wetted by the embrittling metal, while the third considers the fact that stress-assisted diffusion may also play a role in embrittlement [46]. The Rostoker-Rehbinder, Stoloff-Johnson-Westwood-Kamdar, and Robertson-Glickman models all describe a type of brittle crack tip fracture. The Rostoker-Rehbinder [47, 48] model states that the surface energy of the non-embrittling metal is reduced by adhesion of the embrittling metal, thereby decreasing fracture strength. In the Stoloff-Johnson-Westwood-Kamdar model [49, 50], accumulation of liquid atoms ahead of the crack tip reduce the cohesive strength, allowing for crack propagation. The Robertson-Glickman model [51] assumes a stress-assisted dissolution, such that the base metal at the crack tip dissolves into the liquid metal. The Lynch, Rehbinder-Popovich, and Hancock-Ives models describe the dislocation activity at the crack tip. In the Lynch model [52], adsorption of the embrittling metal decreases the stress associated with dislocation movements, facilitating plastic deformation through dislocation nucleation and motion. The Rehbinder-Popovich model [53] assumes plastic deformation at the crack tip by reducing the surface energy between the embrittling metal and base metal. In the Hancock-Ives model [54], it is assumed that the plastic deformation results in dislocation pile-ups ahead of the crack tip, which interact with the embrittling metal to reduce the fracture stress. Finally, the Krishtal-Gordon-An and Rabkin models focus on the grain boundary properties. The Krishtal-Gordon-An model [55, 56] states that the grain boundaries of the base metal are embrittled by stress-induced diffusion of the liquid atoms along grain boundaries. The Rabkin model [57] states that the Kirkendall effect induces high stresses at the grain boundaries such that grain boundary cracks nucleate, allowing for the embrittling metal to penetrate along the cracks. However, no model has yet to be universally accepted, indicating that the mechanism by which LME occurs is not fully understood.

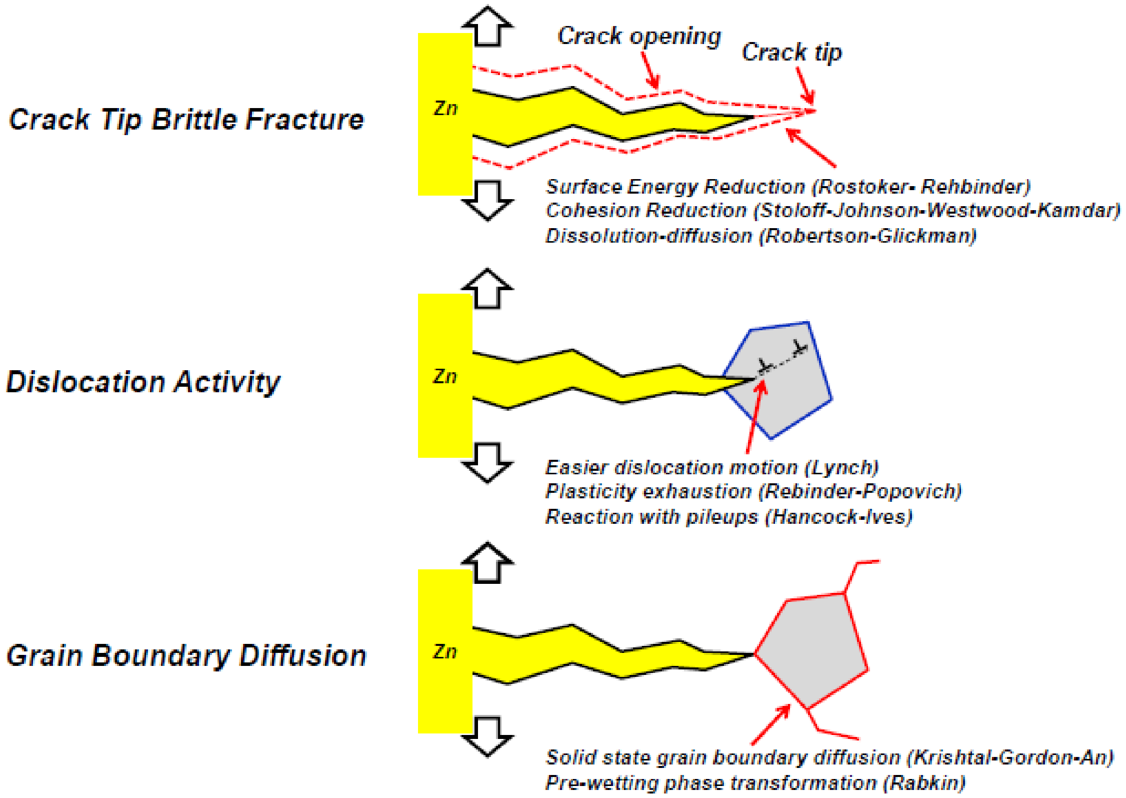

Figure 2.11: Models describing the LME mechanism [36].

Work by Beal et al. [58] found a significant loss in ductility during testing between 775°C-950°C, which, in accordance to the phase diagram (Figure 2.5) [32], is within the liquid Zn region. Further work by Lee et al. [59] found that a sample tested at 700°C did not crack, a result of the fact that no liquid was present during deformation to cause LME. Similar to the work by Beal et al. [58], however, Lee et al. [59] observed a reduction in ductility and cracking within the Zn layer and substrate when the sample was tested at 850°C. Additional experiments conducted by Lee et al. [60] reported the presence of Γ-Fe_3Zn_{10} at the crack tip at room temperature, indicative of the liquid phase at high temperatures. Kang et al. [46] found their results to be compatible with two of the models expressed in Figure 2.11: crack tip brittle fracture (Stoloff-Johnson-Westwood-Kamdar) and grain boundary diffusion (Krishtal-Gordon-An). They proposed two mechanisms for LME, as seen in Figure 2.12. In the first mechanism, the formed Γ-Fe_3Zn_{10} liquefies when heated above the peritectic temperature (782°C), and through stress-induced solid-state diffusion, penetrates along the austenitic grain boundaries of the base metal. The centre of the Zn diffusion profile becomes enriched in Zn, while the Zn content at the penetration tip remains low. Soon, maximum solubility within the austenitic grains is achieved, resulting in the formation of liquid Zn islands within the grain boundary. The presence of the liquid weakens the cohesion between grains, allowing for the propagation of cracks. In the second mechanism, liquid Zn percolation along the austenitic grain boundaries occurs, allowing for liquid Zn to penetrate far into the matrix. Solid-state Zn diffusion also occurs, allowing for enrichment of Zn in neighbouring grains. However, as the microstructure at room temperature would be identical for the two mechanisms, it is impossible to differentiate between which mechanism results in LME [46].

To avoid LME, the literature has suggested forming at temperatures below the peritectic point at 782°C as the coating would be solid and consist solely of Γ-Fe_3Zn_{10} [2, 62]. At the time, however, no steel grade compatible with the DHPF process existed that could be austenitized at these temperatures to achieve an UTS of at least 1500 MPa [1, 2]. The indirect process may be used, but this incurs higher production costs [9, 26]. Another proposed suggestion has been increased annealing times to fully transform the coating layer to α-Fe(Zn), thereby avoiding the presence of Zn(Fe) liquid during forming [36, 45, 59]. However, this proposition has several drawbacks. As the Fe content within α-Fe(Zn) is higher than other Fe-Zn intermetallics, the offered cathodic protection may be reduced [43], as discussed in §2.9. Moreover, microcracking of both the substrate and α-Fe(Zn) have been observed in the absence of Zn(Fe) liquid at the forming temperatures [37]. These cracks penetrate intergranularly through α-Fe(Zn), but are arrested once they reach the substrate [61].

Figure 2.13 depicts the appearance of cracks as annealing times increase, as well as the penetration depth as a function of Zn content. Janik et al. [37] determined that, since the entire coating was solid and there was no liquid Zn present, the microcracks could be associated with friction due to drawing. In addition, it was found that increasing annealing times resulted in a decrease in crack depth, as well as crack blunting. Figure 2.13 (c) also indicates that a decrease in the Zn content within α-Fe(Zn) resulted in an overall decrease in the microcrack depth.

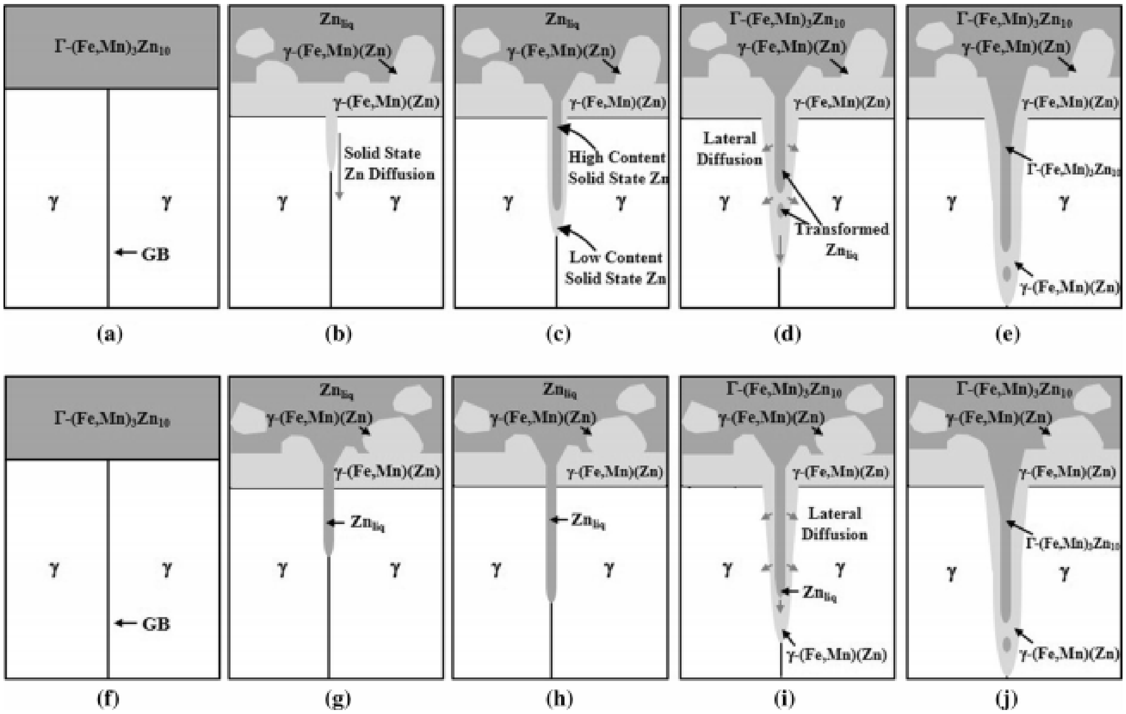

Figure 2.12: Proposed LME mechanisms for (a-e) of solid-state Zn diffusion and (f-j) of penetration of liquid Zn. (a) Low temperature microstructure of reacted coating layer and austenite grains. (b) Stress-assisted solid-state Zn diffusion down austenite grain boundaries. (c) Penetration of Zn by diffusion, whereby the centre of the diffusion zone is enriched in Zn. (d) The maximum solubility of Zn within austenite occurs, resulting in the formation of liquid Zn. (e) Cooled microstructure shows distribution of liquid Zn in the form of Γ-Fe_3Zn_{10}. (f) Low temperature microstructure of reacted coating layer and austenite grains. (g) Penetration of liquid Zn along austenite grain boundaries. (h) Further penetration of liquid Zn along grain boundaries. (i) Diffusion of Zn laterally through solid-state diffusion into neighbouring grains. (j) Cooled microstructure shows distribution of liquid Zn in the form of Γ-Fe_3Zn_{10} [46].

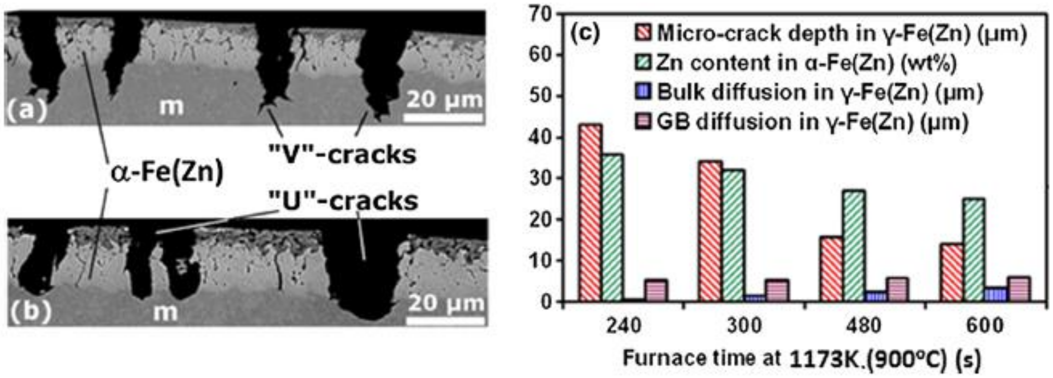

Figure 2.13: Cracking within a drawn side wall a) 240s annealing, b) 600s annealing, c) microcrack depth vs. Zn content [37].

Janik et al. [37] also found the presence of enriched Zn pockets, which may have influenced the propagation of microcracks; however, no Zn was detected at the surface of the cracks. It is believed that the Zn-enriched pockets result from areas where Γ-Fe_3Zn_{10} transformed into α-Fe(Zn). In addition, α-Fe(Zn) would subsequently contain pre-existing cracks that do not penetrate the steel substrate. At 240 s, external loading would result in solid metal induced embrittlement (SME), and subsequently a V-shaped crack would appear, whereas at 600 s, the reduced Zn content within α-Fe(Zn) would reduce the amount of Zn available to cause SME. Instead, longer annealing times result in the opening of pre-existing cracks due to differing thermal expansions, and as such the microcracks are U-shaped and shallow.

2.8 Properties of continuous galvanized press hardened steels

For widespread use in the automotive industry, the properties of continuous galvanized sheets must be assessed. All blanks should be compatible with the current paint system in use, and the parts should be formable and weldable. Most importantly, due to the fact that these parts will come in contact with an aqueous environment, their corrosion resistance must be thoroughly studied and discussed.

2.8.1 Paintability

One of the main issues with painting DHPF GI coatings is the formation of the oxide layers on the surface. These oxides do not form in a uniform manner, and as a result lead to poor paintability. To combat this issue, surface oxides are typically removed by sandblasting to ensure good paint adhesion [2]. After removal of the oxide layer, it has been reported that the paintability of DHPF GI coatings is comparable to GA coatings [62]. Moreover, the phosphatability and paint adhesion to GI coatings after hot stamping has also been found to be good [63].

2.8.2 Weldability

In the same manner as with paintability, surface oxides affect the weldability of Zn-coated DHPF sheets by increasing contact resistance [62, 64]. To decrease this, the surface of the coating must be cleaned prior to welding [2]. However, this cleaning process often leaves behind compact oxides, which serve to increase contact resistance. Thus, it has been stated that, in order to minimize the amount of surface oxides formed, the annealing cycle must be optimized. Shorter annealing times have been reported to result in thinner oxide layers, thereby reducing contact resistance [35, 64]. Tensile shear strengths of the welds were found to be equivalent regardless of if the material was coated or not, indicating that the mechanical properties of the weld are unaffected by the presence of a coating layer [63].

2.9 Corrosion properties of Fe-Zn intermetallics and α-Fe(Zn)

One concern during forming processes is the high temperature needed; however, this is not detrimental to the blanks as the coating is capable of providing good cathodic protection even when the substrate steel has been exposed. This is directly owing to the sacrificial nature of Zn when coupled with Fe [20]. During forming, the coating layer is transformed from nearly pure Zn to a mixture of α-Fe(Zn) and Γ-Fe_3Zn_{10}. The increased Fe content within these phases gives rise to more noble electrochemical potentials; however, these potentials remain more negative than that of the steel substrate, and as a result it can be inferred that the coating will still provide cathodic protection [43].

After stamping, the blanks have been found to provide better resistance to perforation corrosion, often theorized to be a result of the formation of more stable corrosion products and increased coating layer thicknesses [4, 43, 62]. Furthermore, hot stamped GI coatings display better cosmetic corrosion resistance than Al-Si coatings as they provide sacrificial protection to the cut-edge [4]. The higher Fe contents within the Fe-Zn intermetallics yields red-coloured corrosion products, however, this is not the red rust that is typically associated with the corrosion of steel [43]. For these coatings to provide robust cathodic protection, it has been hypothesized in literature that the α-Fe(Zn) within the coating contain a minimum average Zn content of 20-30 wt% [2, 62]. In accordance to the phase diagram in Figure 2.5 [32], it can be seen that the maximum solubility of Zn within α-Fe(Zn) at 900°C is 35 wt% [2, 65]; however, previous literature has often found that the maximum global Zn content is 20-26 wt% [4].

Figure 2.14 displays the results of a test on GA60 (ie. 60 g/m^2/side) coatings conducted by Lee et al. [66], which consisted of a galvanostatic transient using a deaerated electrolyte consisting of 100 g/L ZnSO and 200 g/L NaCl at 2.5 mA/cm^2. From this image, four different electrochemical potentials can be determined based upon the voltage plateaus, or electrochemical potential arrests. These correspond to the various Fe-Zn intermetallics formed in GA coatings, with increasing intermetallic iron contents increasing the electrochemical potential. It was found that, for ζ-$FeZn_{13}$, the electrochemical potential was –870 mV_{SCE}, for δ-$FeZn_{10}$ it was found to be –820 mV_{SCE}, and for Γ-Fe_3Zn_{10} it was found to be –770 mV_{SCE}. These values were all found to be more negative in comparison to the electrochemical potential of iron, specifically –480 mV_{SCE}, indicating that cathodic protection should be achieved.

In addition, it should be noted that the thickness of each phase layer is proportional to the amount of time the test remains at a given electrochemical potential. As such, it can be determined that the given coating consisted mainly of ζ-$FeZn_{13}$, with δ-$FeZn_{10}$ and Γ-Fe_3Zn_{10} being present in approximately the same ratio. Furthermore, initial times indicate a lower electrochemical potential of around –1030 mV_{SCE}; this would be characteristic of pure Zn, or more specifically η-Zn, on the outer edge of the coating.

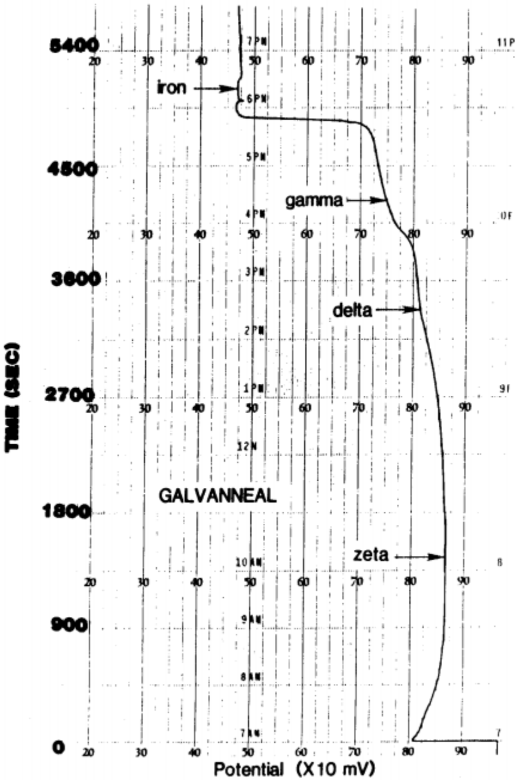

Figure 2.14: Galvanostatic test on an GA60 coating conducted at i = +2.5 mA/cm^2 [66].

Salt fog environmental exposure displayed red rust on the sample surface after 24 hours, whereas the sample containing only η-Zn first displayed signs of red rust after 200 hours [66]. While some literature [67] indicates that this is a sign of poor corrosion performance, it should be noted that red rust will form preferentially on Fe-Zn intermetallic containing samples as they contain higher Fe contents than η-Zn. Lee et al. [66] confirmed this statement, finding that no red rust formed at the steel substrate. Instead, it was found that the red rust formed on the coating, indicating that it formed as a result of the corrosion of Fe-Zn intermetallics.

Lee et al. [66] also found that increasing the thickness of the Zn coating decreased the amount of scribe creepage during corrosion tests. Red rust was present for all samples except the sample containing only η-Zn. These results can be found in Table 2.1 below, which indicates that defects have a less detrimental effect on coatings containing Fe-Zn intermetallics. Figure 2.15 also shows their results from the VDA test, where significant scribe creepage can be seen on both the galvanized and electrogalvanized samples.

Table 2.1 - Salt fog test results on scribed samples [66].

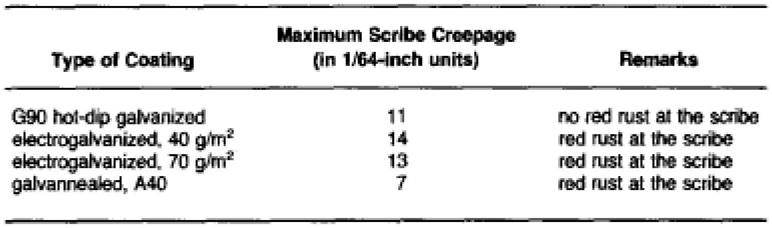

Type of Coating	Maximum Scribe Creepage (in 1/64-inch units)	Remarks
G90 hot-dip galvanized	11	no red rust at the scribe
electrogalvanized, 40 g/m^2	14	red rust at the scribe
electrogalvanized, 70 g/m^2	13	red rust at the scribe
galvannealed, A40	7	red rust at the scribe

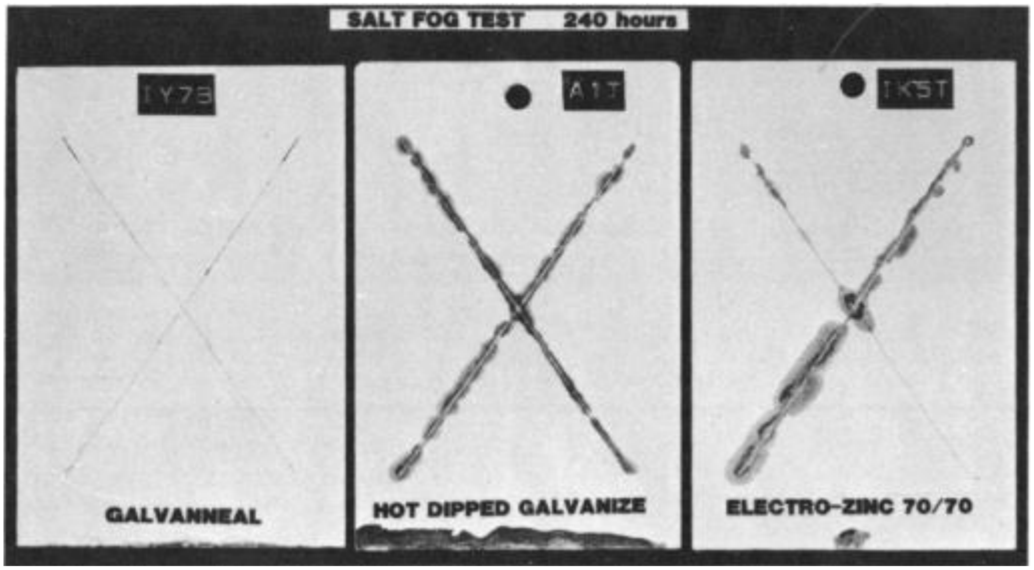

Figure 2.15: Scribe creepage after duration of salt fog tests [66].

Furthermore, Lee et al. [66] did not detect any intergranular corrosion during high humidity and temperature corrosion tests, and no delamination of the coating was detected. However, it was stated that intergranular corrosion should only occur when the Zn bath contains lead [66]; this is not an issue for any current studies due to health and safety hazards.

Based upon their findings, Lee et al. [66] have stated that coatings containing Fe-Zn intermetallics display lower corrosion rates in comparison to coatings containing only η-Zn. This is likely due to the formation of insoluble corrosion products, which act as barriers against oxygen diffusion [43]. Larger amounts of ζ-FeZn$_{13}$ within the coating improve cosmetic corrosion resistance, specifically decreasing the amount of red rust seen due to the increased Zn content of the phase [66].

Work by Autengruber et al. [43] found galvanostatic potential arrests for the Γ-Fe$_3$Zn$_{10}$ and α-Fe(Zn) at $i = +11.76 mA/cm^2$, determined to be $-540\ mV_{SHE}$ and $-400\ mV_{SHE}$, respectively. In contrast, the uncoated steel substrate was found to have an electrochemical potential of $-220\ mV_{SHE}$. As a result, Γ-Fe$_3$Zn$_{10}$ will be capable of providing robust cathodic protection, while α-Fe(Zn) will provide reduced cathodic protection.

Galvanostatic testing by Autengruber et al. on a GI70 coated PHS confirmed the presence of two phases within the coating layer by the three separate voltage plateaus, as seen in Figure 2.16 [43]. Their results indicated a small amount of Γ-Fe$_3$Zn$_{10}$ in comparison to the α-Fe(Zn). They also believed that the increase in electrochemical potential for the iron in the hardened sample in comparison to the unhardened sample was due to an increase in the carbon content, but could not confirm this theory. They further stated that the hardened steel had lower corrosion rates in comparison to the unhardened steel based upon the length of time it took for each to reach the potential of the bare steel. This was likely attributed to the increased thickness of the coating layer, as prior to press hardening, the coating layer is typically around 10 μm thick; after austenitization, the coating layer increased in thickness to around 20 μm [43].

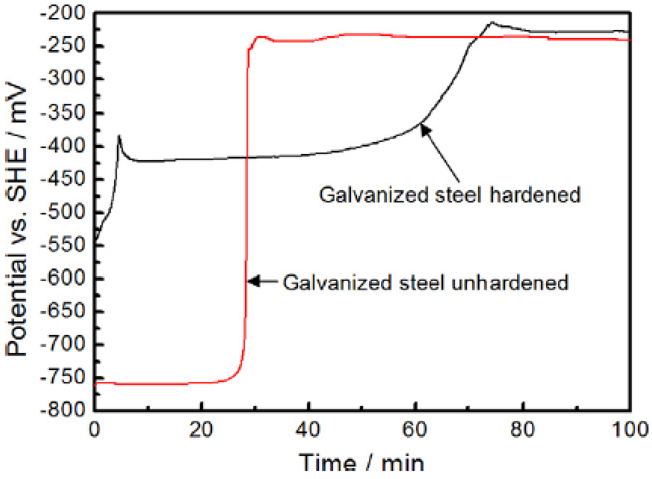

Figure 2.16: Galvanostatic polarization transients at i = +11.76 mA/cm^2 on GI70 coated 22MnB5 annealed at 910°C for 360 s after press hardening [43].

Autengruber et al. [43] also found the presence of red-coloured corrosion products at the beginning of corrosion tests, as seen in Figure 2.17. It was found that longer exposure times resulted in the darkening of the surface. This would be due to the fact that for the initial times, the Γ-Fe_3Zn_{10} would corrode due to the increased Zn content whereas for longer times, the α-Fe(Zn) would corrode. As such, the increase in Fe content between the two phases would lead to different corrosion products forming. More specifically, darker corrosion products form due to the corrosion of the α-Fe(Zn) [43]. It has been found that the minimum Zn content within α-Fe(Zn) is 20 wt% [36].

Accelerated corrosion tests conducted by Dosdat et al. [4] on a GI70 coated 22MnB5 annealed at 870°C for 360 s were used to determine the perforation and cut-edge corrosion resistance. It was found that the DHPF GI coating had better cosmetic corrosion resistance in comparison to the reference GI coating (Z100) and the uncoated substrate material. Most importantly, however, it was found to have better resistance to cut-edge corrosion, indicating that the coating is capable of providing cathodic protection. It was found that the press hardened coating exhibited signs of red rust from the onset of corrosion testing; this was a result of the increased Fe contents within the coating layer. Thus, it was stated that the red rust criterion cannot be used to assess corrosion performance of DHPF GI coatings [4].

In contrast, the red corrosion products for the unhardened samples possessed a different colour and morphology, as discussed by Autengruber et al. [43]. It was theorized that this corrosion product was a result of base material attack, whereas the red-coloured corrosion products seen on the hardened samples was no indication for base material attack. They further assessed the cross-sections of the samples that had corroded to understand more about the base material attack. As seen in Figure 2.18 [43], only superficial attack was observed on the hardened samples, which could not penetrate deep enough to reach the substrate. As such, even after 10 weeks of exposure, no base material attack was seen. This provides further evidence that the red-coloured corrosion products were a result of corroding α-Fe(Zn).

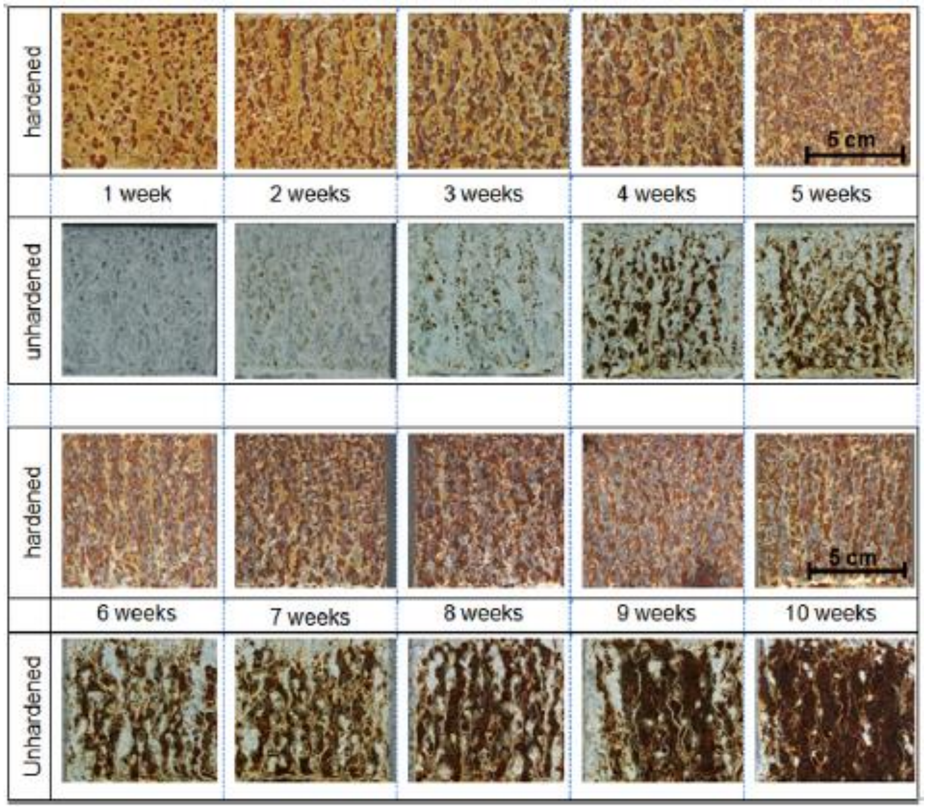

Figure 2.17: Results of VGA 621-415 on hardened and unhardened galvanized sheets [43].

Galvanostatic testing has been used to confirm the presence of these phases, indicated by dissolution plateaus corresponding to the preferential dissolution of a specific phase. First, Γ-Fe_3Zn_{10} dissolves as a result of its lower electrochemical potential due to the increased percentage of Zn within the phase. α-Fe(Zn) is subsequently the next phase to dissolve, and finally the bare steel substrate.

To further support the galvanostatic data, Autengruber et al. [43] confirmed that the Γ-Fe_3Zn_{10} was the first to corrode from Figure 2.18. They believed that the corrosion of the Γ-Fe_3Zn_{10} would result in corrosion products that were more brightly coloured due to the lower Fe content. Their results further confirm that the Γ-Fe_3Zn_{10} provides cathodic protection for both the steel substrate and the α-Fe(Zn) [43].

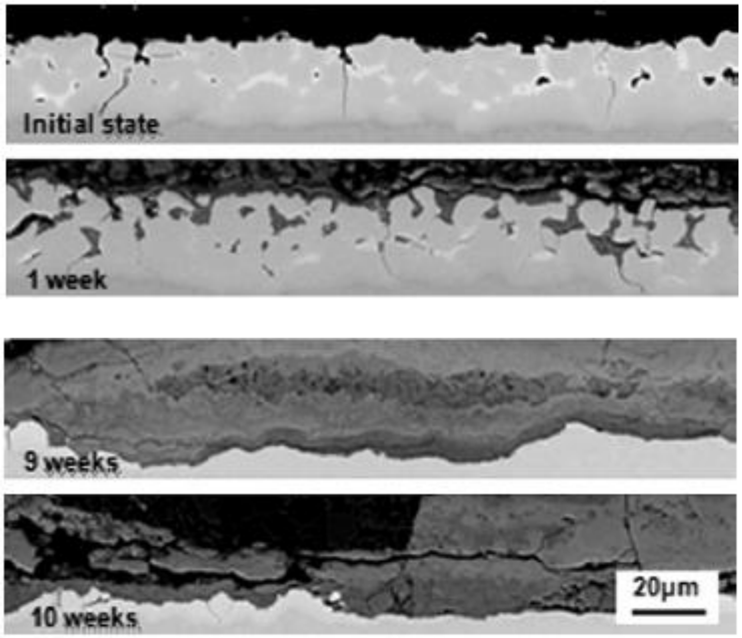

Figure 2.18: Cross-sectional view after exposure to VDA 621-415 on Zn-coated PHS [43].

2.10 Formation of corrosion products on Zn-coated DHPF Steels

Previous literature has reported on decreased corrosion rates observed for DHPF galvanized coatings, which has been attributed to the formation of specific corrosion products [43, 67]. These formed corrosion products arise as a result of the exposure environment. These include hydroxides and oxides, carbonates, chlorides, sulfates, and chlorosulfates. To understand the formation of corrosion products on the surface, the anodic and cathodic reactions occurring on the Zn coating must be considered, and are, respectively: $Zn \rightarrow Zn^{2+} + 2e^{-}$ and $O_2 + 2H_2O + 4e^{-} \rightarrow 4OH^{-}$. Resultant of these reactions, zinc dihydroxide ($Zn(OH)_2$) forms as per $Zn^{2+} + 2OH^{-} \rightarrow Zn(OH)_2$; this phase has been previously reported to have poor solubility in neutral aqueous solutions [68].

Corrosion rates of press formed GI70 coatings have been found to vary in different environments. Zhu et al. [69] have reported that CO_2 and Cl containing environments (specifically NaCl) decreased corrosion rates by up to 6 times. Their work determined that, at low pH values and high Cl concentrations, simonkolleite ($Zn_5(OH)_8Cl_2 \cdot H_2O$) formed per $5Zn(OH)_2 + Cl_2 \rightarrow Zn_5(OH)_8Cl_2 \cdot H_2O + \frac{1}{2}O_2$. The presence of CO_2 within the environment (atmospheric conditions) formed hydrozincite ($Zn_5(OH)_6(CO_3)_2$) as a result of $5Zn(OH)_2 + 2CO_2 \rightarrow Zn_5(OH)_6(CO_3)_2 + 2H_2O$. Furthermore, ZnO has often been found to form at higher pH levels. From the results presented in Figure 2.19 [69] and previous literature [70], it can be stated that the formation of compact Zn-based corrosion products is favoured when exposed to a neutral or slightly alkaline environments.

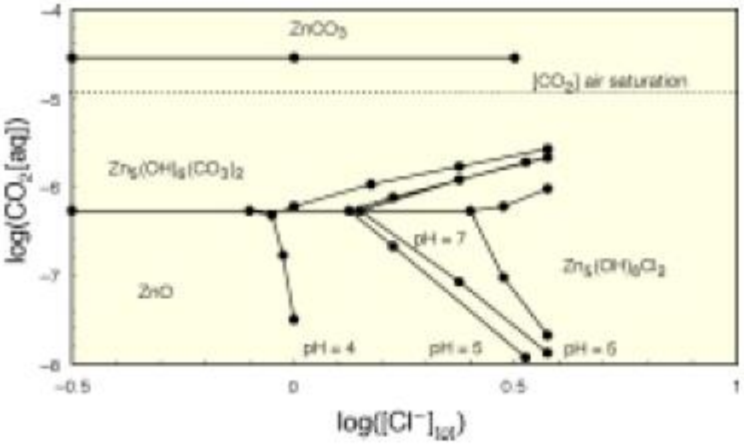

Figure 2.19: Phase stability diagram of formed corrosion products from GI70 coatings as a function of pH [69].

Some literature has reported that the presence of ZnO may act to passivate the coating, thereby decreasing corrosion rates of Zn-coated PHS [71]. However, this is unlikely to be true as it has been found that it weakly adheres to the outer coating layer, forming a very wavy interface [2, 35]. Lack of ZnO adhesion is especially true once the layer reaches a thickness greater than 2 μm [2]. Zn-based corrosion products, such as simonkolleite and hydrozincite, in contrast, may act as passivation agents as they have been found to be insoluble and form compact layers on the surface of the coating [35, 67]. Previous work by Dafydd et al. [72] found that Zn-coatings exhibited a limiting current in aerated conditions. Diffusion controlled O_2 reduction was attributed to the presence of $Zn(OH)_2$. The presence of corrosion products has also been found to severely reduce the oxygen reduction at cut-edges, promoting what has often been referred to as “cathodic self-healing” [73].

Autengruber et al. [43] found that after 5 weeks in the VDA test, corrosion of both Γ-Fe_3Zn_{10} and α-Fe(Zn) had occurred. As a result, it was expected that corrosion products characteristic of both phases would be observed. Using FT-IR, Raman spectroscopy, and XRD, Autengruber et al. [43] were able to determine that simonkolleite, hydrozincite, and akaganeite (β-FeOOH) had formed as a result of the corrosive environment. The run-off white lines were attributed to hydrozincite, the orange coloured areas to simonkolleite, and the dark red areas to akaganeite. It was determined that simonkolleite formed as a result of the corrosion of the Γ-Fe_3Zn_{10} due to the higher Zn content, and that akaganeite formed as a result of the α-Fe(Zn) corroding. Hydrozincite has been found to form as the concentration of carbonate ions on the surface increases, and when the pH of the solution is neutral or basic [43, 74, 75].

There have been conflicting opinions in literature on which Zn-based corrosion product acts as the predominant corrosion inhibitor. Autengruber et al. theorized that simonkolleite acts as a cathodic inhibitor due to its layered structure, compact morphology, and low electron density [43]. Qu et al. found that simonkolleite precipitated near anodic sites and blocked further corrosion attack due to its insoluble nature [76]. In contrast, work by Ligier et al. found that the corrosion rate was reduced by the presence of hydrozincite, but was unaffected by simonkolleite [74]. Le Bozec et al. also reported on increased corrosion rates in the absence of a CO_2 containing environment [75]. This is also likely to be attributed to the fact that CO_2 may act to buffer the pH; in its absence, the environment is more alkaline [77]. As such, further work is necessary to resolve which corrosion product acts as the cathodic inhibitor to oxygen diffusion. Unlike the stable and insoluble Zn-based corrosion products, akaganeite has been reported to reduce oxygen to OH^- [78]; as a result, it can be stated with certainty that akaganeite does not decrease the corrosion rate of DHPF Zn-coated steels.

2.11 Summary on the electrochemical properties of DHPF coatings

At the present, it has been found that DHPF GI coatings provide increased corrosion resistance in comparison to the non heat-treated GI coatings due to the formation of a compact, insoluble corrosion product layer [43, 42]. Much of the work performed on GI coatings after press hardening has confirmed that Γ-Fe_3Zn_{10} will provide robust cathodic protection. However, questions arise around the protectiveness of α-Fe(Zn). The increased Fe content as a result of longer austenitization times leads to increased nobility such that the electrochemical properties of α-Fe(Zn) are similar to that of the substrate material [79]. The work by Mutgi [79], however, indicated that coatings that contained only α-Fe(Zn) provided better passivation than coatings that contained a mixture of Γ-Fe_3Zn_{10} and α-Fe(Zn) due to the combination of simonkolleite and akaganeite. These results are inconsistent with previous literature, which has indicated reduced corrosion rates for samples containing Γ-Fe_3Zn_{10} and α-Fe(Zn) due to the formation of simonkolleite and hydrozincite [43, 74-76], and increased corrosion rates when the formed corrosion product is akaganeite due to its affinity for oxygen reduction [78]. Previous literature has theorized that a α-Fe(Zn)-only containing coating should have a Zn content of at least 30 wt% to achieve robust cathodic protection [2, 8]. However, it has been found that the α-Fe(Zn) obtained at 900°C typically has a Zn content between 20-26 wt% [4].

3 RESEARCH OBJECTIVES

Previous literature has stated that robust cathodic protection may be obtained when the α Fe(Zn) within the coating layer contains at least 30 wt% Zn. The main objective of this study was thus to assess how the coating microstructure evolved as a function of annealing time at 900°C, and, thereby, the fraction of Γ-Fe_3Zn_{10} within the coating, affected the electrochemical properties with a focus on the potential for providing robust cathodic protection. Based upon previous literature, it is hypothesized that there exists some critical fraction of Γ-Fe_3Zn_{10} necessary to achieve robust cathodic protection. The overall industrial objective of this study was to find a direct hot press stamping process window compatible with the currently used 22MnB5 grade that would provide robust cathodic corrosion protection while avoiding LME and microcracking of the substrate.

In order to test these objectives, GI70 coatings on a 22MnB5 substrate were held at 900°C for holding times ranging from 30 s to 420 s to alter the coating chemistry and microstructure. Microstructural changes as a function of annealing time were characterized at a variety of length scales including glow discharge optical emission spectrometry (GDOES), X-ray diffraction (XRD), field emission scanning electron microscopy – energy dispersive X-ray spectroscopy (FE-SEM)/(EDS), scanning Auger microscopy – Auger electron spectroscopy (SAM-AES), and transmission electron microscopy (TEM). Coating electrochemical properties as a result of the changes in coating morphology were then assessed using a variety of techniques, including potentiodynamic polarization scans, galvanostatic polarization scans, potentiostatic scans, and galvanic corrosion measurements.

4 EXPERIMENTAL METHOD

Experiments were conducted to determine the effect of austenitizing time on the microstructure, and subsequently how these microstructural changes affected overall corrosion and mechanical properties.

4.1 Steel chemistry and sample preparation

The experimental composition of the 22MnB5 substrate, as determined using inductively coupled plasma – optical emission spectroscopy (ICP-OES), is detailed in Table 4.1. ICP-OES analysis was performed on a VISTA-PRO CC Simultaneous ICP-OES instrument. The steel composition obtained was in agreement with that specified for 22MnB5 [80]. All experimental steels were provided by ArcelorMittal Dofasco (Hamilton, ON) in the as-coated state and comprised 1.5 mm thick flat sheets with a nominal coating weight of GI70 (i.e. 70 g/m^2/side). For the purpose of this study, only galvanized (GI) coatings were investigated. The coating weight of the sheet was evaluated using ASTM A90/A90M [81] and was determined to be 72 g/m^2/side. The as-received (AR) coating properties are provided in Table 4.2. It should be noted that width position refers to the placement of the sheet with respect to the drive side of the coil, such that E1 is closest to the drive side and E2 is the outer edge.

Uncoated 22MnB5 substrate material was also provided by ArcelorMittal Dofasco in its unhardened state. Figure 4.1 (a) shows the AR microstructure, consisting of ferrite and pearlite. Figure 4.1 (b), in comparison, shows the microstructure of the AR coated material, which was found to also consist of ferrite and pearlite. However, it can be seen that grains have become elongated in the rolling direction, and the overall fraction of αFe within the microstructure has increased while the fraction of pearlite has subsequently decreased. The samples were prepared as described in §4.6.

Table 4.1: 22MnB5 steel chemical composition, as determined by ICP-OES (wt%).

C	Mn	Si	Cr	P	S	B	Al	Ti	Fe
0.221	1.169	0.252	0.179	0.0123	0.0025	0.0025	0.0383	0.0283	Balance

Table 4.2 AR GI70 coating properties.

							Coating weight		Fe (mass%)	
ID	Length position	Width position	Surface	Coating Weight (g/m^2/side)	Al (mass%)	Fe (mass%)	Top (g/m^2/side)	Bottom (g/m^2/side)	Top (g/m^2/side)	Bottom (g/m^2/side)
GI70	Tail	E1	Top	76	0.49	0.34	73	73	0.35	0.37
			Bottom	71	0.55	0.40				
		CTR	Top	75	0.45	0.28				
			Bottom	75	0.48	0.33				
		E2	Top	68	0.56	0.42				
			Bottom	74	0.53	0.39				

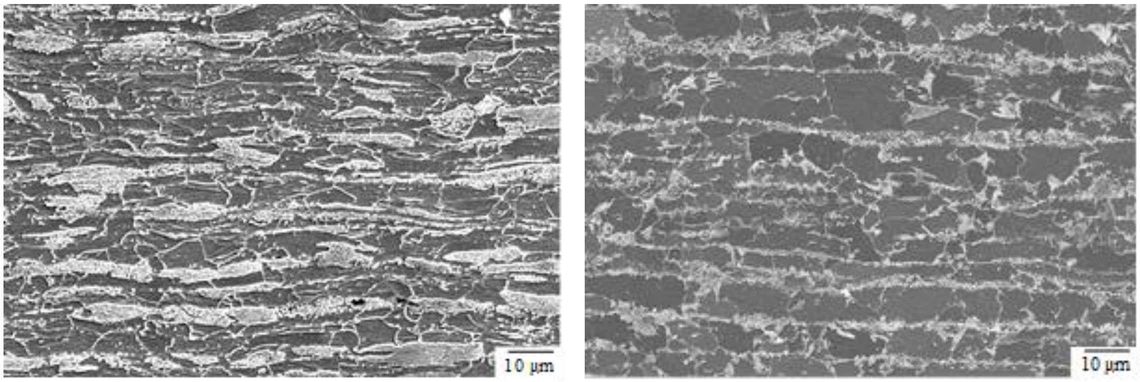

a) b)

Figure 4.1: Secondary electron images of a) AR uncoated 22MnB5 substrate material and b) AR GI70 coated 22MnB5 substrate material.

Experimental coupons were prepared from the larger sheet measuring 30 mm in the transverse direction (TD) and 50 mm in the rolling direction (RD). Prior to annealing, coupons were cleaned ultrasonically with acetone for 5 minutes followed by ultrasonic cleaning in ethanol for 5 minutes to remove all surface contaminants, followed by drying using a warm air stream.

4.2 Heat treatments

Coating microstructural evolution was assessed at the austenitizing temperature of 900°C for annealing times ranging from 30 s to 420 s. All heat treatments were performed using a conventional tube furnace, as depicted in Figure 4.3, under an ambient atmosphere. Parallel gas quenching platens using room temperature compressed air at were used for quenching. All coupons were oriented such that the sheet surface was parallel to both the bench surface and the cooling platens. Time-temperature profiles for all samples were measured using a 0.5 mm K-type thermocouple welded to the centre of each coupon. Coupons were placed into the tube furnace and pre-heated to a set temperature of 900°C using the slider. Experimental annealing times began once the coupon had reached a temperature of 890°C. Once the sample reached an internal temperature of 890°C, samples were held for the set annealing times presented in Table 4.3. After being annealed for the target annealing times, the samples were removed from the furnace and quenched using compressed air with a flow rate of 0.005 m^3/s and a pressure of 600 kPa via the cooling platens such that the cooling rates were approximately 75°C/s. Cooling continued until the sample reached 60°C. All resultant substrate microstructures were confirmed to be fully martensitic through a combination of uniaxial testing and scanning SEM analysis. Figure 4.2 shows the typical microstructure of the substrate material after experimental hardening, whereby a fully martensitic microstructure was obtained.

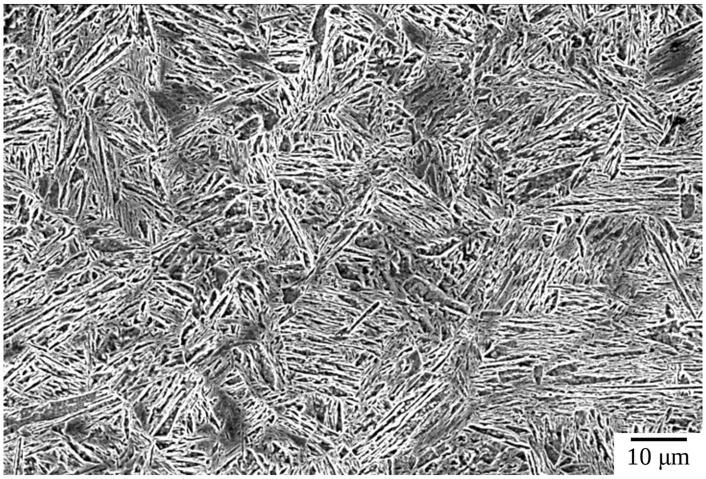

Figure 4.2: Secondary electron image of 22MnB5 substrate after experimental hardening.

For microstructural and electrochemical comparison, samples with a coating comprising only Γ-Fe_3Zn_{10} were produced using the experimental set up detailed in Figure 4.3. Samples were inserted into a furnace preheated to 700°C using the slider. Once the coupon reached a temperature of 690°C, samples were held in the furnace for 60 s before being removed and quenched.

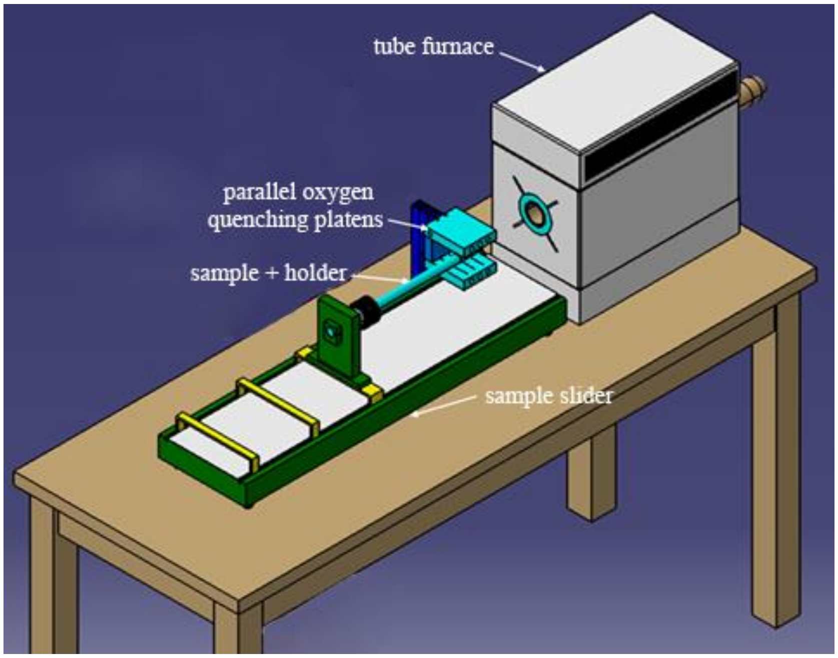

Figure 4.3: Schematic of tube furnace set up for microstructural and corrosion coupon preparation.

Table 4.3: Experimental annealing conditions.

Sample	Annealing Temperature (°C)	Annealing Time (s)
GI70	900	30, 60, 120, 180, 240, 300, 360, 420
GI70	700	60

Typical time-temperature profiles for GI70 samples annealed at 900°C can be found in Figure 4.4. Samples reached the target start temperature of 890°C within 210 s, and all samples met the target cooling rate of 75°C/s. Heating and cooling rates were determined to be consistent on both the upper and lower surfaces of the coupon.

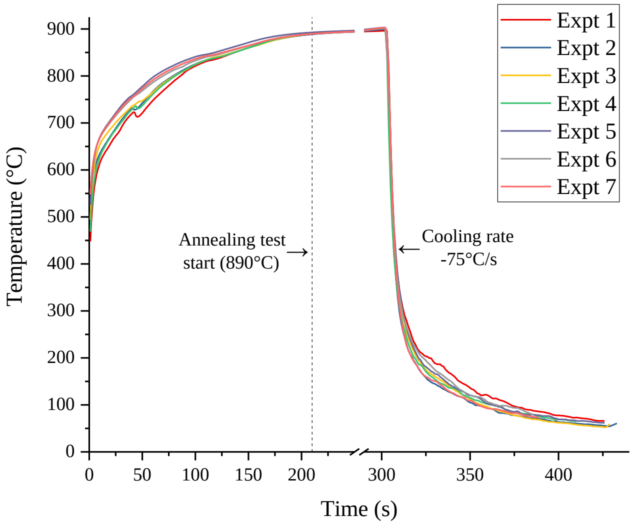

Figure 4.4: Typical time-temperature profiles at the 900°C PAT.

4.3 Tensile testing

All uniaxial tensile tests were performed at room temperature using an Instron 100 kN testing frame with a cross-head speed of 1 mm/minute. Samples were first annealed as specified in §4.2 before machining into sub-sized tensile samples per ASTM E8/E8M [82]. All tensile samples were machined from the middle of the experimental coupon with the length parallel to the RD. Sample extension during tensile testing was monitored using a 5 mm contact extensometer in all cases.

Tests were repeated in triplicate for all samples. The equation used to calculate engineering stress can be seen in equation (4.1), where σ represents engineering stress denoted in MPa, F the tensile force in N, A_0 the original cross-sectional area prior to tensile testing of the tensile gauge in mm^2. The equation used to calculate engineering strain can be seen in equation (4.2), where ε represents the engineering strain, ΔL the change in gauge length in mm, and L_0 the original gauge length prior to testing in mm [83].

$$\sigma = \frac{F}{A_0} \tag{4.1}$$

$$\varepsilon = \frac{\Delta L}{L_0} \tag{4.2}$$

4.4 Glow discharge optical emission spectrometry analysis

GDOES was performed using an Yvon Horiba GD-Profiler HR to determine elemental depth profiles as a function of annealing time at 900°C, with a primary focus on the overall Zn content within the coating. All analyses were performed using Ar sputtering with a sputtering rate of 130 nm/s and a spot size of 4 mm. The flush time was 60 s, and the Ar pressure was set as 600 Pa. Prior to sample testing, Al, Zn, and Fe standards were used to calibrate the machine.

4.5 Two-dimensional X-ray diffraction

XRD^2 analysis was used for quantitative analysis of the annealed coatings, and were performed as a coupled θ/2θ scan. A Bruker Mo Smart APEX2 diffractometer with Co $K\alpha_1$ (λ=1.79026 Å) radiation was used to minimise the effects of Fe fluorescence. The detector distance was 20 cm to the sample surface. The X-ray generator voltage was set as 35 kV and the generator current was set as 45 kV. A 0.5 mm collimator and 1 mm slit size were used. Diffraction angles between $10° \leq 2\theta \leq 90°$ with 0.02° step intervals and step times of 600 s were used to collect the diffraction data. To mitigate texture effects, samples were rotated during data collection. Diffraction data was subsequently analysed using Diffrac Eva, and Rietveld refinements were performed using TOPAS5 software for quantitative phase analysis. Error bars were determined using the 95% confidence interval over three repeated experimental measurements per annealing time.

4.6 Scanning electron microscopy analysis of the coating microstructures

SEM was performed using a JEOL 6610 LV microscope. SEM was used to assess the morphology of the coatings as a function of annealing time, as well as to confirm the coating thicknesses determined from GDOES analysis. Working distances of 10 mm and acceleration voltages of 10 keV were used for all images. SEM analysis was performed on cross-sections after annealing, and images were taken such that the rolling direction of the sample was parallel to the longitudinal axis of the micrograph. Coupons were cold-mounted in epoxy resin and prepared using conventional metallographic preparation with a final polishing step of 1:1 OPS and ethylene glycol. To reveal the microstructure of the substrate, samples were etched with 2% nital for 5 s. This step was not performed for coating layer assessment as etching has been known to preferentially attack Fe-Zn intermetallics. More detailed metallographic preparation is listed in Appendix A. After polishing, samples were ultrasonically cleaned in ethanol, blown dry with a hot air stream, rinsed with isopropanol, and blown dry again. All samples were coated in carbon to avoid sample charging while allowing for accurate energy dispersive X-ray spectroscopy (EDS) measurements. To enhance elemental contrast between coating phases, backscattered electron (BSE) imaging mode was used. EDS elemental maps, point scans, and line scans were used to correlate the Fe-Zn phase chemistry with the coating microstructure using AZtec Version 3.3 Oxford Instruments software.

4.7 Scanning Auger microscopy

Auger electron spectroscopy (AES) was performed using a JEOL JAMP 9500F field emission scanning Auger microscope (FE-SAM). SAM-AES was used to provide elemental analyses within the first few atomic layers of the sample surface, specifically to detect the intermetallic phases present at the surface of the coating as a function of annealing time at 900°C. SAM-AES was also used to better spatially resolve the formed corrosion products that formed as outlined in §4.12. In addition, SAM-AES provides excellent lateral spatial resolution using a minimum probe diameter of 8 nm, allowing it to resolve minute differences between α-Fe(Zn) and Γ-Fe_3Zn_{10}.

A combination of plan view and cross-sections of the as-annealed and interrupted galvanostatic coupons were assessed using SAM-AES. As-annealed coupons in the plan view were lightly ground mechanically using 1200 grit SiC paper to remove loose oxides on the sample surface. Once inserted into the Auger, samples were tilted to 30° and the working distance was set between 20-23 mm. A sputtering 3 keV argon (Ar) ion beam was used to completely remove the surface oxides present to reveal the coating's surface. To remove all oxides present, sputtering was performed for a duration of 360 s (6 min.). Samples that had undergone interrupted galvanostatic testing were not mechanically ground to prevent the removal of lightly adherent corrosion products. Ar etching was performed for 30 seconds to remove surface contaminants, such as C and O, that were deposited subsequent to testing. Cross-sections of the interrupted galvanostatic tested samples were ground and polished using standard metallography techniques up to 1 μm. As previously, Ar etching was performed for 30 s to remove surface contaminants deposited after polishing and before insertion into the FE-SAM.

Auger elemental mapping was performed over designated sample areas to assess elemental distribution using a probe current of 70 nA. For the as-annealed samples, Fe, Zn, O, and Al were included within the scan, however, no significant fractions of Al were detected and as a result the Al elemental maps were discarded. For the corroded samples, Fe, Zn, O, Al, C, Cl, S, and N were included in the scans.

4.8 Transmission electron microscopy sample preparation using focused ion beam milling

Site-specific TEM sample preparation across the coating cross-section of a corroded sample was performed using focused ion beam (FIB) milling using Ga^+ ions and with a NVision 40 by Zeiss FIB. Due to how easily Zn is sputtered in comparison to Fe, carbon was deposited over the sample location to mitigate preferential thinning of the coating layer. To see how the site was extracted, please refer to Appendix A.

4.9 TEM analysis

All TEM analysis was performed using a FEI Titan 80-300 HB, which makes use of a XFEG source. TEM was used to resolve the corrosion products that formed as a result of interrupted galvanostatic polarization testing, as detailed in §4.12. The acceleration voltage was set as 200 keV. Electron energy loss spectroscopy (EELS) analysis with a dispersion of 0.2 eV/pixel was performed for elemental mapping of the sample surface, and subsequently point analyses to identify specific corrosion products. The acquired EELS spectra were calibrated using the major Fe-$L_{2,3}$ edge at 708 eV, and were subsequently analysed using INCA software [84]. Once the data had been analysed, all spectra were compared to reference spectra of anticipated corrosion products, as will be detailed in §5.2.8.

4.10 Corrosion testing and electrochemical measurements

The electrochemical properties of the produced coatings were assessed using a variety of scanning techniques, including potentiodynamic polarization, galvanostatic, and potentiostatic measurements. Galvanostatic corrosion tests were used in an attempt to examine the cathodic protection efficacy offered by the coatings to the substrate material. Prior to the start of testing, all potentiostats underwent ASTM G5-14 [85] testing to ensure that both the experimental technique and instruments were accurate. This standard was repeated every 6 months over the course of the testing. All electrochemical testing was performed using a BioLogic VSP-300 potentiostat or a Gamry Reference 600 potentiostat and a Gamry flat cell specimen holder, which exposed 2.6 cm^2 of the coating layer (i.e. the working electrode) to the electrolyte. A schematic of the cell set-up can be seen in Figure 4.5. All potentials were measured against a saturated calomel reference electrode (SCE) and employed a graphite counter-electrode. It should be noted that the cathode material was only used for the purpose of galvanic corrosion experiments whereby the carbon rod was not used. The effect of crevice corrosion around the working electrode area was mitigated through the use of a silicone O-ring seal. The electrolyte comprised 100 g $ZnSO_4 \cdot 7H_2O$ and 200 g NaCl in 1000 mL of DI water, with a starting pH of 5.8 [86]. All electrolytes were naturally aerated and tests were conducted at room temperature (20°C). Dissolution of Zn from the coating into the electrolyte was mitigated by saturating the electrolyte with respect to Zn^{2+} through the $ZnSO_4 \cdot 7H_2O$ addition. ICP-OES analysis was performed on four solutions to confirm that the electrolyte was saturated with respect to

Zn^{2+}: the base electrolyte, the electrolyte after a 600 s open circuit potential (OCP) exposure, the electrolyte after a 2700 s (45 min) OCP exposure, and the electrolyte after a 600 s OCP and 26 h (93600 s) galvanostatic exposure using a current density of +1 mA/cm^2. The results of the ICP-OES analysis are presented in Table 4.4. All coupons were cleaned and degreased with acetone and dried using a warm air stream before testing.

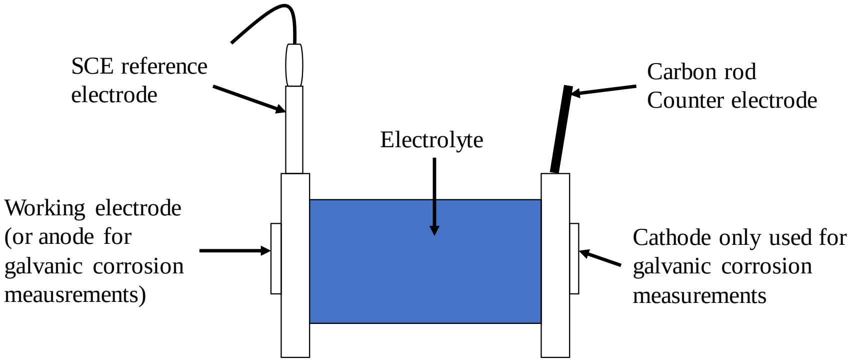

Figure 4.5: Experimental apparatus for all electrochemical testing.

Table 4.4: ICP-OES results of Zn concentration within electrolyte after varying exposure times.

Sample ID	**Element**	**Concentration (ppm)**
Base electrolyte	Zn	182.5
600 s OCP exposure	Zn	186.8
2700 s OCP exposure	Zn	181.8
600 s OCP exposure + 93 600 s galvanostatic exposure	Zn	177.8

OCP measurements were conducted for 600 s prior to the start of all electrochemical measurements to establish equilibrium with the electrolyte without substantial corrosion having occurred. The OCP potential was used to determine the scan range necessary for the potentiodynamic polarization scans as outlined in §4.11.

4.11 Potentiodynamic polarization scans

Potentiodynamic polarization measurements were collected over a scan range from $-0.93\ V_{SCE}$ to $-0.55\ V_{SCE}$ at a scan rate of 0.167 mV/s. Potentiodynamic polarization scans were also performed on the AR GI70 coated steel and the uncoated steel substrate for reference purposes using the same parameters. It should be stated that no microscopic analysis was performed on the samples following the potentiodynamic polarization scans.

4.12 Galvanostatic polarization scans

Galvanostatic polarization measurements were conducted to complete dissolution of the coating layer at an applied current density of +1 mA/cm^2. It should be noted that previous literature has performed galvanostatic scans at an applied current density of or +10 mA/cm^2 [87] or +11.76 mA/cm^2 [79, 88, 89]. However, consideration of the potentiodynamic polarization scans as presented later in this report (detailed in §5.2.2) deemed that this current density was too far into the anodic region to detail cathodic protection, and as a result +1 mA/cm^2 was instead chosen. Galvanostatic polarization scans were employed to encompass the necessity of Γ-Fe_3Zn_{10} within the coating, as well as to identify a predicted critical volume fraction of Γ-Fe_3Zn_{10}. Interrupted galvanostatic polarization measurements were performed at several different dissolution points, and also used a current density of +1 mA/cm^2. The purpose of interrupted galvanostatic polarization scans was to assess the formation of varying corrosion products, and to evaluate performance of the two coating phases in a corrosive environment. In particular, the interrupted galvanostatic measurements were stopped once the second potential arrest had been achieved, indicating the complete dissolution of Γ-Fe_3Zn_{10}. To encompass the dissolution of both Γ-Fe_3Zn_{10} and α-Fe(Zn), further interrupted galvanostatic testing was performed on a GI70 coating annealed for 30 s. These interrupted tests were stopped at three different dissolution times: halfway through the dissolution plateau indicative of Γ-Fe_3Zn_{10} (7000 s), once the dissolution plateau indicative of Γ-Fe_3Zn_{10} had ceased (16 000 s), and halfway through the dissolution plateau indicative of α-Fe(Zn) (32 000 s). Subsequent to testing, samples that underwent interrupted galvanostatic testing were analysed using XRD, FE-SEM/EDS, SAM-AES, and TEM as per §4.5, 4.6, 4.7, and 4.9.

4.13 Potentiostatic scans

Potentiostatic tests were used to determine how the coating microstructure as a function of annealing time at 900°C was affected at specific voltages, either above or below the corrosion potential (E_{corr}) determined from potentiodynamic polarization scans. Three voltages were chosen based upon the experimental results: $-0.97\ V_{SCE}$, $-0.77\ V_{SCE}$, and $-0.61\ V_{SCE}$. More specifically, the sample potentials were set at $\pm 0.10\ V_{SCE}$ from their determined E_{corr}, which was microstructure dependant. Samples were held at the constant voltage for 12 600 s (3.5 h), after which they were removed from solution and subsequently assessed using FE-SEM and EDS as detailed in §4.6.

4.14 Galvanic corrosion measurements

To determine the cathodic protection efficacy of the coatings as a function of annealing time at 900°C, galvanic corrosion measurements were performed. Samples were set up such that the working electrode was the as-annealed sample with the coating exposed, and the counter electrode was the uncoated 22MnB5 substrate material. For these tests, the potentiostat forces the potential difference between the coated and uncoated substrate to be zero and monitors the exchange current density between the coating and substrate. While a reference electrode is not necessary for these tests as it is a "spectator", a reference electrode was placed near the as-annealed coating surface to check that the voltage of the sample remained constant throughout the duration of the test at the OCP value. For the purpose of all experimentation, the annealed coating was always designated as the working electrode and the 22MnB5 substrate material the counter electrode, as can be seen in Figure 4.5. To ensure that the exposed area of both electrodes was identical, Gamry port-hole masks with an exposed area of 1 cm^2 were used.

5 RESULTS

5.1 The microstructural and mechanical properties of GI70 coated 22MnB5 as a function of annealing time

How the microstructure and, subsequently, the mechanical properties of the coated substrate material varied as a function of annealing time at 900°C was investigated. The purpose of this work was to determine how the microstructural evolution and coating morphology as a function of annealing time at 900°C affected the mechanical properties of the uncoated 22MnB5 substrate material and the GI70 coated 22MnB5.

5.1.1 Tensile testing

Uniaxial tensile tests were performed on both the AR and press formed uncoated 22MnB5 substrates to determine if the results complied with the industrial target properties of an ultimate tensile strength (UTS) in excess of 1500 MPa and total elongation (TE) of approximately 5-6%. The engineering stress-strain curves for both materials can be seen in Figure 5.1, where Figure 5.1 (a) depicts that of the AR material and Figure 5.1 (b) shows the annealed and air-quenched sample with a cooling rate of −75°C/s. It should be noted that all tests were performed in triplicate. The AR material displayed typical mechanical properties for a ferrite-pearlite microstructure, with an approximate 30% TE and UTS of 850 MPa, and was found to have an average hardness value of 221 ± 5 HV. These results are in good agreement with the microstructure seen in Figure 4.1 (a) [90]. In contrast, the annealed and quenched sample displayed mechanical properties typical of a fully martensitic microstructure, and had an average hardness value of 521 ± 4 HV. These results are also in good agreement with the microstructure observed in Figure 4.2 [91]. For these samples, the TE was found to be approximately 7-9% and average UTS values were 1630 ± 20 MPa, above the target value as depicted by the dashed line in Figure 5.1 (b). As a result, the annealed samples met the required mechanical property targets [2, 88].

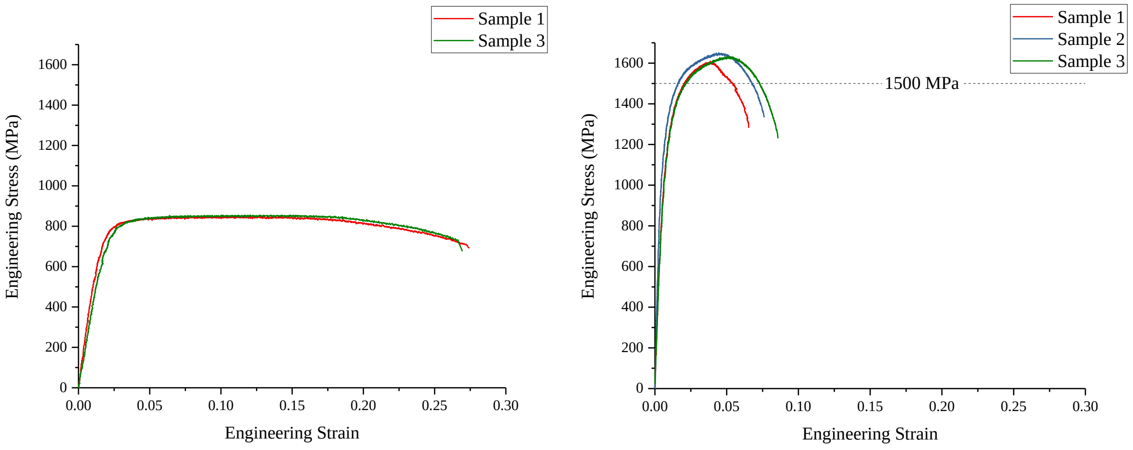

a) b)

Figure 5.1: Engineering stress-strain curves for uncoated 22MnB5 annealed at 900°C a) AR and b) annealed at 900°C for 600 s and air quenched.

It was also important to determine how the annealing temperature and time affected the UTS of the coated samples. The engineering stress-strain curve for the uncoated 22MnB5 substrate as a function of annealing time at 900°C can be seen in Figure 5.2 (a), and was used as a baseline comparison for the GI70 coated samples. It can be seen that, similar to Figure 5.1 (b), all annealing times met the target properties of $\sigma_{(UTS)} \geq 1500$ MPa. Thus, it can be stated that the UTS of the substrate material was not significantly affected by annealing time. Figure 5.2 (b) shows the engineering-stress strain curves obtained for the GI70 coatings as a function of annealing time at 900°C. Unlike the previous results seen in Figure 5.2 (a), it can be seen that, when the sample was annealed for 180 s or longer, $\sigma_{(UTS)}$ was less than 1500 MPa. These results are clearly emphasized in Figure 5.3, where the error bars are the 95% confidence interval (CI) taken from triplicate sampling. Again, the UTS of the uncoated substrate is independent of time, but when the sample is coated, UTS gradually decreased until it dropped below the target value of σ_{UTS} (min) = 1500 MPa after 180 s at 900°C.

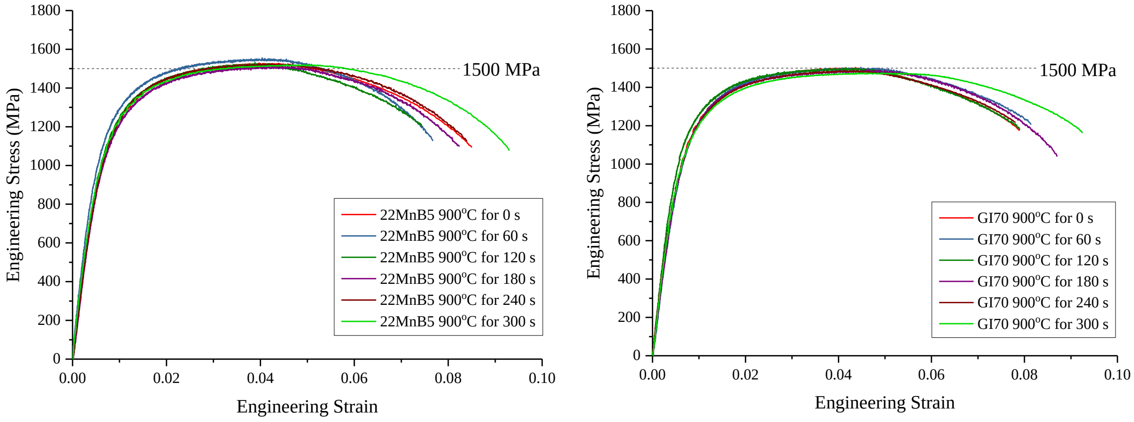

a) b)

Figure 5.2: Engineering stress-strain curves as a function of annealing time at 900°C for a) uncoated 22MnB5 and b) GI70 coated 22MnB5.

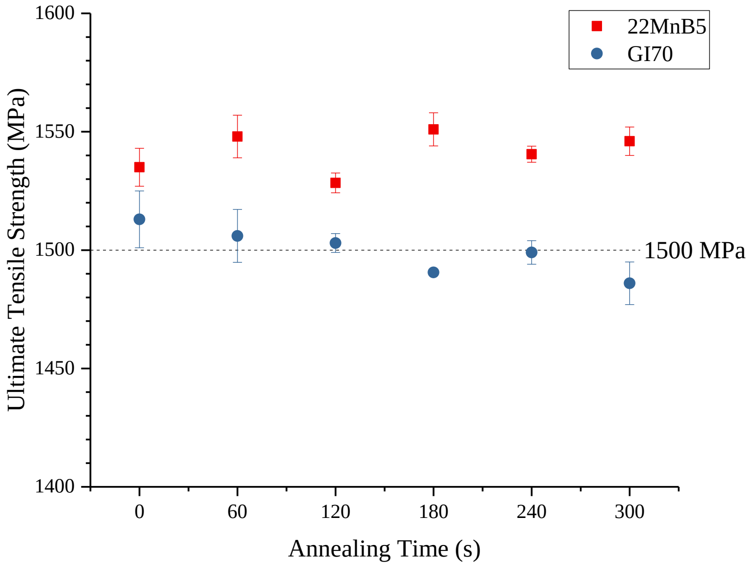

Figure 5.3: Summative plot of $\sigma_{(UTS)}$ as a function of annealing time at 900°C for uncoated 22MnB5 and GI70 coated 22MnB5.

5.1.2 GDOES analysis of the coating layer after annealing

GDOES was used to determine the overall Zn content within the coating layer after annealing at 900°C. The GDOES spectra for all annealing times in at% can be seen in Figure 5.4 (a). It should be noted that only the Zn and Al analyses are depicted within the graph. The overall fraction of Fe within the coating is simply the difference of the sum of the Zn and Al content from 100%. To better represent the average Zn content within the coating layer, the Zn content at a depth of 10 μm (chosen from the starting thickness of the AR coating prior to annealing) as a function of annealing time can be seen in Figure 5.4 (b). It should also be noted that a Zn content of 30 wt% is equivalent to 26.8 at%. From Figure 5.4 (a), it can be seen that Zn penetration depth increased with increasing annealing times, resultant of the diffusion-based growth mechanism of α-Fe(Zn) [13, 37]. As a result, GDOES was able to determine the coating thicknesses of both the AR coupons and the annealed coupons, where the AR coupon had an average coating thickness of 10 μm while the annealed coupons possessed average coating thicknesses between approximately 25 μm and 40 μm. An Al peak can be observed at the surface of the AR coating owing to the presence of Al_2O_3, which forms due to oxidation of the dissolved Al in the coating due to exposure of the liquid metal and the ambient atmosphere. It is noteworthy to also consider the Al peak that occurs at a depth of 10 μm for the AR sample. The rise in Al content is indicative of the $Fe_2Al_5Zn_x$ interfacial layer that forms during dipping [23, 24]. Subsequent austenitization for direct press hardening causes the interfacial layer to become unstable and "breakdown", resulting in the formation Fe-Zn intermetallic phases seen throughout this work [35, 36, 92]. Due to this, all annealed samples do not possess this Al peak at the coating/substrate interface. Similar to the AR sample, a small Al peak was detected at the outer edge of the annealed samples, indicating the presence of an aluminum oxide which forms as a result of oxidation from the residual Al dissolved within the coating. This oxide is likely to be Al_2O_3 [2, 35, 36].

Assessment of Figure 5.4 (b) reveals that annealing times less than or equal to 180 s have an average Zn content within the coating of at least 30 wt% at a depth of 10 μm, whereas annealing times of 240 s or greater possess lower Zn contents.

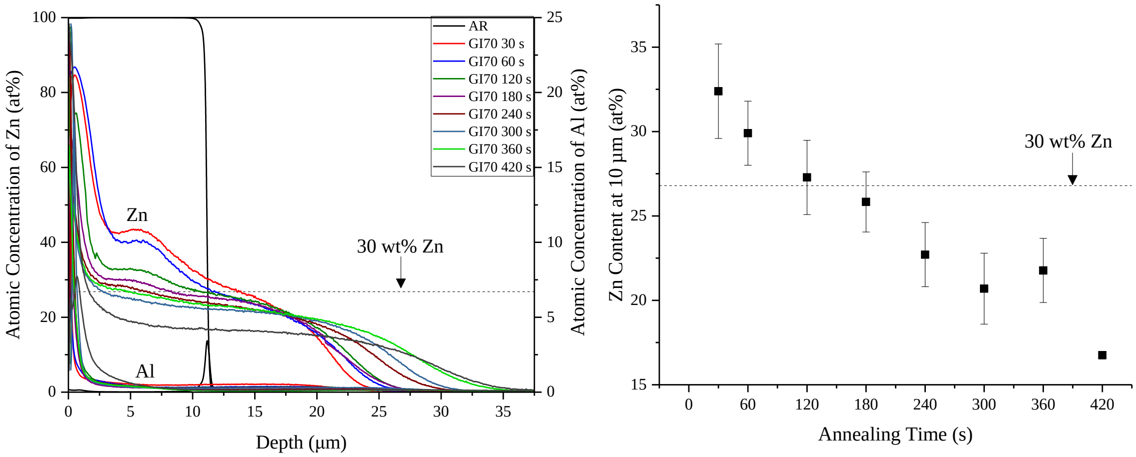

a) b)

Figure 5.4: GDOES analysis results for samples annealed at 900°C showing a) depth profile and b) atomic concentration of Zn at a depth of 10 µm as a function of annealing time.

5.1.3 XRD analysis of the coating layer after annealing

The relative phase fractions within the coating layer subsequent to annealing were determined using XRD. Raw XRD spectra of the as-annealed coatings as a function of annealing time at 900°C, as well as a sample held for 60 s at 700°C, are presented in Figure 5.5 and the resultant quantitative phase fractions in the coatings as a function of annealing time are shown in Figure 5.6. It should be noted that the 0 s time within Figure 5.6 are the results from the sample annealed at 700°C for 60 s. The coatings comprised varying fractions of Γ-Fe_3Zn_{10} and α-Fe(Zn) with smaller fractions of ZnO and minor MnO (Figure 5.5). No Al_2O_3 was detected, likely due to the negligible amounts that form in comparison to both ZnO and MnO. When the sample was annealed at 700°C for

60 s (Figure 5.6), the coating was found to be comprised of Γ-Fe_3Zn_{10} with minor fractions of α-Fe(Zn) and ZnO. These results indicate that, prior to passing through the peritectic temperature, the coating has completely transformed to Γ-Fe_3Zn_{10} and contained no other Fe-Zn intermetallic phases (ie. ζ-$FeZn_{13}$ or δ-$FeZn_{10}$). It was found that as annealing times at 900°C increased, the relative fraction of Γ-Fe_3Zn_{10} decreased while the amount of α-Fe(Zn) increased in a commensurate manner. In addition, the amount of oxides present also increased as annealing times increased; this was more clearly seen with the increase in ZnO with increasing annealing time. These results are consistent with the data obtained from GDOES (Figure 5.4), which indicated a decrease in global Zn content as a result of the overall decrease of Γ-Fe_3Zn_{10}. It should be noted that the presence of Γ-Fe_3Zn_{10} in the room temperature coatings is indicative of the presence of Zn(Fe) liquid in the coating at 900°C, which solidified to Γ-Fe_3Zn_{10} as the coating passed through the 782°C peritectic temperature during cooling, per Figure 2.5 [32].

Further examination of Figure 5.6 shows that the phase fraction of Γ-Fe_3Zn_{10} in the coating decreased to approximately zero for annealing times at 900°C of 240 s or greater, with the coating principally comprising α-Fe(Zn) for longer annealing times, indicating that there was no longer any Zn(Fe) liquid present in the equivalent 900°C microstructures. Furthermore, an examination of Figure 5.5 shows that the peaks associated with α-Fe(Zn) shifted slightly to the right with both an increase in annealing temperature and annealing time, indicating that the Zn concentration within α-Fe(Zn) was decreasing. This latter observation is consistent with the diffusion-based growth mechanism of this phase, particularly following the exhaustion of the diffusible Zn supply upon the disappearance of the Zn(Fe) liquid phase from the 900°C microstructures [13]. These results are consistent with the GDOES results (Figure 5.4), which indicated that the bulk Zn content was less than 30 wt% after annealing for 240 s at 900°C.

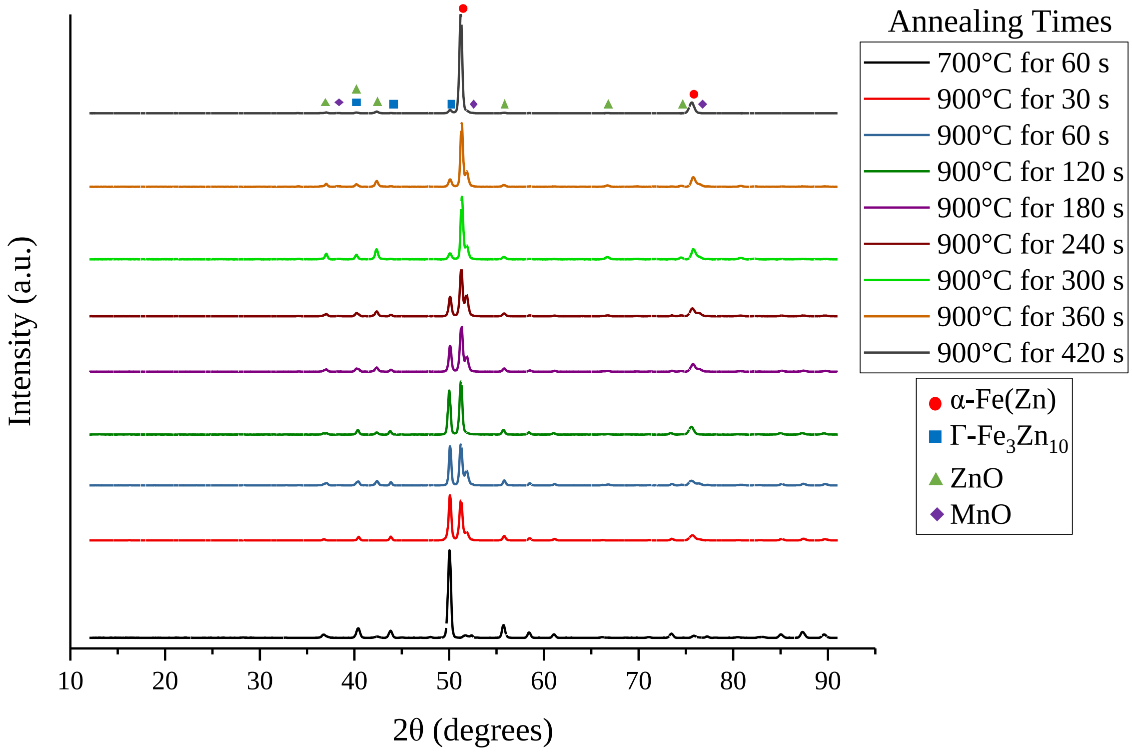

Figure 5.5: XRD spectra of as-annealed coatings as a function of annealing time at 900°C.

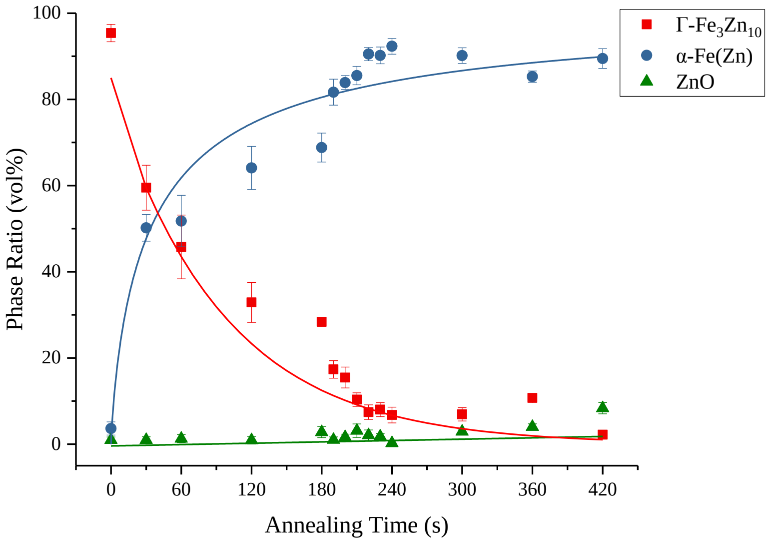

Figure 5.6: XRD phase analysis results at 900°C with a 95% confidence interval.

The XRD results were used to determine the bulk composition of the coating, as seen in Figure 5.7. Detailed calculations may be found in Appendix B. It can be seen that as annealing time increased, the global Zn content decreased until it was less than 30 wt% when the sample was annealed for 240 s or longer. These results are consistent with those found from GDOES (Figure 5.4). As the previous XRD data (Figure 5.6) indicated that samples annealed for 240 s or longer contained only α-Fe(Zn), it can be stated that the α-Fe(Zn) does not meet the theorized minimum requirement of a Zn content of 30 wt% necessary for robust cathodic protection [2, 4, 8]. However, further electrochemical testing is required to confirm this hypothesis.

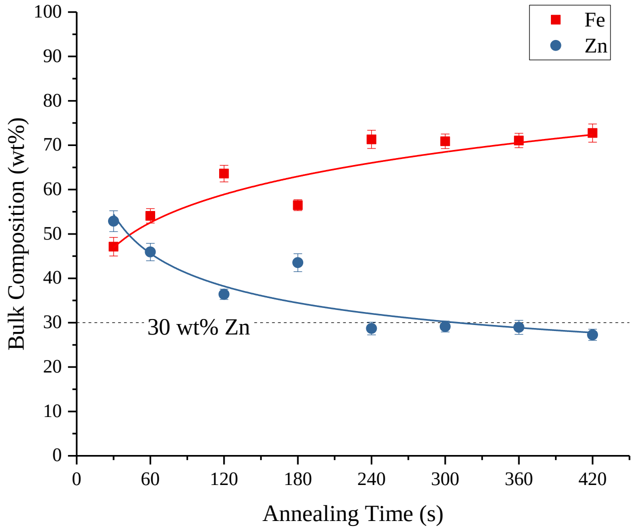

Figure 5.7: Bulk composition of GI70 coatings as a function of annealing time at 900°C with a 95% confidence interval, as determined by XRD analysis.

5.1.4 SEM analysis of the coating layer after annealing

SEM was performed to assess the microstructural evolution of the coatings as a function of annealing time. It should be stated that all images were taken using BSE imaging mode, and as a result, higher average atomic number phases will appear lighter. Figure 5.8 shows the cross-sectional image of the AR coating. It can be seen that the coating is only 10 µm thick, consistent with the GDOES results (Figure 5.4), and is comprised of η-Zn. A layer separating the coating and the substrate material can also be seen, and is attributed to the presence of $Fe_2Al_5Zn_x$, which inhibits the growth of Fe-Zn intermetallics during dipping [23, 24]. Figure 5.9, in contrast, shows the change in coating morphology when the sample is annealed at 700°C for 60 s. The lighter phase within the coating layer is Γ-Fe_3Zn_{10}, and the darker phase is α-Fe(Zn) as it is enriched in Fe. The $Fe_2Al_5Zn_x$ layer is no longer present due its breakdown as a result of outbursts of Fe-Zn intermetallics at higher temperatures [35]. Due to the lack of $Fe_2Al_5Zn_x$, outward diffusion of Fe occurs into the Zn coating. As a result, the coating thickness was found to have increased, and the coating's chemistry has been altered such that the coating is now largely comprised of Γ-Fe_3Zn_{10}. These results are consistent with the XRD findings (Figure 5.6), and further confirms that the coating has completely transformed to Γ-Fe_3Zn_{10} prior to passing through the peritectic temperature [7].

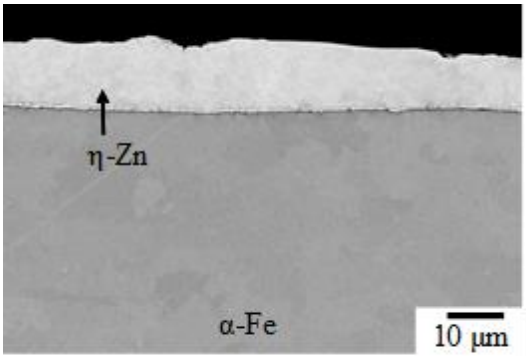

Figure 5.8: Cross-sectional BSE SEM image of AR GI70 sample.

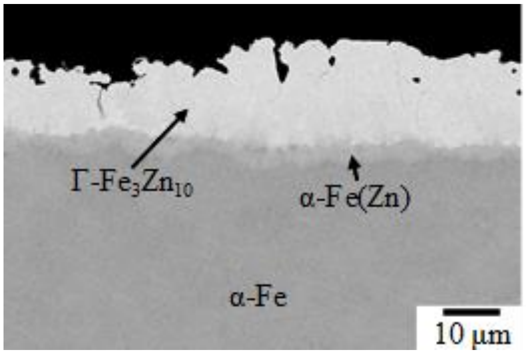

Figure 5.9: Cross-sectional BSE SEM image of GI70 coating annealed at 700°C for 60 s.

Figure 5.10 depicts the microstructural evolution of the coating after annealing at 900°C for varying annealing times. Due to the fact that Γ-Fe_3Zn_{10} is liquid at the annealing temperature, the majority of this phase tends to be concentrated towards the surface of the coating. As annealing times increased, the amount of Fe(Zn) liquid decreased as it is consumed by α-Fe(Zn) until it is no longer present. This phenomenon is evident within Figure 5.10, whereby the volume fraction of Γ-Fe_3Zn_{10} within the coating layer decreased as annealing time increased until it was no longer detected after 240 s of annealing. These observations are consistent with that seen from XRD, presented in Figure 5.6.

It should also be noted that, similar to the sample annealed at 700°C for 60 s, all annealing times at 900°C resulted in an increase in coating thickness in comparison to the AR material, where the AR GI70 coating had an overall thickness of 10 μm (Figure 5.4, Figure 5.8). After 30 s of annealing, the average coating thickness was found to be approximately 25 μm, and after annealing for 420 s, the average coating thickness increased to approximately 40 μm. This change in coating thickness is resultant of the diffusional-based growth mechanism of the α-Fe(Zn) phase as it forms by counter-diffusion of Zn into the Fe substrate [35, 37], and is consistent with the GDOES (Figure 5.4) and XRD (Figure 5.5, Figure 5.6) findings that average Zn concentration within α-Fe(Zn) decreases with increasing annealing time. A wavy oxide layer can also be seen after long annealing times, and consists predominantly of ZnO with minor fractions of MnO. This layer can be seen to be slightly detached from the coating, owing to the poor cohesion between Fe-Zn intermetallics and metallic oxides [2].

As with XRD (Figure 5.7), SEM was also used in order to determine the global Zn content within the coating layer, the results of which are presented in Figure 5.11. It can be seen that, when the sample had been annealed for 240 s and contained only α-Fe(Zn), the overall Zn content within the coating layer was approximately 30 wt%, which has been proposed to be the minimum content within the phase to achieve cathodic protection [2, 4, 8]. These results differ slightly from that determined using XRD analysis (Figure 5.7), though the overall trend is similar: samples annealed for 180 s or less meet the minimum Zn content required for robust cathodic protection, while samples annealed for 240 s or longer are just on the cusp or do not meet the minimum theorized threshold value of Zn content to achieve robust cathodic protection.

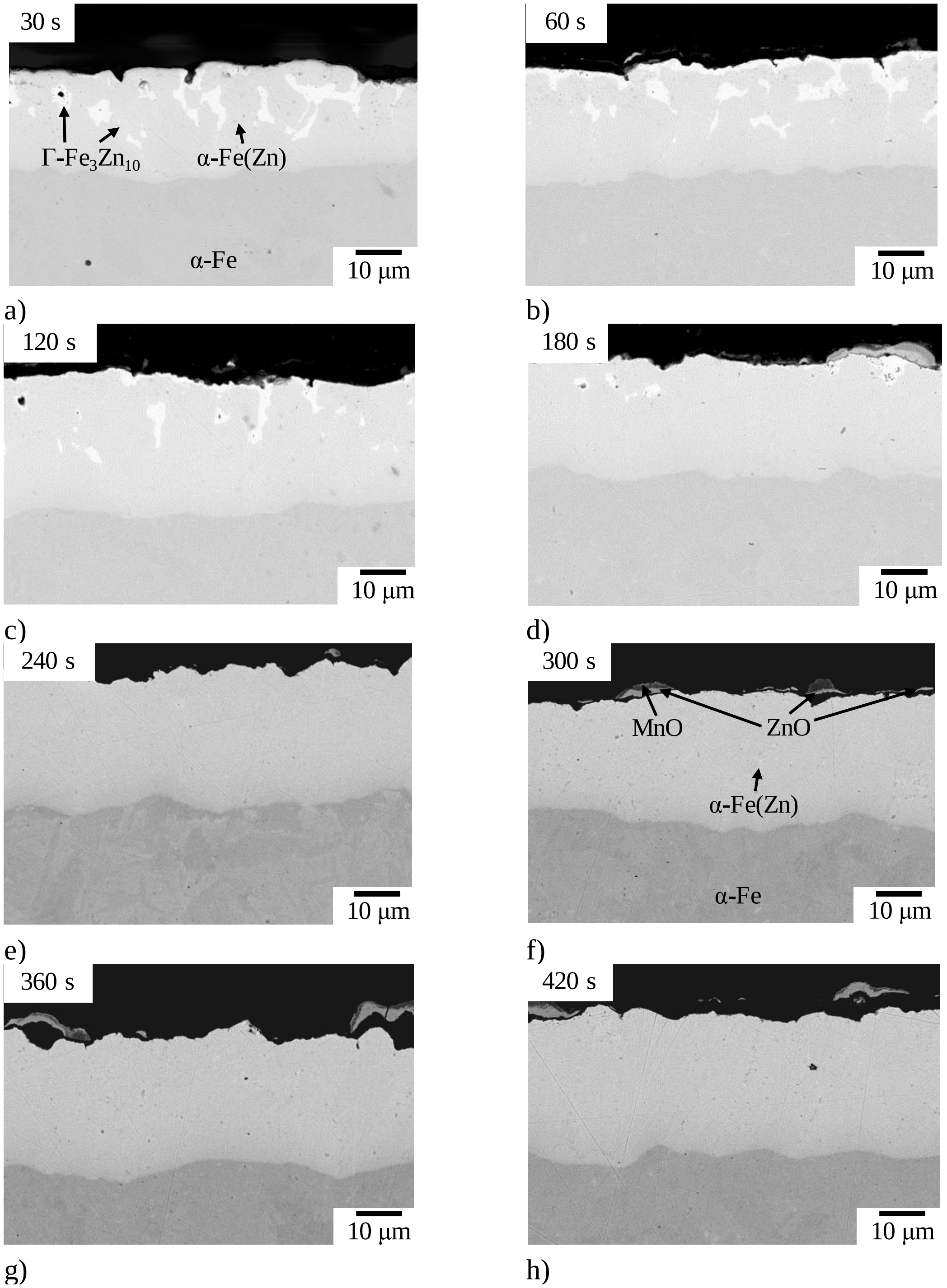

Figure 5.10: Cross-sectional BSE SEM images of GI70 coatings annealed at 900°C for a) 30 s, b) 60 s, c) 120 s, d) 180 s, e) 240 s, f) 300 s, g) 360 s and h) 420 s.

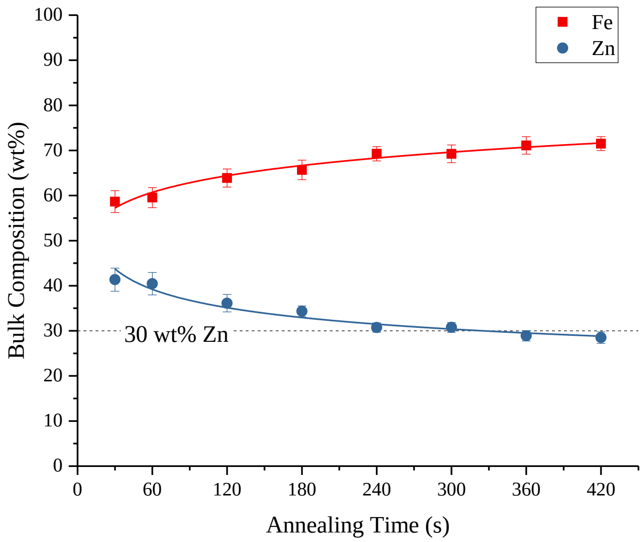

Figure 5.11: Bulk composition of GI70 coatings as a function of annealing time at 900°C with a 95% confidence interval, as determined by SEM analysis.

As discussed previously in §3 it was hypothesized that there would exist a critical volume fraction of Γ-Fe_3Zn_{10} within the coating layer required to provide robust cathodic protection. As a result of GDOES (Figure 5.4), XRD (Figure 5.6), and SEM (Figure 5.10) analyses, it was theorized that this critical Γ-Fe_3Zn_{10} content would lie somewhere between annealing times of 180 s and 240 s and, as such, five additional annealing times were analyzed: 190 s, 200 s, 210 s, 220 s, and 230 s. The BSE cross-sectional images for annealing times within the hypothesised "transition window" can be seen in Figure 5.12. However, it is clear from these images that all annealing times within the transition window contain a significant volume fraction of Γ-Fe_3Zn_{10} within the coating layer, while after 240 s of annealing Γ-Fe_3Zn_{10} is no longer present. Therefore, the first annealing time where no Fe(Zn) liquid was present at the austentizing and forming temperatures was 240 s.

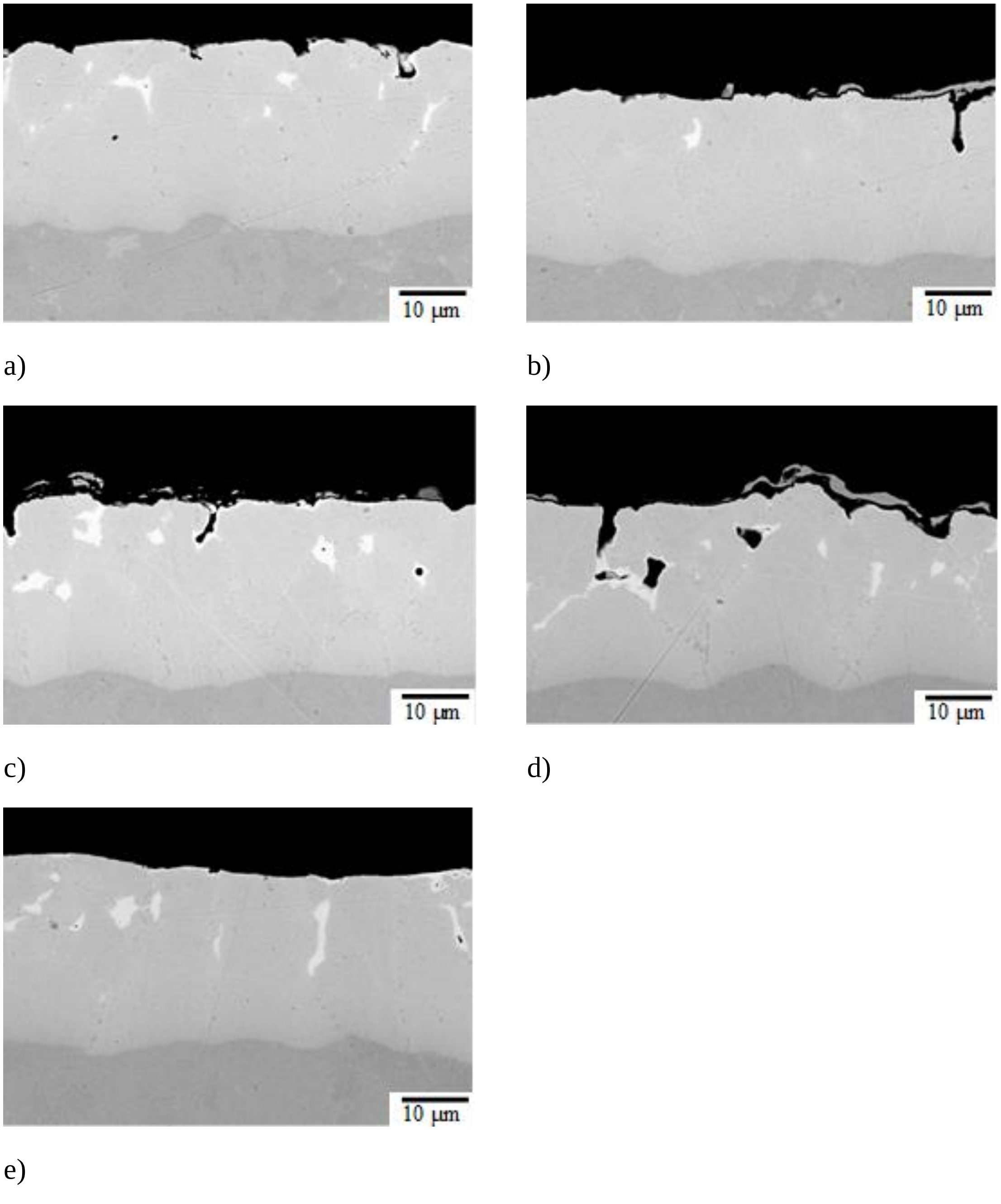

Figure 5.12: Cross-sectional BSE SEM images of GI70 coated samples annealed at 900°C for a) 190 s, b) 200 s, c) 210 s, d) 220 s, and e) 230 s.

5.1.5 SAM-AES analysis of the coating layer in plan view after annealing

In order to assess the area fractions of Γ-Fe_3Zn_{10} and α-Fe(Zn) present on the exposed surface that would initially come into contact with the electrolyte, SAM-AES was used. Plan view images of the coating layer for annealing times of 30 s and 420 s are depicted in Figure 5.13 and Figure 5.14, respectively. For all other annealing times, please refer to Appendix B. It should be noted that minor amounts of O are present within the Auger maps; this is a result of mechanical grinding to remove loose oxides present on the surface, and Ar etching within the Auger to remove all remaining oxide to assess the surface chemistry of the coating. Furthermore, as a result of the removal of the oxide layers, no significant Al was detected and was, therefore, omitted from all analyses.

In assessing Figure 5.13, hot spots of both Zn and Fe were detected on the sample surface. Zn-rich areas are attributed to Γ-Fe_3Zn_{10} being present on the coating layer surface (as seen in the SEM results presented in Figure 5.10), while Fe-enriched areas indicate the presence of α-Fe(Zn). These findings indicate that a high area fraction of Γ-Fe_3Zn_{10} were present on the initial exposed surface. These results are consistent with both XRD (Figure 5.6) and SEM (Figure 5.10) findings, where it was found that the sample contained approximately 52 wt% Γ-Fe_3Zn_{10}. Analyses conducted on the areas representative of α-Fe(Zn) indicated Fe contents of 64 wt% and Zn contents of 36 wt%.

In contrast, it can be seen from Figure 5.14 that there is no longer any Γ-Fe_3Zn_{10} present within the coating; instead, the Auger map detected a relatively constant amount of Fe present on the sample surface. Surface analyses performed on this sample revealed that the average Fe content was approximately 72 wt%, while the average Zn content was approximately 28 wt%. This Zn content is lower than that determined from the phase diagram (Figure 2.5) [32] for the phase at 900°C (around 40 wt% Zn) and lower than that seen in Figure 5.13, indicating that as annealing times increase, α-Fe(Zn) moves further away from saturation and becomes enriched in Fe. These results are consistent with the decreased Zn contents as a result of increasing annealing time found in the GDOES results (Figure 5.4).

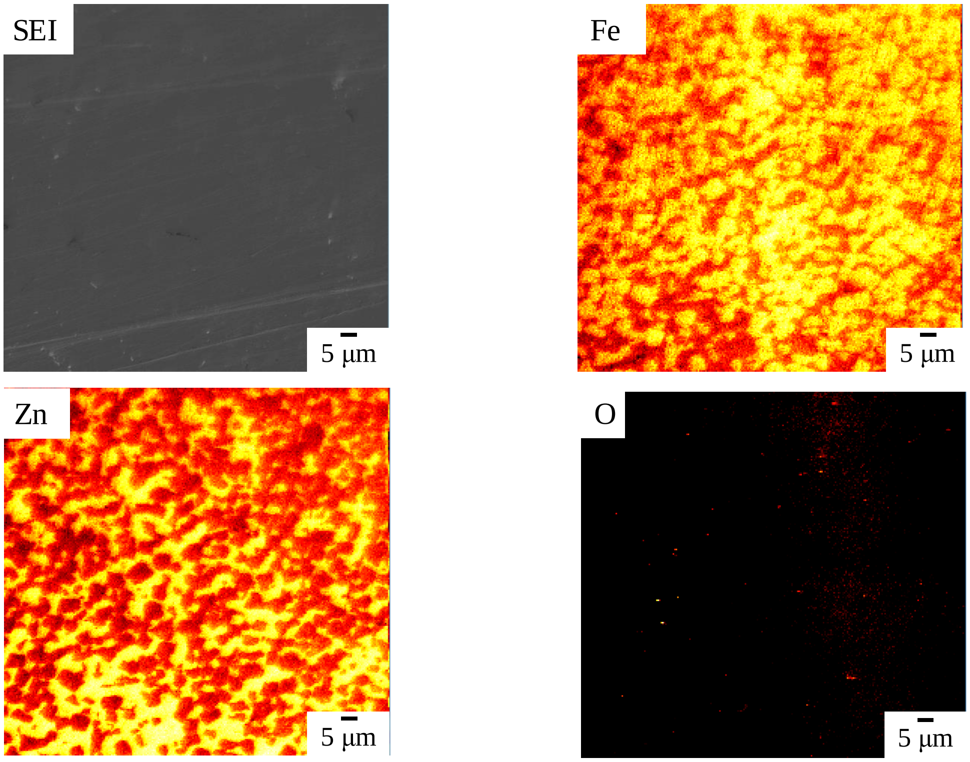

Figure 5.13: SAM-AES elemental mapping of a GI70 sample annealed for 30 s at 900°C in plan view.

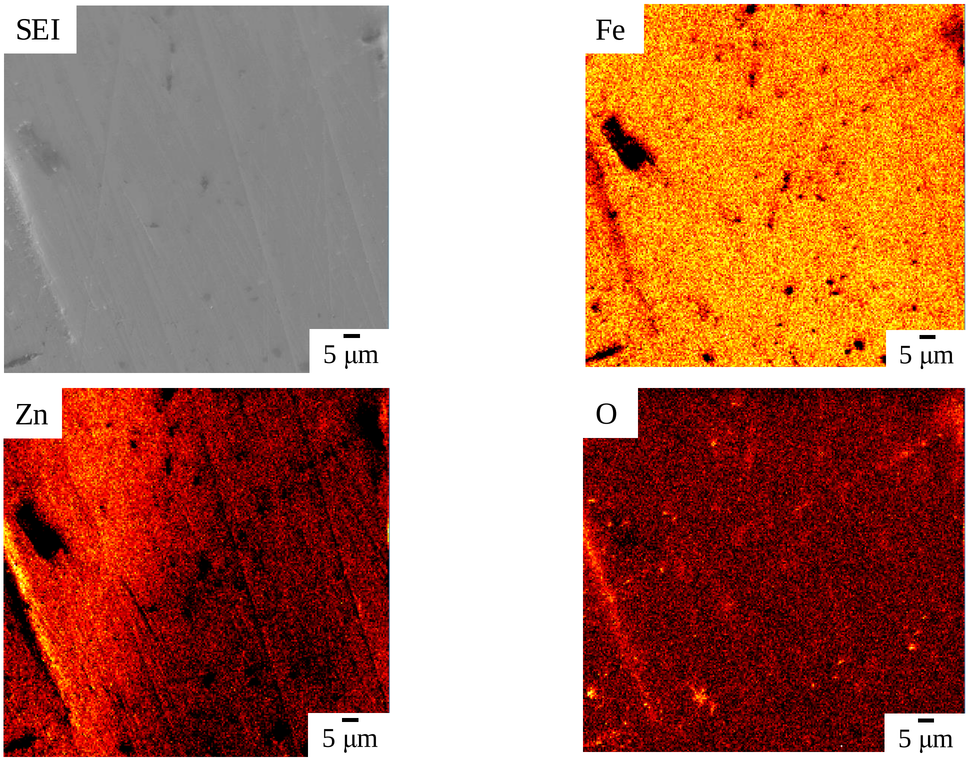

Figure 5.14: SAM-AES elemental mapping of a GI70 sample annealed for 420 s at 900°C in plan view.

Figure 5.15 presents a summative plot of the area fraction of Γ-Fe_3Zn_{10} present on the as-annealed coating surface as a function of annealing time at 900°C. It can be seen that, as annealing time increases, the overall fraction of Γ-Fe_3Zn_{10} decreases until it is no longer present on the surface after 240 s. These results are consistent with the global phase fractions of Γ-Fe_3Zn_{10} within the coating layer as determined by XRD and presented in Figure 5.6.

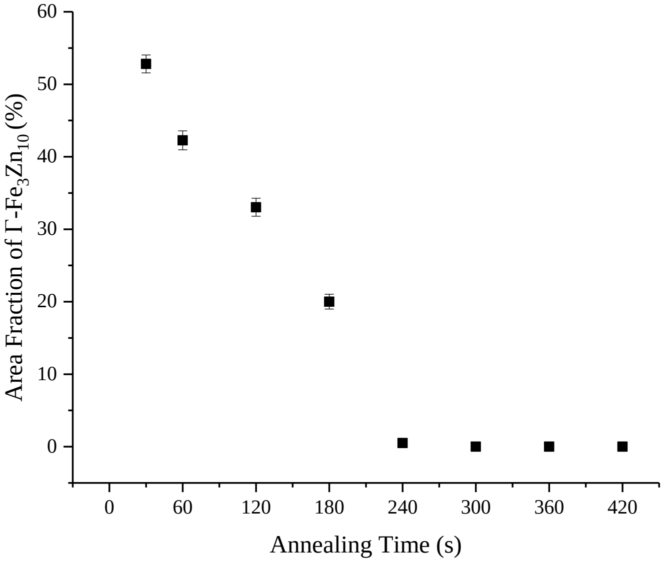

Figure 5.15: Area fraction of Γ-Fe_3Zn_{10} present on the as-annealed coating surface as a function of annealing time at 900°C.

5.2 Coating electrochemical properties

A series of electrochemical tests were performed to determine how the morphology of the coating affected the electrochemical properties. The purpose of this work was to determine the coating microstructure necessary to achieve robust cathodic protection.

5.2.1 Open circuit potential

Prior to the start of all electrochemical tests, samples were held at OCP for 600 s to allow for the metallic interface to reach equilibrium with the electrolyte. However, the free corrosion potentials obtained from these tests allows for further insight into how the coating behaves when it is in contact with the electrolyte. It should be noted that the OCP for the uncoated 22MnB5 substrate was found to be −0.69 V_{SCE}; this datum may be found within

Appendix C. The collected results for specific annealing times can be found in Figure 5.16; for all remaining annealing times, please refer to Appendix C. All annealed coated samples were found to be cathodic with regards to the AR GI70 coated coupon and anodic in comparison to the uncoated 22MnB5. It was found that all coatings required 600 s to equilibrate with the electrolyte. Three main groupings can be seen in Figure 5.16: coatings annealed for 210 s or less, including the sample annealed at 700°C for 60 s, had steady-state OCP values more active than $-0.81\ V_{SCE}$; coatings annealed between 220 s and 240 s had equilibrium OCP values more cathodic than $-0.81\ V_{SCE}$ but more active than $-0.73\ V_{SCE}$ whereas coatings annealed for 300 s or longer had equilibrium OCP values more cathodic than $-0.73\ V_{SCE}$.

A summative plot of the steady-state OCP values taken at 600 s, presented in Figure 5.17, clearly delineates these specific groupings as a function of the overall fraction of Γ-Fe_3Zn_{10} in the coating. It can be seen in Figure 5.17 that the steady-state OCP values of the annealed coatings increased slightly as the phase ratio of Γ-Fe_3Zn_{10} decreased until the fraction of Γ-Fe_3Zn_{10} dropped below 10 vol%. Once the phase ratio of Γ-Fe_3Zn_{10} within the coating was less than 10 vol%, a substantial increase in the steady-state OCP value was found which was very sensitive to the fraction of Γ-Fe_3Zn_{10}. This rapid OCP transition is directly correlated to the appearance of the α-Fe(Zn)-only coatings, as seen in Figure 5.6. From Figure 5.17, it can be seen that the OCP values within this region are in close proximity to that of the uncoated 22MnB5 substrate, indicating that the cathodic protection, if any, offered by these coatings will likely be minor.

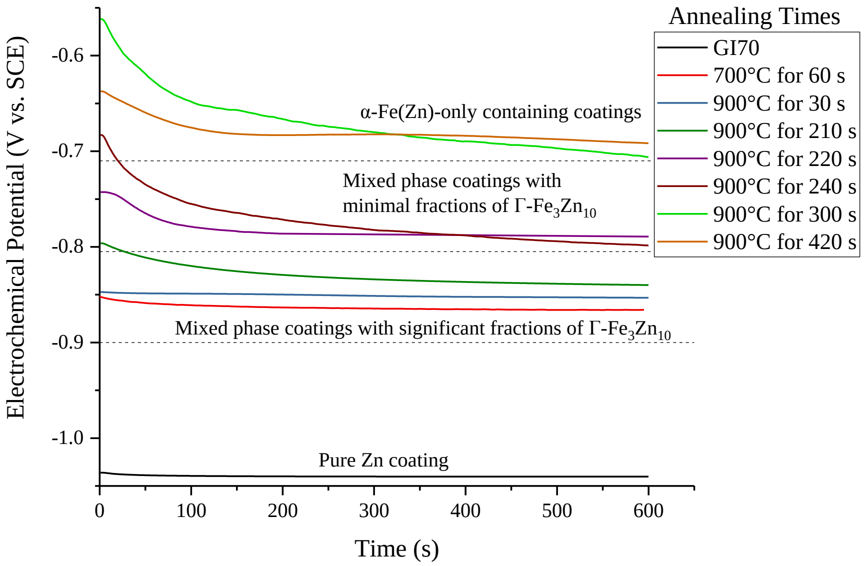

Figure 5.16: OCP results for GI70 coated samples as a function of annealing time.

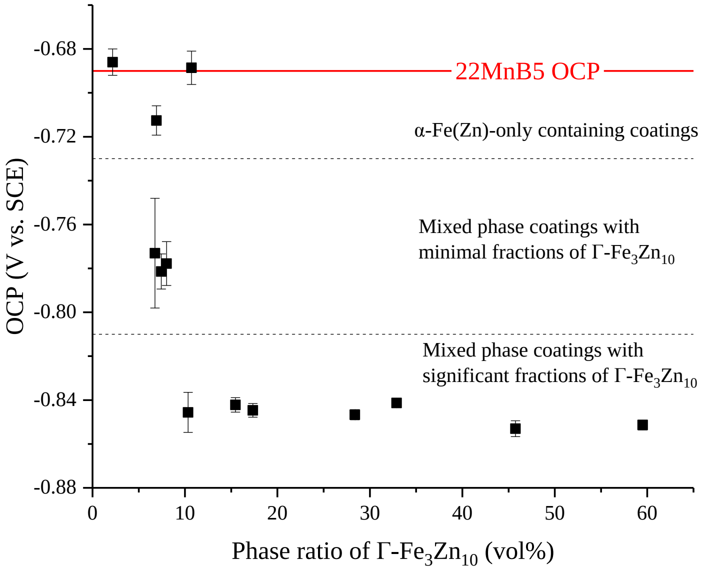

Figure 5.17: Summative plot of steady-state OCP values after 600 s as a function of the phase fraction of Γ-Fe_3Zn_{10}.

5.2.2 Potentiodynamic polarization scans

Figure 5.18 displays the potentiodynamic polarization scans obtained for the bare 22MnB5 substrate, the as-received GI70 coating and the annealed GI70 coatings. It should be noted that not all annealing times are included within this graphic to distinguish between the different annealing times; for a full set of potentiodynamic polarization curves, please refer to Appendix C. Potentiodynamic polarization scans were used to determine the preliminary electrochemical properties as a result of the varying coating morphologies. It can be seen that all annealed samples (regardless of annealing temperature) possessed corrosion potentials (E_{corr}) between both the AR GI70 coating and the uncoated 22MnB5 substrate material, and clusters formed as a result of coating morphology. The coupon that had been annealed at 700°C for 60 s was found to have an E_{corr} of approximately $-0.85\ V_{SCE}$, owing to the presence of Γ-Fe_3Zn_{10} in direct contact with the electrolyte. A secondary anodic region (depicted by the "nose" in the scan occurring at approximately $-0.57\ V_{SCE}$) can be seen within the scan, and is attributed to the dissolution process of α-Fe(Zn). Due to the fact that this portion occurs at a potential more noble than the E_{corr} of the substrate material, it is unlikely that the presence of α-Fe(Zn) within the coating contributed significantly to the cathodic protection of the substrate. Further assessment of Figure 5.18 reveals the presence of a limiting cathodic current density, which is hypothesized to be due to the formation of stable Zn-based corrosion products [43, 69, 76, 93].

Figure 5.18 shows that coupons annealed at 900°C that had some significant fraction of Γ-Fe_3Zn_{10} present within the coating layer – i.e. annealed for 300 s or less – clustered at approximately the same E_{corr} found for the coating that contained 100% Γ-Fe_3Zn_{10}: −0.85 V_{SCE}. In comparison, annealed coupons with the single-phase α-Fe(Zn) coating i.e. annealed for 360 s and greater, had an E_{corr} of approximately −0.72 V_{SCE}. The Ecorr results are directly related to the microstructure of the coating, and agree with the general trends seen in Figure 5.16 and Figure 5.17. Similar to the above observations for the 100% Γ-Fe_3Zn_{10} coating, mixed phase coatings were found to possess a secondary anodic region indicative of the dissolution of α-Fe(Zn) (Figure 5.18). This feature was found to become more active as the overall fraction of Γ-Fe_3Zn_{10} within the coating decreased until it was nearly coincident with the E_{corr} of α-Fe(Zn)-only coatings: approximately −0.71 V_{SCE}. This feature indicates that the dissolution kinetics of α-Fe(Zn) within mixed phase coatings is rapid due to the high current density. In further assessment of Figure 5.18, a limiting current density within the cathodic region was observed for samples annealed for 300 s or less, but this behaviour was not found to be present for samples annealed for 360 s or more. As this feature was also observed for the sample annealed at 700°C for 60 s, it was hypothesized that this phenomenon was linked to the presence of Γ-Fe_3Zn_{10} within the coating layer.

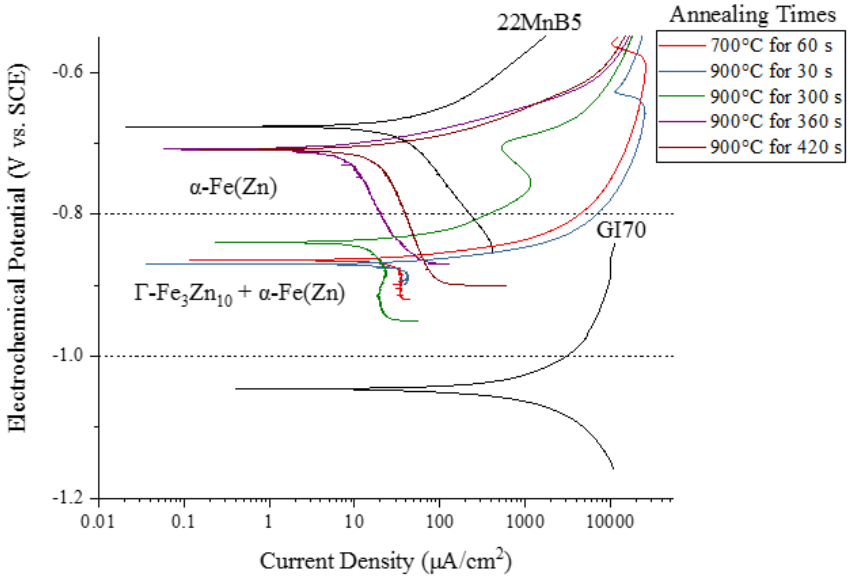

Figure 5.18: Potentiodynamic polarization scans for samples annealed at 900°C.

In an attempt to better characterize the theorized critical volume fraction of Γ-Fe_3Zn_{10}, potentiodynamic polarization scans were also performed for samples within the transition window, the results of which can be seen in Figure 5.19. As was expected from the results in Figure 5.18, all samples had an E_{corr} of approximately −0.85 V_{SCE} owing to the Γ-Fe_3Zn_{10} towards the surface of the coating being in contact with the electrolyte. These results are consistent with the fact that Γ-Fe_3Zn_{10} tends to segregate towards the surface edge of the coating (Figure 5.12), but do not correlate with the OCP values observed in Figure 5.16. Similar to the previous results, all annealing times had a secondary anodic region approximately coincident to the E_{corr} determined for α-Fe(Zn). The potential at which this secondary anodic portion occurred was found to grow slightly more active as annealing times increased. Furthermore, a limiting current density was observed for all annealing times within the transition window, potentially due to the presence of Γ-Fe_3Zn_{10}. However, due to the fact that the E_{corr} was found to be relatively constant between all annealing times, the critical volume fraction of Γ-Fe_3Zn_{10} within the annealed coatings was unable to be determined from these results. As such, further testing was necessary to determine the minimum threshold value for robust cathodic protection.

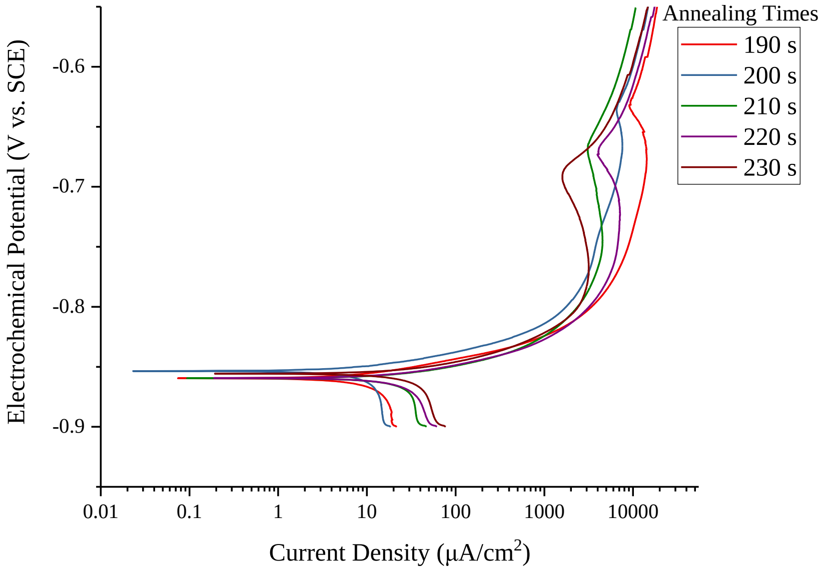

Figure 5.19: Potentiodynamic polarization scans for samples annealed at 900°C within the transition window.

The summative results of E_{corr} as a function of coating annealing parameters are presented in Figure 5.20 (a). It can be seen that the E_{corr} of the coating layer after 360 s is in relatively close proximity to the uncoated 22MnB5 substrate material. In contrast, there is a larger difference in the E_{corr} associated with coating layers that have been annealed for 300 s or less, indicating a significantly larger thermodynamic driving force for cathodic protection. Figure 5.20 (b) shows how the phase fraction of Γ-Fe_3Zn_{10} within the coating layer affected E_{corr}. There exists a sharp transition in behaviour between the two E_{corr} regimes, however, the exact nature of this transition point cannot be clearly determined by potentiodynamic polarization scans. This transition occurs when the fraction of Γ-Fe_3Zn_{10} is close to zero, indicating that samples that comprise of a single-phase coating (α-Fe(Zn)) provide a diminished driving force for robust cathodic protection.

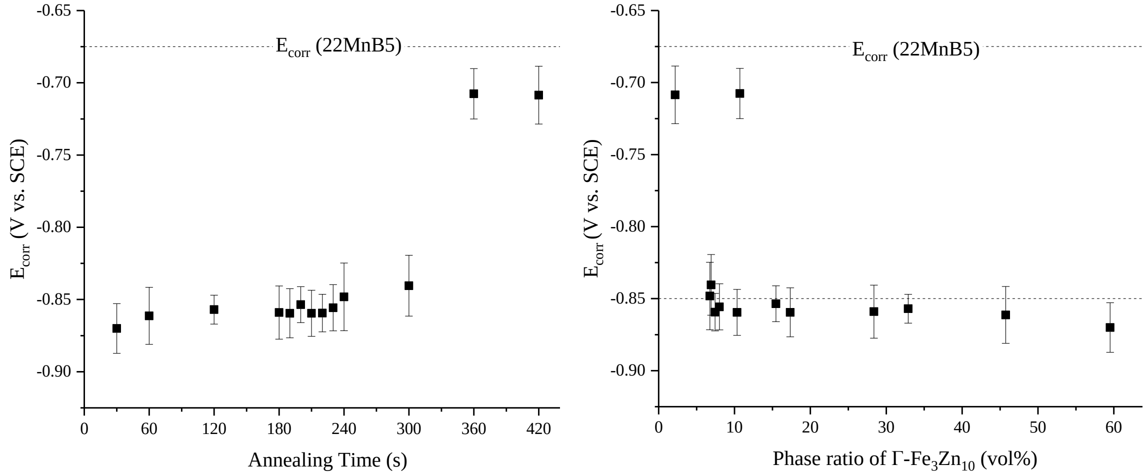

a) b)

Figure 5.20: Changes in E_{corr} as a function of a) annealing time at 900°C and b) phase ratio of Γ-Fe_3Zn_{10}.

5.2.3 Galvanostatic polarization transients

To better delineate the electrochemical properties of both coating phases, galvanostatic polarization tests were performed, the results of which are depicted in Figure 5.21. For reference, both an AR sample and a sample annealed at 700°C for 60 s were tested. It should be noted that not all annealing times are included within the report to improve resolution of the graphic; a full set of data can be seen in Appendix C.

It should first be stated that, when considering Figure 5.21, the AR coating appears to have full dissolution of the coating occur at a more rapid rate in comparison to the annealed samples. This is mainly attributed to the overall coating thickness, where the AR coating was 10 µm in thickness versus the annealed coatings, which were 25 µm to 40 µm in thickness (Figure 5.4). Additionally, a potential overshoot was observed for the AR sample once it reached the electrochemical potential associated with the 22MnB5 substrate material. This is likely owing to the $Fe_2Al_5Zn_x$ interfacial layer's dissolution; as the $Fe_2Al_5Zn_x$ layer was not present within the annealed samples, this overshoot was not seen for the samples annealed at 900°C.

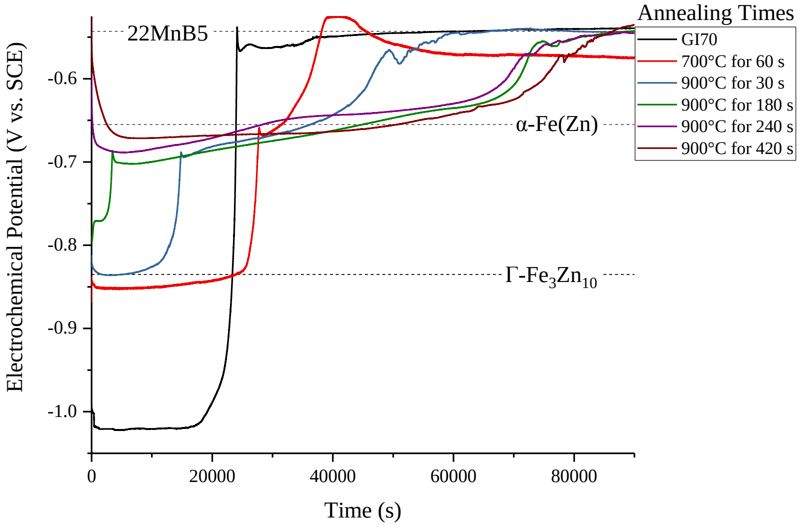

Figure 5.21: Galvanostatic polarization transients for GI70 samples annealed at 700°C and 900°C at an applied current density of +1 mA/cm^2.

As can be seen in Figure 5.21, the sample annealed at 700°C for 60 s was found to possess three distinct dissolution potentials, indicative of the anodic dissolution of Γ-Fe_3Zn_{10}, α-Fe(Zn), and the uncoated substrate material in order of increasing nobility. The longer dissolution time of Γ-Fe_3Zn_{10} was consistent with the increased coating thickness of this coating (15 μm) in comparison to the AR coating (10 μm), as seen in Figure 5.9. Due to the fact that the coating largely consists of Γ-Fe_3Zn_{10}, the dissolution potential was found to remain constant for its entire duration. In contrast, the dissolution time of α-Fe(Zn) was extremely short as the layer was quite thin, as seen in Figure 5.9, and was found to increase rapidly in potential as the phase dissolved. This is a result of a compositional gradient existing within the phase such that the Zn content is highest at the Γ-Fe_3Zn_{10}/α-Fe(Zn) interface and gradually depleted towards the α-Fe(Zn)/substrate interface. These results are in good agreement with the GDOES data presented in Figure 5.4.

As can also be observed in Figure 5.21, the mixed phase coatings obtained at 900°C were also found to contain three potential arrests of –0.835 V_{SCE}, –0.655 V_{SCE}, and –0.54 V_{SCE}, coincident with the dissolution of Γ-Fe_3Zn_{10}, α-Fe(Zn) and finally the 22MnB5 substrate, respectively, as documented above for the 700°C × 60 s coatings. It was found that the dissolution potential associated with Γ-Fe_3Zn_{10} was more noble in comparison to that found for the 700°C × 60 s coatings. This is due to the fact that, at 700°C, Γ-Fe_3Zn_{10} has a higher Zn content than when it is formed at 900°C [35]. Similar to the nearly 100%

Γ-Fe_3Zn_{10}-coating, the dissolution plateau potential indicative of α-Fe(Zn) was found to increase during dissolution. The increasing potential observed is likely linked to the decreasing Zn content of this coating, as can be seen in the GDOES profiles (Figure 5.4). Furthermore, this effect was found to be greatest for the sample annealed for 30 s and negligible for the sample annealed for 420 s, a result of increased diffusion times leading to the thicker coatings observed in Figure 5.10. Therefore, corrosion rates are not directly correlated to the time it takes to reach the potential associated with the uncoated substrate material but the i_{corr} values for each coating phase, as will be discussed in more detail in §6.2. It was also found that the duration of the dissolution arrest indicative of Γ-Fe_3Zn_{10} decreased as annealing time increased such that the plateau was no longer present after 240 s of annealing.

In an attempt to determine the hypothesized critical fraction of Γ-Fe_3Zn_{10}, samples taken from within the transition window of annealing times of 190 s to 230 s underwent galvanostatic polarization testing, the results of which are displayed in Figure 5.22. As galvanostatic scans are quite sensitive to surface morphology, it was assumed that the sample that possessed the shortest possible dissolution plateau indicative of Γ-Fe_3Zn_{10} would also contain the critical volume fraction necessary for robust cathodic protection. Similar to the observations in Figure 5.21, three dissolution plateaus associated with Γ-Fe_3Zn_{10}, α-Fe(Zn), and the substrate were present for samples that had been annealed for 210 s or less, while samples annealed for 220 s or 230 s only displayed the dissolution plateaus associated with α-Fe(Zn) and the substrate. These results were interesting as SEM analysis (Figure 5.12) had revealed that all samples within the transition window contained a significant fraction of Γ-Fe_3Zn_{10}. Resultant of this data, it can be inferred that the critical Zn content or fraction of Γ-Fe_3Zn_{10} necessary within the coating layer to achieve robust cathodic protection occurred at an annealing time of 210 s. Correlation of this result with the XRD results in Figure 5.6 indicates that the volume fraction of Γ-Fe_3Zn_{10} within the 900°C × 210 s coating was approximately 10 vol%.

Furthermore, it can be seen from Figure 5.22 that the dissolution plateau indicative of α-Fe(Zn) for samples annealed within the transition window was found to rise as dissolution time increased. As such, it can be inferred that a compositional gradient exists within α-Fe(Zn) such that the Zn content towards the surface of the coating is higher than that adjacent to the coating/substrate interface. This further confirms the finding that a fully saturated α-Fe(Zn) will not be able to provide robust cathodic protection, especially when it is recalled that, when the dissolution plateau of α-Fe(Zn) was constant and indicative of a fully saturated phase, GDOES found that α-Fe(Zn) contained less than 30 wt% Zn (Figure 5.4).

The dissolution time of Γ-Fe_3Zn_{10} as a function of the overall fraction of Γ-Fe_3Zn_{10} within the coating is presented in Figure 5.23. It can be seen that dissolution time decreases in a linear fashion. From this figure, it can be seen that the lowest possible fraction of Γ-Fe_3Zn_{10} that corresponds to a dissolution arrest is 10 vol%, consistent with an annealing time of 210 s at 900°C as seen in XRD (Figure 5.6).

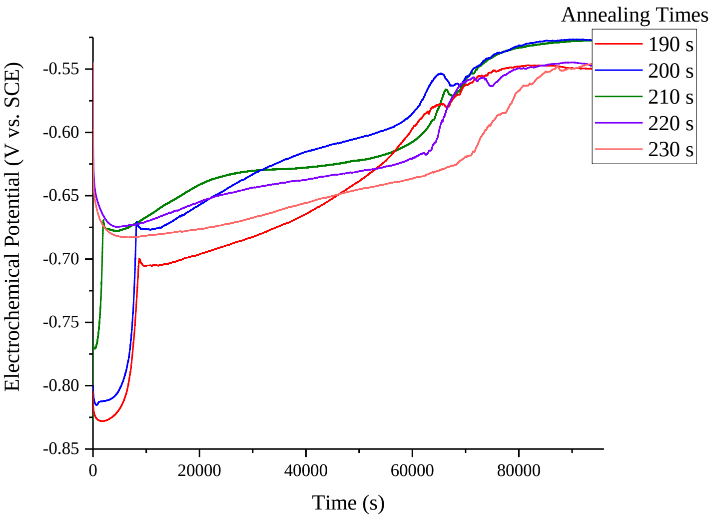

Figure 5.22: Galvanostatic polarization transients for GI70 samples annealed at 900°C within the transition window at an applied current density of +1 mA/cm^2.

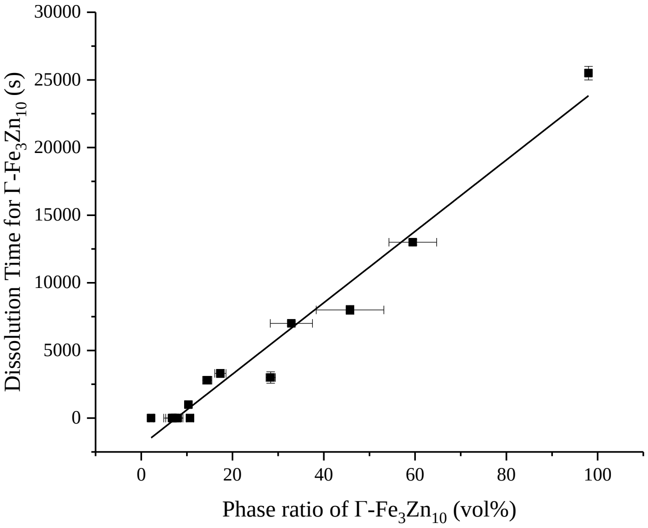

Figure 5.23: Dissolution time of Γ-Fe$_3$Zn$_{10}$ as a function of the overall fraction of Γ-Fe$_3$Zn$_{10}$ within the coating.

5.2.4 Potentiostatic testing

Potentiostatic tests were conducted to allow for further analysis into the comparison of the electrochemical properties of Γ-Fe_3Zn_{10} and α-Fe(Zn). Three potentials were chosen to encompass the cathodic and anodic regions within the potentiodynamic polarization curves (Figure 5.18) for both coating phases: −0.97 V_{SCE}, −0.77 V_{SCE}, and −0.61 V_{SCE}. These values were chosen such that they would be ±0.10 V_{SCE} in comparison to the E_{corr} determined for both phases. Both the 120 s and 420 s annealing times can be seen in Figure 5.24 below; for all other annealing times, please refer to Appendix D. As anticipated, when the 120 s coupon was held at a potential within the cathodic region at −0.970 V_{SCE}, no coating attack was observed, as seen in Figure 5.24 (e). However, when the sample annealed for 120 s was held at −0.770 V_{SCE}, within the anodic region, preferential dissolution of Γ-Fe_3Zn_{10} was seen to occur (Figure 5.24 (c)). This was, again, expected as this potential was anodic in relation to the E_{corr} determined for Γ-Fe_3Zn_{10}. At this stage, no attack to either α-Fe(Zn) nor the substrate material was seen. Further dissolution of the coating occurred when the sample was held at −0.610 V_{SCE}, and it can be seen that dissolution of α-Fe(Zn) had occurred in Figure 5.24 (a). Again, no substrate attack was observed; it can thus be stated that the coating obtained after annealing for 120 s dissolved at a relatively slow rate.

When the coupon annealed for 420 s was subjected to potentials within the cathodic region, −0.970 V_{SCE} and −0.770 V_{SCE}, no dissolution of the coating layer occurred, as can be seen in Figure 5.24 (d) and (f). However, substantial coating damage was seen in

Figure 5.24 (b) when the sample was held at −0.610 V_{SCE}, which was +0.10 V_{SCE} above the E_{corr} of α-Fe(Zn); this is a result of the rapid changes to the anodic current when the sample is polarized above E_{corr}. Furthermore, substrate attack was observed in localized areas throughout the cross-section, indicating rapid dissolution of the α-Fe(Zn) coating layer despite its increased coating thickness in comparison to the sample annealed for 120 s. Unlike the sample annealed for 120 s, no corrosion products were observed when the sample was annealed for 420 s regardless of applied potential (Figure 5.24 (b), (d), and (f)). As a result, it is not the thickness that plays a predominant role in the effectiveness of the coating to provide protection to the underlying substrate material, but the composition itself of the coating and the formation of passivating corrosion products. More specifically, the same conclusion as previously drawn can be stated, such that a critical fraction of Γ-Fe_3Zn_{10} must be present within the coating layer to provide a sufficient Zn content to achieve robust cathodic protection.

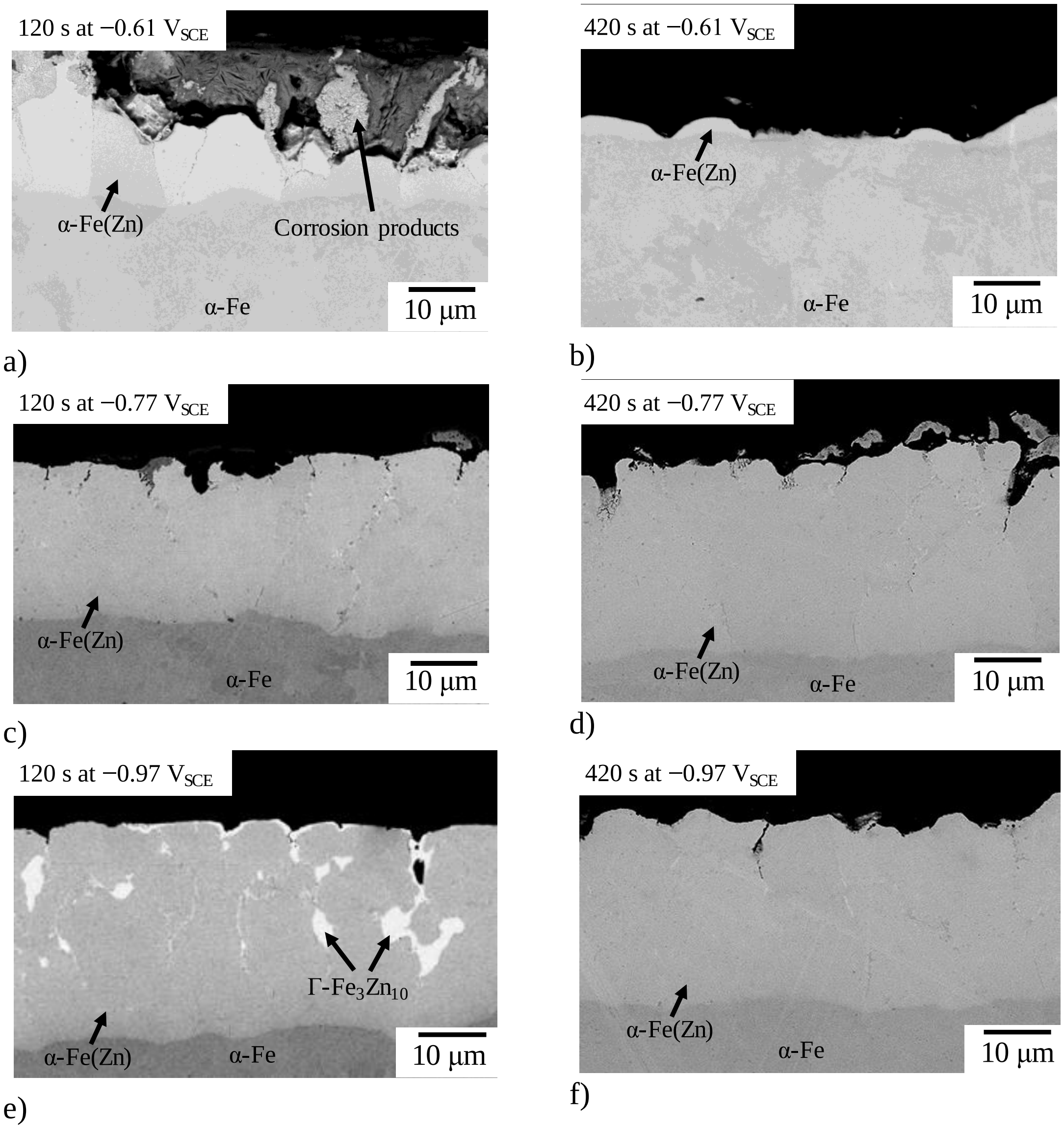

Figure 5.24: Cross-sectional BSE SEM images after potentiostatic testing at for a a) GI70 sample annealed at 900°C for 120 s held at −0.61 V$_{SCE}$, b) GI70 sample annealed at 900°C for 420 s held at −0.61 V$_{SCE}$, c) GI70 sample annealed at 900°C for 120 s held at −0.77 V$_{SCE}$, d) GI70 sample annealed at 900°C for 420 s held at −0.77 V$_{SCE}$, e) GI70 sample annealed at 900°C for 120 s held at −0.97 V$_{SCE}$, and f) GI70 sample annealed at 900°C for 420 s held at −0.97 V$_{SCE}$.

5.2.5 XRD analysis of interrupted galvanostatic polarization transients

In order to determine the corrosion products resulting from the selective dissolution of Γ-Fe_3Zn_{10} arising during the galvanostatic transients, "interrupted" galvanostatic polarization transients were performed such that testing was completed once the Γ-Fe_3Zn_{10} dissolution plateau had been completed and the dissolution plateau for α-Fe(Zn) began. Based upon previous literature, it was anticipated that specific corrosion products would form as a result of environmental factors and coating morphology [69, 76]. The XRD results of the corrosion product analysis can be seen in Figure 5.25.

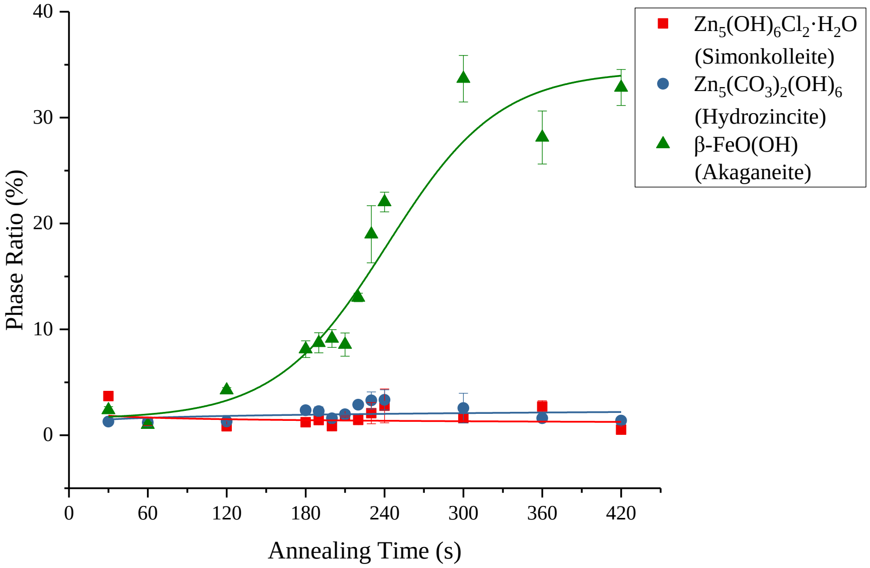

Figure 5.25: XRD phase analysis of corrosion product formation during interrupted galvanostatic polarization testing at +1 mA/cm^2.

All XRD analyses detected negligible amounts of β-$ZnCl_2$, and as such it was omitted from Figure 5.25. The three corrosion products that formed were resultant of the coating microstructure and environmental factors. Hydrozincite was found to have formed as a result of higher fractions of Γ-Fe_3Zn_{10} leading to increased Zn contents within the coating layer and the naturally aerated condition of the tests [69]. Simonkolleite, while also a result of higher Zn contents within the coating, formed due to the chloride-containing corrosive environment [43, 69, 76]. Finally, akaganeite formed as a result of increased Fe contents within the coating layer [43, 93]. From the figure, a rapid change in slope can be seen between annealing times of 180 s and 240 s, specifically at 220 s, likely due to the significantly reduced fraction of Γ-Fe_3Zn_{10} present within the coating layer after annealing for 220 s (Figure 5.25). Furthermore, the overall formation of akaganeite plateaued after the sample was annealed for 360 s and the coating microstructure was 100% α-Fe(Zn).

Figure 5.26 presents the fraction of formed corrosion products as a result of the fraction of Γ-Fe_3Zn_{10} within the coating layer from the interrupted galvanostatic transients. It can be seen that the fraction of corrosion products increased substantially once the volume fraction of Γ-Fe_3Zn_{10} dropped below 10 vol%, consistent with the galvanostatic data (Figure 5.21, Figure 5.22). Furthermore, it can be seen that the dominant corrosion product changes from hydrozincite and simonkolleite at high Zn contents to akaganeite as Zn content decreases. Thus, when considering the potentiostatic results presented in Figure 5.24, it is likely that the corrosion products seen for the sample annealed for 120 s were stable, passivating, Zn-based corrosion products. This is also likely to be the reason for the observed cathodic limiting current density observed in the potentiodynamic polarization scans (Figure 5.18, Figure 5.19).

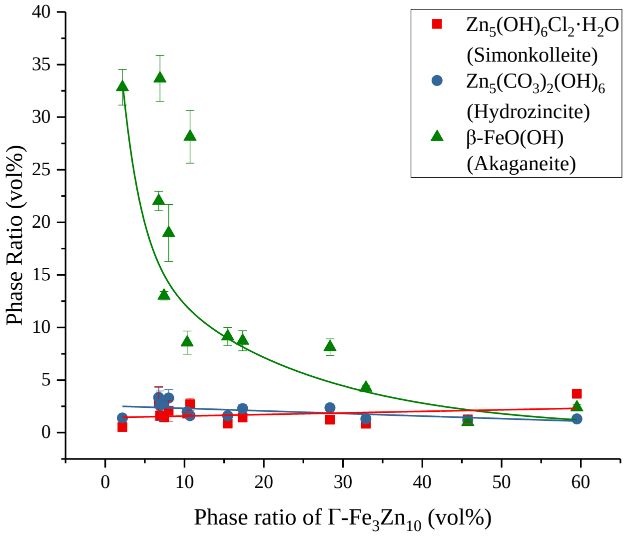

Figure 5.26: Phase ratio of corrosion products as a function of global Zn content within the coating layer.

5.2.6 SEM analysis of interrupted galvanostatic polarization transients

It is important to assess how the coating microstructure evolved during dissolution of both coating phases throughout the galvanostatic polarization measurements. As a result, interrupted galvanostatic scans were performed such that three new dissolution times were considered and the coating microstructures assessed. These tests were performed on a sample annealed at 900°C for 30 s, as it would have the highest fraction of Γ-Fe_3Zn_{10}, the results of which are presented in Figure 5.27.

Consideration of Figure 5.27 (a) shows only localized dissolution of Γ-Fe_3Zn_{10} to have occurred. Voids within the coating correlated to preferentially dissolved grains of Γ-Fe_3Zn_{10}; however, as this test was only run to halfway through the dissolution plateau, some Γ-Fe_3Zn_{10} remained. The α-Fe(Zn) remained untouched, which was expected as its

E_{corr} is more noble in comparison to the E_{corr} determined for Γ-Fe_3Zn_{10} (Figure 5.18). Figure 5.27 (b), in contrast, depicts complete dissolution of Γ-Fe_3Zn_{10} such that no significant amount was detected using SEM techniques. Preferential dissolution of α-Fe(Zn) in areas that were in direct contact with the electrolyte can be seen to have occurred. Corrosion attack areas appears to be more localized, resulting in the appearance of voids within the coating layer. Figure 5.27 (c) shows more advanced attack of α-Fe(Zn), where certain areas have dissolved more rapidly than others. This is potentially due to the compositional gradient within the phase, whereby areas that were more rich in Zn would dissolve sooner than areas more enriched in Fe, as seen in the GDOES (Figure 5.4), XRD (Figure 5.5), and galvanostatic scan (Figure 5.21) results. However, no substrate attack was observed at this stage; it is anticipated that substrate damage would only occur once the entire coating layer had dissolved. This is a result of the sacrificial nature of Zn, whereby it would galvanically corrode to protect the more noble substrate material even if the Fe was exposed directly to the corrosive environment. Therefore, the coating layer will continue to provide corrosion protection to the substrate until it was no longer present.

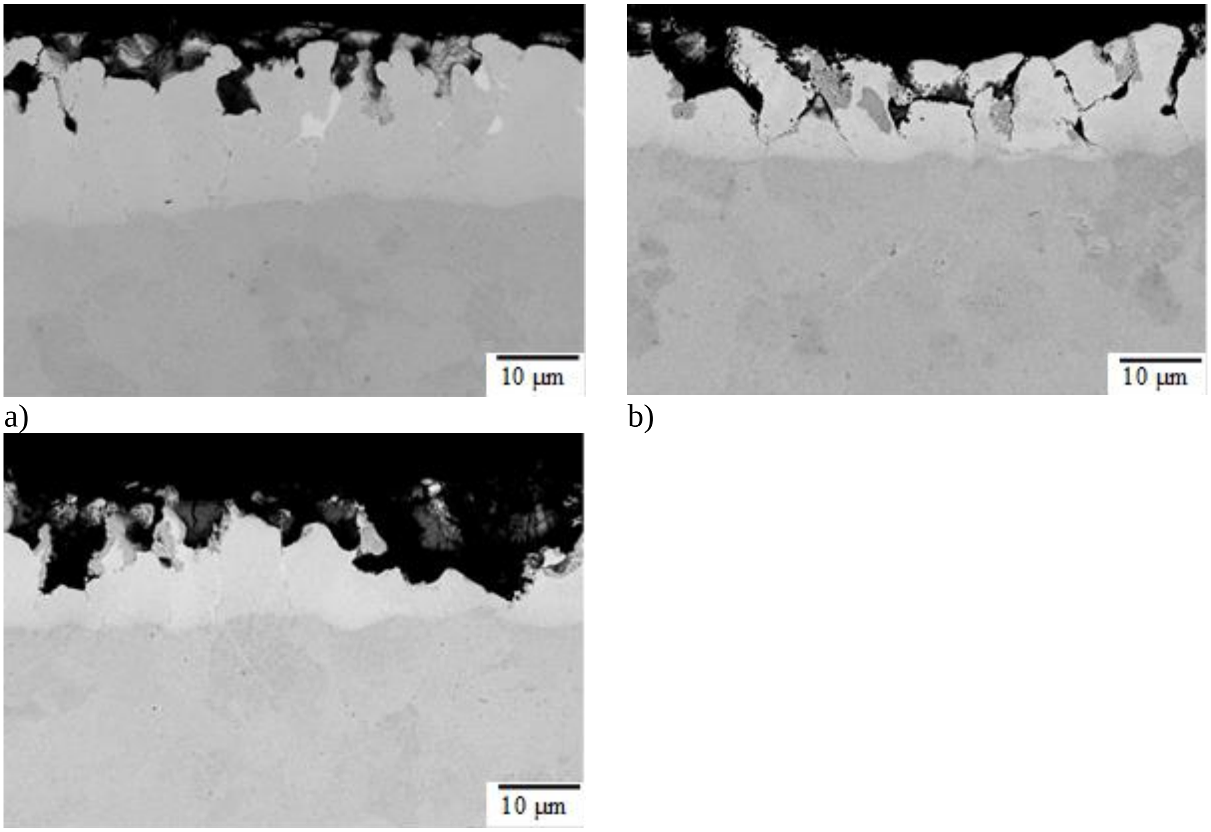

a)

b)

c)

Figure 5.27: Cross-sectional BSE-SEM images of a coupon annealed for 30 s at 900°C subjected to interrupted galvanostatic polarization testing at +1 mA/cm^2 for a) halfway through the Γ-Fe_3Zn_{10} dissolution plateau, b) immediately after the Γ-Fe_3Zn_{10} dissolution plateau, and c) halfway through the α-Fe(Zn) dissolution plateau.

5.2.7 SAM-AES analysis of interrupted galvanostatic polarization transient samples in cross-section

To identify the formed corrosion products and to better represent Cl, SAM-AES analysis was used. Cross-sections, as seen in Figure 5.28 and Figure 5.29, were used to better resolve the low concentrations and small dimensions of corrosion products. It should be noted that only samples annealed for 30 s and 240 s are included within the body of the report, while the remaining annealing times can be found in Appendix D. The presence of S within the maps was likely a result of the addition of $ZnSO_4$ to the electrolyte.

Assessment of Figure 5.28 reveals relatively high concentrations of C and Cl penetrating down the coating layer, indicative of the presence of hydrozincite and simonkolleite, respectively. An evenly thick layer of O can be seen on the surface of the sample, likely a result of the compact morphology of hydrozincite and simonkolleite [43, 94, 95]. This densely packed corrosion product layer would likely lead to a diminished mass transport of oxygen to the sample surface. Furthermore, it is unlikely that significant fractions of akaganeite have formed as no O hot spots correlated to the hot spots of Fe, consistent with the XRD findings (Figure 5.25).

Figure 5.29, in contrast, depicts substantially decreased amounts of C and Cl. No S was detected, and as a result its map was omitted. This is likely due to the fact that hydrozincite and simonkolleite were less likely to form when the coating contained higher amounts of Fe, once again consistent with the XRD (Figure 5.25) results. It can also be seen that more O hot spots coincided with Fe hot spots, indicating a switch in the dominant corrosion products from Zn-based to Fe-based, namely akaganeite. Furthermore, an increased penetration depth of corrosion products in the coating layer can also be seen, indicating increased corrosion susceptibility as Fe content within the coating layer increases. This finding is consistent with the increased formation of corrosion products as annealing time increases, found from the XRD analysis (Figure 5.25).

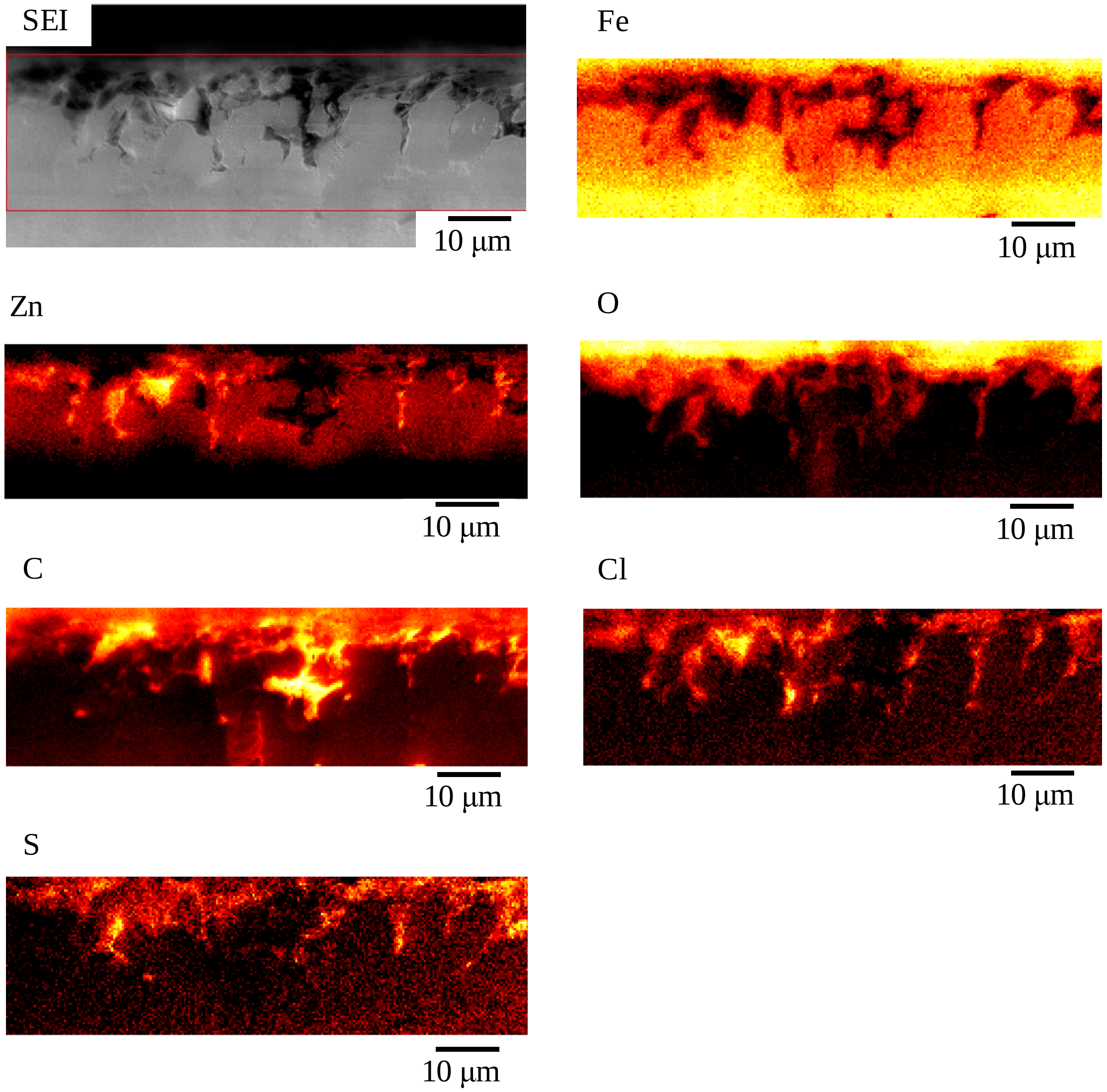

Figure 5.28: Cross-sectional view SAM-AES map images of GI70 sample annealed at 900°C for 30 s.

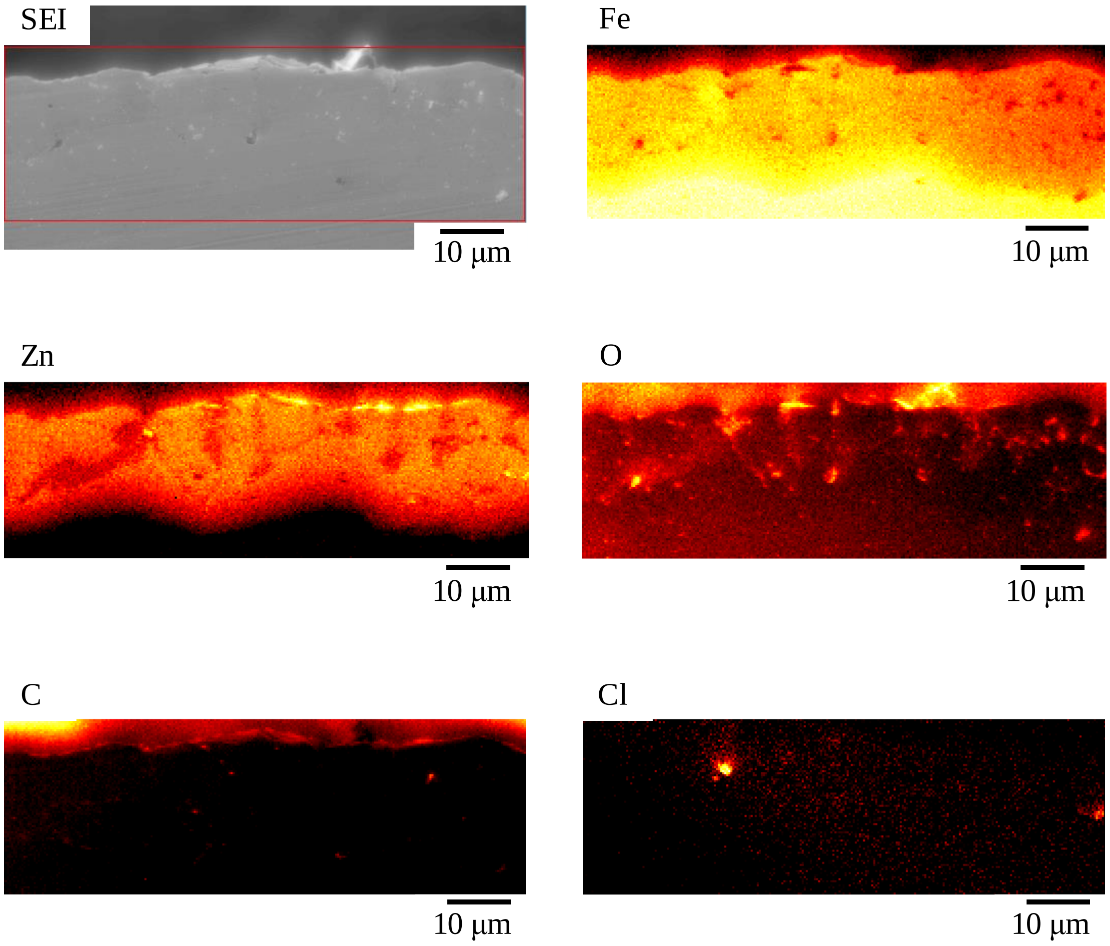

Figure 5.29: Cross-sectional view SAM-AES map images of GI70 sample annealed at 900°C for 240 s.

5.2.8 TEM analysis of interrupted galvanostatic transients

While SAM-AES was able to detect the corrosion products formed, it was unable to spatially resolve them; as a result, the corrosion products were deemed too small to be detectable on the microscale offered by this technique. Thus, TEM analysis was performed to differentiate the formed corrosion products on the nanoscale. The EELS spectra obtained from a sample annealed at 900°C for 60 s that had been subjected to interrupted galvanostatic polarization scans are outlined in Figure 5.30. It should first stated that, as part of the FIB sample fabrication process, C was deposited onto the sample. Due to the extremely low concentrations of Cl within simonkolleite, the C peak overshadowed the Cl peak and, as a result, the presence of simonkolleite could not be determined from this data.

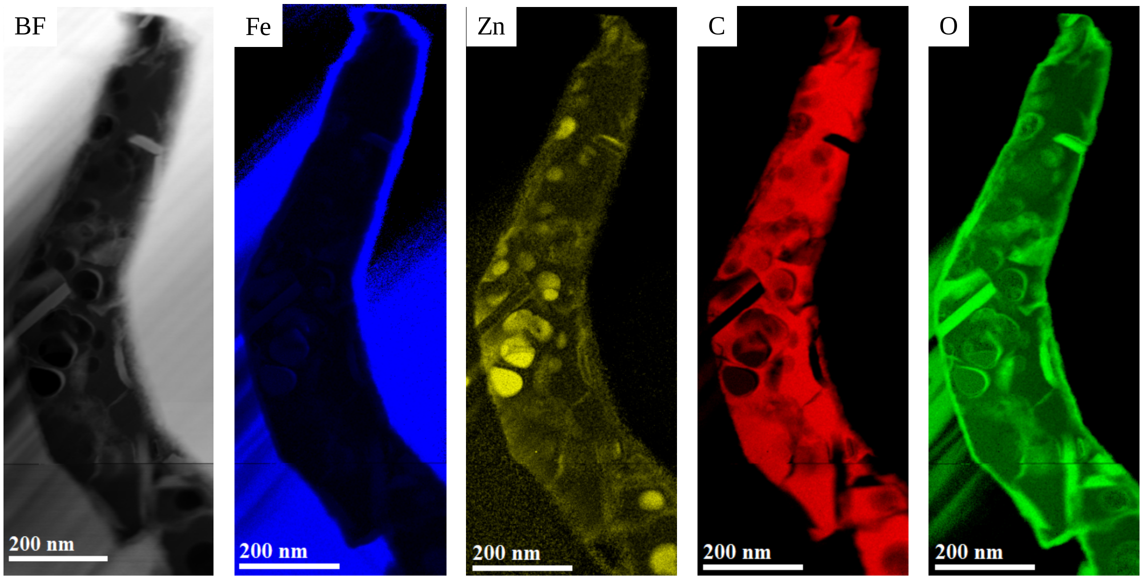

Figure 5.30: HR-TEM EELS map of sample annealed at 900°C for 60 s subjected to interrupted galvanostatic scan depicting the bright field STEM image and the corresponding elemental maps.

Two different morphologies could be detected within the EELS maps (Figure 5.30): one which was more rod-like in appearance, while the other was more disc-like. In consultation with the literature, it was determined that these morphologies coincided with that seen for akaganeite and hydrozincite [96-99], respectively. The presence of these two corrosion products is consistent with that seen in XRD (Figure 5.25). Furthermore, the elemental contrast appears to agree with these findings, where the rod-like structures are rich in Fe and O but devoid of both C and Zn, while the disc-like structures were higher in both Zn and C. The EELS spectra obtained from both of these morphologies can be seen in Figure 5.31, where Figure 5.31 (a) corresponds to the disc-like structures and Figure 5.31 (b) the rod-like structures. Comparison of these spectra to literature further confirmed that the rod-like structures were akaganeite and disc-like structures were hydrozincite [96].

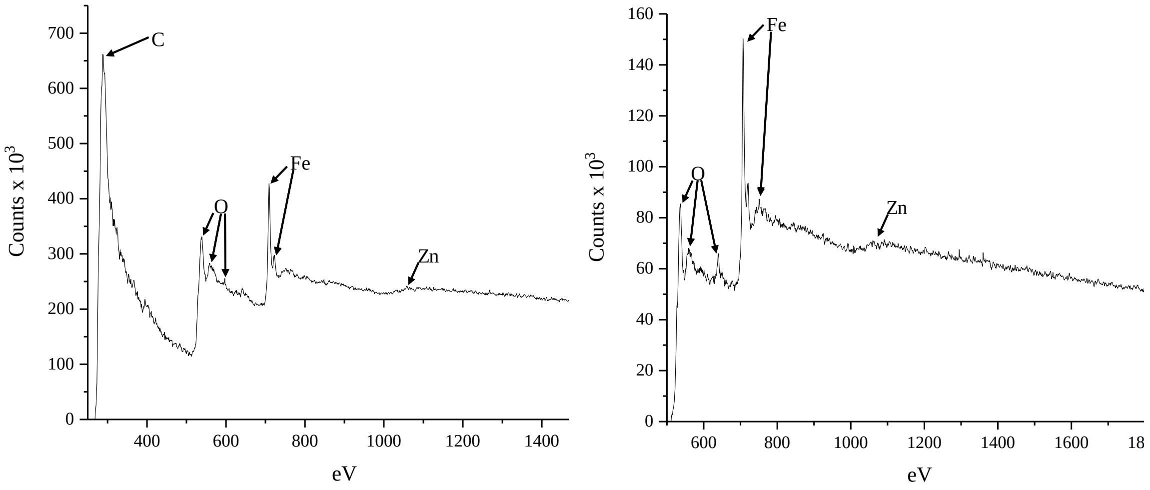

a) b)

Figure 5.31: EELS spectra indicative of a) hydrozincite and b) akaganeite.

5.2.9 Galvanic corrosion measurements

While the previous tests were able to determine how well the overall coating performed in a corrosive environment, none assessed the galvanic protection offered by the coating to the substrate material. As a result, galvanic corrosion measurements were performed by coupling the annealed coating and the uncoated 22MnB5 substrate material through the electrolyte, the results of which are displayed in Figure 5.32. To better differentiate between the varying annealing times, some results were omitted from the plot. For a full set of data, please refer to Appendix D.

Assessment of Figure 5.32 shows that samples that were annealed for 180 s or less reached a constant exchange current density with the substrate material much sooner than samples that were annealed for 240 s or longer. Preliminary steady-state galvanic currents for the samples annealed for 180 s or less were found to be relatively low (less than approximately 17 $\mu A/cm^2$). These low galvanic exchange currents indicate minor galvanic activity. These lower stabilized coupling current densities were a result of the corrosion products predicted to cause the limiting current density observed in Figure 5.18 and Figure 5.19, which were attributed to the presence of stable Zn-based corrosion products. However, it can be seen from Figure 5.32 that, partway through the scan at 46 000 s, the current density for the sample annealed for 180 s increased. The preliminary portion of the curve was found to be consistent with that seen for the sample annealed for 30 s; after the increase, it was found to be coincident to that of the samples annealed for 240 s or longer. It is possible that the Γ-Fe_3Zn_{10} within the coating had fully dissolved, and as a result the cathodically protective phase switched to α-Fe(Zn). At this point, however, a direct conclusion cannot be made and further testing must be performed. The positive current density indicates that all annealed coatings were active in relation to the coupled substrate material, and as a result little corrosion of the substrate material was expected to occur.

Further assessment of Figure 5.32 reveals that the fluctuations in exchanged current density increasedd as a function of annealing time. These larger fluctuations in coupling current density for samples annealed for 240 s or longer have been observed to be indicative of increased corrosion activity [100]. Furthermore, these changes in galvanic current density have also been stated to result from initiation of corrosion in a localized area before ceasing [101].

Figure 5.33 presents the average galvanic coupling currents in the beginning half of the scan once the reading had stabilized (up to 46 000 s) and until the end of the scan (from 46 000 s to 86 400 s). These results indicate that, when the coating contained at least 15 vol% Γ-Fe_3Zn_{10}, the coupled current density was approximately constant throughout the duration of the scan. These values were found to be low, indicating low galvanic activity and thus low corrosion rates, consistent with previous data. When the phase fraction of Γ-Fe_3Zn_{10} was less than 15 vol%, the galvanic activity was found to increase, consistent with the increased corrosion rates observed in previous data.

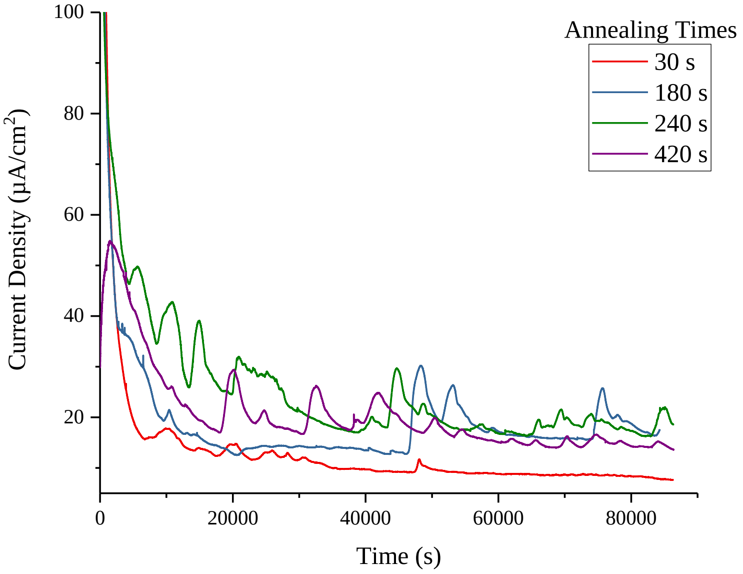

Figure 5.32: Galvanic corrosion scans for GI70 samples annealed at 900°C.

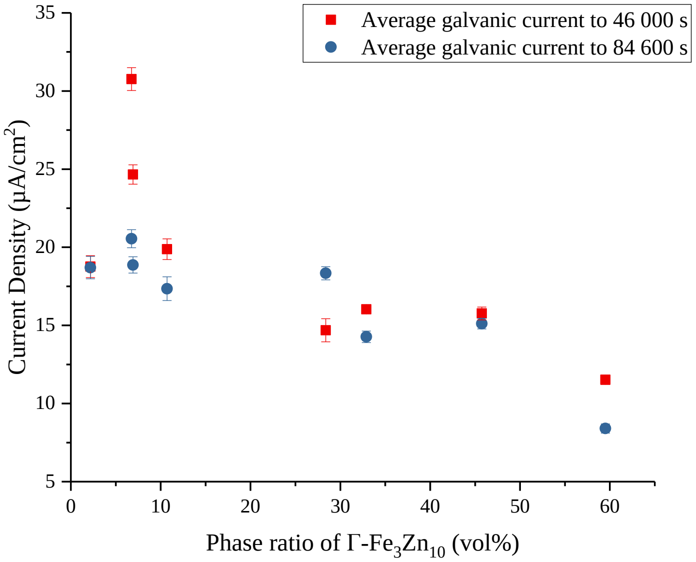

Figure 5.33: Average galvanic current densities as a function of the phase fraction of Γ-Fe_3Zn_{10}.

5.3 Results Summary

Industrially produced GI70 coatings on a 22MnB5 substrate were annealed at 900°C for holding times ranging from 30 s to 420 s in order to assess how the coating morphology changed as a function of annealing time, and how that subsequently affected the electrochemical properties. It was found that the uncoated 22MnB5 substrate material met the mechanical target properties regardless of annealing time. However, when the samples were coated, $\sigma_{(UTS)}$ was found to decrease with increasing annealing times until it was less than 1500 MPa when the sample was annealed at 900°C for 180 s. GDOES analysis revealed that the global Zn content of the coating also decreased as a function of annealing time until it was less than 30 wt% when the sample was annealed 900°C for 240 s. A sample annealed at 700°C for 60 s was found to consist of Γ-Fe_3Zn_{10}, indicating a full transformation of all Fe-Zn intermetallics to Γ-Fe_3Zn_{10} prior to passing through the peritectic temperature at 782°C. When the samples were annealed at 900°C, it was found that coatings comprised of varying fractions of Γ-Fe_3Zn_{10} and α-Fe(Zn). The fraction of Γ-Fe_3Zn_{10} decreased until it was no longer present after the sample was annealed for 240 s, indicating that all of the liquid phase had been consumed at the austenitizing temperature. SAM-AES analysis determined that the fraction of Γ-Fe_3Zn_{10} present on the coating surface decreased until it was negligible when the sample was annealed at 900°C for 240 s.

In the second part of the study, the effect of coating morphology on the electrochemical properties was assessed. Steady-state OCP values taken after 600 s were found to increase as a function of annealing times, with large transitions when samples had been annealed for longer than 210 s at 900°C. The potentiodynamic polarization scans displayed a limiting current density in the cathodic region of the scans when samples contained even minor fractions of Γ-Fe_3Zn_{10}, indicating decreased corrosion rates. Galvanostatic polarization measurements were performed, and found three dissolution arrests, attributed to Γ-Fe_3Zn_{10}, α-Fe(Zn), and the substrate material. The dissolution time for Γ-Fe_3Zn_{10} was found to decrease with increasing annealing times until the sample was annealed for 220 s or longer at 900°C. Thus, it was found that samples needed to contain at least 10 vol% Γ-Fe_3Zn_{10} within the coating microstructure to have a dissolution arrest pertaining to Γ-Fe_3Zn_{10}. Potentiostatic tests determined that the dissolution rate for coatings that contained only α-Fe(Zn) was higher than that found for coatings that contained a mixture of Γ-Fe_3Zn_{10} and α-Fe(Zn). Furthermore, some substrate attack was observed when the sample was annealed at 900°C for 420 s despite the fact that some coating still remained, indicating that the coating was unable to provide adequate cathodic protection. XRD analysis on samples that underwent interrupted galvanostatic scans found that three corrosion products formed: simonkolleite, hydrozincite, and akagneite. The relative fraction of akaganeite increased as annealing times increased, demonstrating a change in the dominant corrosion product from Zn-based to Fe-based. Additionally, it was found that the amount of formed corrosion products increased significantly when the coating contained less than 15 vol% Γ-Fe_3Zn_{10}, signifying the necessity of increased fractions of Γ-Fe_3Zn_{10} within the coating to provide robust cathodic protection. SAM-AES analysis on these samples showed that the Zn-based corrosion products obtained when samples were annealed for 180 s or less at 900°C were more compact in nature than the Fe-based corrosion products that formed when the samples were annealed for 240 s or longer. As a result, it is likely that the Zn-based corrosion products will act as cathodic inhibitors and further decrease the corrosion rates. Spatial resolution of the corrosion products was obtained using TEM analysis, where it was found that both hydrozincite and akaganeite were present on a sample annealed for 60 s, as represented by the globular-like and rod-like morphologies, respectively. Finally, galvanic corrosion measurements found that the galvanic current density increased as annealing time increased, indicative of increased corrosion rates. Furthermore, the amount of noise present in the scans was found to increase as a result of increased annealing times, again resultant of increased corrosion rates when the samples contained less than 15 vol% Γ-Fe_3Zn_{10}.

6 DISCUSSION

The effect of annealing time on the microstructural development and subsequently the electrochemical properties of the coatings was investigated for a GI70 coated 22MnB5 steel grade. Industrially produced GI70 sheets with an initial ferritic-pearlitic microstructure were machined into smaller samples for microstructural and electrochemical testing. Samples were annealed at the standard austenitizing temperature of 900°C and quenched with rapid cooling rates of −75°C/s compatible with the steel grade to obtain a fully lath martensitic microstructure.

6.1 The effect of annealing time on the microstructural and mechanical properties

The results of uniaxial tensile testing (Figure 5.1) on uncoated 22MnB5 indicated that a fully martensitic microstructure was achieved after austenitizing at 900°C and quenching with cooling rates in excess of −75°C/s. This data was found to be consistent with that seen in the microstructural images in Figure 4.1. It can be seen that the AR uncoated 22MnB5 substrate material consisted of a mixture of ferrite and pearlite [102], where pearlite can be identified by the alternating lamellae of cementite (Fe_3C) and ferrite. After austentization and rapid quenching, the microstructure transforms to yield that of lath martensite [102]. All given test results on the uncoated 22MnB5 samples coincided with the industrial target mechanical properties of $\sigma_{(UTS)} \geq 1500$ MPa for a 22MnB5 PHS [36, 103]. However, tensile results (Figure 5.2) obtained after experimental hardening on GI70 coated samples revealed that as annealing time increased, UTS decreased until it no longer met the target UTS of at least 1500 MPa after annealing for 180 s. It is possible that the reduction in UTS was a result of both substrate microcracking and a decreased cross-sectional substrate area to withstand the tensile load, resultant of the fact that α-Fe(Zn) grows due to the inward diffusion of Zn [36, 37]. As Zn is a ferrite stabilizer, transformation to martensite does not occur [36]; therefore, the overall thickness of martensite will decrease as annealing times increase. Moreover, previous research has theorized that Zn enrichment along prior austenitic grain boundaries results in increased susceptibility to microcracking, however, more research must be done to confirm this [59, 104].

The GDOES results (Figure 5.4) found that coating thicknesses increased with increasing annealing time, a result of the inward diffusion of Zn into the substrate material and subsequently the formation of α-Fe(Zn) [13, 37]. As-annealed coupons were found to have coating thicknesses between 25 μm and 40 μm, a substantial increase from that of the AR coating thickness of 10 μm. It is important to note the presence of an Al peak at the surface of the coating, likely a result of outward diffusion of the coating dissolved Al reacting with the atmosphere and forming Al_2O_3 [35, 36]. The presence of Al_2O_3 has been reported to reduce Zn evaporation during forming processes [4, 105]. A strong Zn peak can be observed at the surface of the coating, owing to the ZnO that forms during annealing [35]. Afterwards, the Zn content decreased to a plateau for samples annealed for 60 s or less, a result of high concentrations of Γ-Fe_3Zn_{10} within the coating layer. The overall Zn concentration was found to steadily decrease with increasing depth, owing to a decreasing Zn content within α-Fe(Zn) as a result of diffusion [35, 37]. Previous literature has stated that a Zn based coating will be cathodically protective if the α-Fe(Zn) has a bulk composition of 30 wt% Zn [2, 8], and as a result this was set as the lower threshold value. Consultation of Figure 5.4 found that as annealing time increased, the bulk concentration of Zn within the coating decreased until it was less than 30 wt% after 240 s of annealing. Therefore, it is unlikely that a coating annealed for 240 s or longer will be capable of providing robust cathodic protection to the substrate, however, electrochemical testing was necessary in order to prove this hypothesis.

The XRD results (Figure 5.6) for a sample annealed at 700°C for 60 s indicated that the coating fully transforms into Γ-Fe_3Zn_{10} prior to passing through the peritectic temperature. When the coating is annealed at temperatures greater than 782°C, specifically at 900°C, it was found that all annealing times consisted of a mixture of α-Fe(Zn), Γ-Fe_3Zn_{10}, and minor fractions of ZnO. It was found that as annealing time at 900°C increased, the fraction of Γ-Fe_3Zn_{10} within the coating layer decreased while the amount of α-Fe(Zn) increased commensurately. The fraction of formed ZnO was also found to increase as annealing times increased. These results were found to be generally consistent with that seen from GDOES (Figure 5.4). Growth of the α-Fe(Zn) increased in a parabolic trend, indicative of a diffusion-based growth mechanism [36, 37]. The results indicate that when the samples were annealed for 180 s or less, the coating consisted of a mixture of Γ-Fe_3Zn_{10} and α-Fe(Zn); after annealing for 240 s, the fraction of Γ-Fe_3Zn_{10} was deemed to be negligible. As a result of the eventual disappearance of this phase, it can be assumed that all residual Zn(Fe) liquid at 900°C had transformed into α-Fe(Zn). The XRD spectra (Figure 5.5) showed that as annealing time increased, the major peak associated with α-Fe(Zn) shifted to higher values of 2θ. Based upon the knowledge that lighter elements diffract at higher angles while heavier elements diffract at smaller values, it can be inferred that the fraction of Fe within the phase is increasing. These results are consistent with the GDOES results (Figure 5.4) which indicated decreasing Zn contents as a function of increasing annealing times. Moreover, GDOES analysis revealed that the global Zn content within a coating annealed for 240 s or longer was less than 30 wt%; XRD has deemed these coatings to contain only α-Fe(Zn). The bulk coating analysis from XRD (Figure 5.7) indicated that, when the coating only contained α-Fe(Zn), the global Zn concentration was less than 30 wt%, consistent with the results seen from GDOES. It is, therefore, probable that a α-Fe(Zn)-only containing coating will not provide robust cathodic protection, and as a result the presence of Γ-Fe_3Zn_{10} in the coating is likely necessary. However, it must be remembered that Γ-Fe_3Zn_{10} forms as a result of the presence of Zn(Fe) liquid at the stamping temperature, and as a result any coating that consists of some fraction of Γ-Fe_3Zn_{10} would be susceptible to LME. These results were further tested using electrochemistry, which is discussed in §6.2.

The SEM results (Figure 5.9, Figure 5.10) were found to be consistent with the data obtained from GDOES (Figure 5.4) and XRD (Figure 5.6). The sample annealed at 700°C (Figure 5.9) was found to consist majorly of Γ-Fe_3Zn_{10} with no other Fe-Zn intermetallics detected, indicating that the coating fully transforms into Γ-Fe_3Zn_{10} before passing through the pertiectic temperature at 782°C. When annealing times at 900°C were 180 s or less (Figure 5.10), the coating comprised of a mixture of Γ-Fe_3Zn_{10} and α-Fe(Zn). It can be seen that the majority of Γ-Fe_3Zn_{10} present within the coating layer was segregated to the surface edge of the coating, as observed in previous literature [106]. These results are expected due to the fact that Γ-Fe_3Zn_{10} forms as a result of a solidifying liquid. Samples annealed between 190 s and 230 s indicated the presence of some retained Γ-Fe_3Zn_{10}. When annealing times were 240 s or longer, the coating consisted of α-Fe(Zn) with no discernible Γ-Fe_3Zn_{10}. Therefore, the minimum annealing time for all Zn(Fe) liquid to transform into α-Fe(Zn) at 900°C occurs at 240 s. A wavy, detached oxide layer consisting of ZnO and MnO was found at the surface of the coating, resultant of the poor adherence of these oxides to Fe-Zn intermetallics. This lack of cohesion has been attributed to the presence of a liquid phase at the annealing temperature, thereby decreasing the interfacial energy between the outer edge of the coating and the oxide layer [40]. The presence of MnO for longer annealing times is a result of the high affinity of Mn for oxygen, as well as outward lattice diffusion [40, 41].

SAM-AES, as seen in Figure 5.13 and Figure 5.14, was used to determine the surface chemistry of the coating that would initially come in contact with a corrosive environment. The images show that the majority of the surface of the coating was covered by Γ-Fe_3Zn_{10} after annealing for 30 s at 900°C (Figure 5.13), while the remainder was comprised of α-Fe(Zn). This was, again, expected as Γ-Fe_3Zn_{10} forms from a solidifying liquid. After 240 s of annealing (Figure 5.14), the surface was almost entirely composed of α-Fe(Zn) with some residual fractions of Γ-Fe_3Zn_{10}. These results were found to be consistent with both XRD (Figure 5.7) and SEM (Figure 5.11) results in regards to the fraction of Γ-Fe_3Zn_{10} present on the coating surface.

It was hypothesized that a single-phase coating containing only α-Fe(Zn) would not be cathodically protective as it does not contain at least 30 wt% Zn based upon the results currently seen from GDOES, XRD, SEM, and SAM-AES. Thus, there must exist some critical fraction of Γ-Fe_3Zn_{10} necessary within the coating to achieve robust cathodic protection. However, the given data does not clearly resolve the critical volume fraction of Γ-Fe_3Zn_{10}, and as such further testing was required, as detailed in §6.2.

6.2 The effect of the fraction of Γ-Fe_3Zn_{10} on the electrochemical properties

Electrochemical polarization techniques were conducted in an attempt to define the electrochemical properties of the coatings as a result of annealing time. Figure 5.16 shows the effect of annealing time at 900°C on the OCP values. As a result of the coating surface chemistry, as seen from SAM-AES (Figure 5.13**,** Figure 5.14), samples were found to group at specific potentials. It was found that as annealing time increased, the OCP value increased gradually within these groupings; these results were expected as the global Fe content within the coating layer was found to increase. However, the rapid increases in potential between these clusters was not expected as it was anticipated that there would only be minor changes to the Zn content from the GDOES (Figure 5.4), XRD (Figure 5.6), SEM (Figure 5.10), and SAM-AES (Figure 5.13**,** Figure 5.14) results. These results indicate that the surface in contact with the solution has more significant changes to the overall Zn content between clusters than within the groups. It is, then, likely that the fraction of Γ-Fe_3Zn_{10} within the coating affects the Zn content at the outer area of the coating. This further solidifies the hypothesis that a set fraction of Γ-Fe_3Zn_{10} is required to be present within the coating layer. As a result of the given data, it is possible that this critical fraction occurs when the sample is annealed for 210 s or less as this is the final annealing time to cluster at the most active potential.

Potentiodynamic polarization scans (Figure 5.18) found that all annealed samples clustered between the AR coated sample and the uncoated 22MnB5 substrate material. As expected, the E_{corr} associated with the AR coated sample was lower than that seen for all other samples, owing to the fact that the coating is comprised solely of η-Zn, an almost entirely pure Zn phase [33]. E_{corr} values associated with the Fe-Zn intermetallics were determined from the annealed coupons, and were found to be −0.861 V_{SCE} and −0.708 V_{SCE} for Γ-Fe_3Zn_{10} and α-Fe(Zn), respectively. In contrast, the uncoated substrate material was found to have an E_{corr} of −0.675 V_{SCE}. These values could then be used to determine the relative difference in E_{corr} between each phase and the substrate, giving insight into the driving force for cathodic protection in accordance to equation (6.1) [20]. *ΔG* corresponds to the free energy change or driving force, *n* is the exchanged electrons in the system, *F* is Faraday's constant, and *E* is the electrochemical potential of the cell at equilibrium.

$$\Delta G = -nFE \tag{6.1}$$

The determined difference in E_{corr} between Γ-Fe_3Zn_{10} and an uncoated 22MnB5 substrate was found to be $\Delta\mathrm{E}_{\Gamma-\mathrm{Fe_3Zn_{10}}-\alpha\mathrm{Fe}} = -0.186\ \mathrm{V}$, while the difference found between α-Fe(Zn) and the steel substrate was $\Delta\mathrm{E}_{\alpha-\mathrm{Fe(Zn)}-\alpha\mathrm{Fe}} = -0.033\ \mathrm{V}$. In accordance to equation (6.1), these results indicate that the largest driving force for cathodic protection is associated with the Γ-Fe_3Zn_{10} phase. In contrast, the relative difference in E_{corr} associated with a α-Fe(Zn)-only containing coating was minor, indicating a poor driving force for cathodic protection. Samples annealed within the transition window (Figure 5.19) were found to possess the same E_{corr} as determined for Γ-Fe_3Zn_{10} (Figure 5.18). Therefore, the minimum threshold value for Γ-Fe_3Zn_{10} within the coating layer remains unclear, and as a result further testing is required. Furthermore, a secondary active region with a potential nearly coincident to that of the E_{corr} for α-Fe(Zn) was observed for mixed phase coatings (approximately −0.71 V_{SCE}). These results indicate that the α-Fe(Zn) within these coatings provides very little to the offered cathodic protection, consistent with the minimal difference in E_{corr} between α-Fe(Zn) and the substrate material. This secondary anodic region was found to decrease in potential as annealing times increased, owing to the fact that the process is dominated by the dissolution of α-Fe(Zn). Moreover, all annealed samples were found to polarize quite rapidly, indicative of high activity rates and, subsequently, good cathodic protection to a substrate material. Figure 5.20 shows a sharp increase in the E_{corr} when the sample contained practically no Γ-Fe_3Zn_{10}, indicating that samples that comprise solely of α-Fe(Zn) provide a diminished driving force for cathodic protection.

A limiting current density within the cathodic region can be seen in Figure 5.18 and Figure 5.19 for samples that contained some fraction of Γ-Fe_3Zn_{10} within the coating layer, but was not observed for samples that consisted of only α-Fe(Zn). It has been reported that these limiting current densities are a consequence of oxygen reduction at the coating edge/corrosive solution interface [107]. Previous work by Yadav et al. also identified the presence of this limiting current density, but did not delve deeper into its mechanisms [67]. It is theorized that this limiting current density arises from the presence of Γ-Fe_3Zn_{10} within the coatings, which subsequently leads to the formation of stable Zn-based corrosion products.

Both simonkolleite and hydrozincite have been reported to have low solubility within acidic environments, and as a result may act as a barrier against the diffusion of oxygen [43, 95]. Previous literature has hypothesized that the barrier protection offered by simonkolleite arises as a result of its compact morphology, low electron density, and a reduction in the ion-transfer due to its layered structure [95]. Therefore, it is probable that these products preferentially form during the cathodic portion of the scan and act as cathodic inhibitors, greatly reducing the corrosion rate of the coating [43, 67, 68]. The lack of a limiting current density for longer annealing times is likely a result of the formation of akaganeite (β-FeOOH), which forms within chloride-containing environments when there is Fe enrichment within the coating [43, 93]. It has been reported that oxygen accepts electrons from akaganeite, and forms OH^- through reduction [78]. Therefore, mass transport of oxygen to the interface occurs as expected, and as a result oxygen reduction is not limited.

It is known that a limiting current density will result in a reduction in the corrosion rate; when this is not present, corrosion occurs as expected [108]. Thus, samples that exhibit a limiting current density and which preferentially form hydrozincite or simonkolleite on the surface as opposed to akaganeite will have slower rates of corrosion. These results further affirm the necessity of the presence of Γ-Fe_3Zn_{10} within the coating to be in contact with the corrosive environment to form these Zn-based corrosion products.

Currently, all electrochemical results have focused on the thermodynamic response of the coating as opposed to the reaction kinetics. For a more detailed understanding of how each phase will perform in a corrosive environment, the Evans diagram presented in Figure 6.1 must be analysed. This image details the galvanic coupling behaviour of the coating to the substrate material. It should be noted that only two samples are included within the figure; all annealing times were analysed with the same procedure. The corrosion potential for the galvanic couple (E_{gc}) was determined to be −0.855 V_{SCE} for coatings that contained some fraction of Γ-Fe_3Zn_{10}. In contrast, E_{gc} for coatings that consisted primarily of α-Fe(Zn) was found to be −0.69 V_{SCE}. These results are almost coincident with the E_{corr} found for each coating phase. As with previously, it can thus be stated that the driving force for cathodic protection is significantly higher when the coating contains at least some fraction of Γ-Fe_3Zn_{10} than coatings that contain only α-Fe(Zn). However, the most important information that can be inferred from this figure is the corrosion rate of the galvanic couple (i_{gc}), as seen in Figure 6.2. It was found that i_{gc} for coatings that contained even minute percentages of Γ-Fe_3Zn_{10} ranged between approximately 0.125 $\mu A/cm^2$ when the sample was annealed for 30 s and 1.05 $\mu A/cm^2$ when the sample was annealed for 300 s. In contrast, i_{gc} for single phase coatings (α-Fe(Zn)-only) was determined to be approximately 46 $\mu A/cm^2$ when the sample was annealed for 360 s and 60 $\mu A/cm^2$ when the sample was annealed for 420 s. Based upon these values, it can be seen that coatings that contain Γ-Fe_3Zn_{10} have a i_{gc} two orders of magnitude lower than coatings that contain only α-Fe(Zn). Therefore, it can be stated that Γ-Fe_3Zn_{10} will dissolve at a significantly slower rate when providing galvanic protection to the substrate material than α-Fe(Zn). It can justly be inferred that Γ-Fe$_3$Zn$_{10}$-containing coatings will provide longer cathodic protection than coatings that contain minor amounts or are completely devoid of Γ-Fe$_3$Zn$_{10}$.

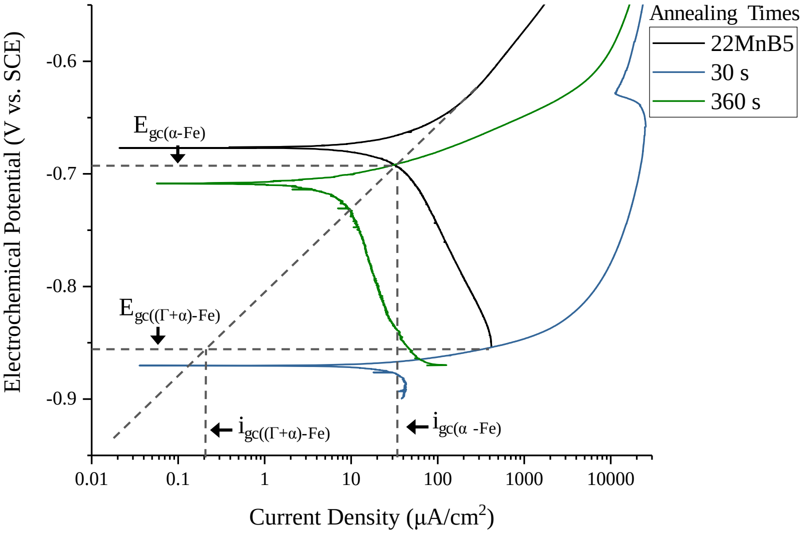

Figure 6.1: Galvanic coupling effects of the coating layer as a function of annealing time at 900°C.

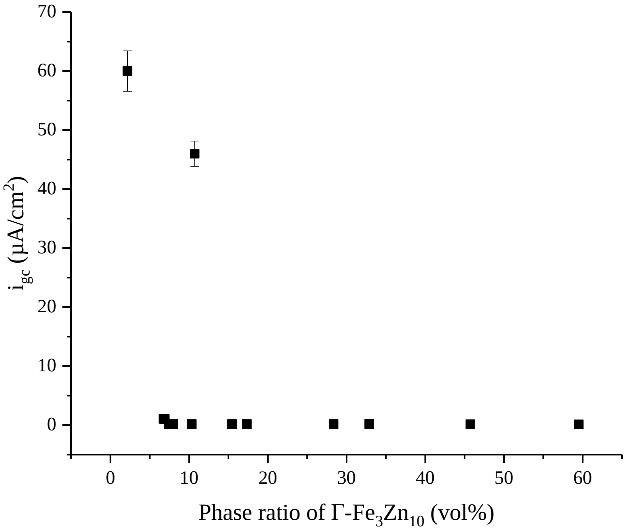

Figure 6.2: Effect of the fraction of Γ-Fe$_3$Zn$_{10}$ on the i_{gc} of the coatings.

Potentiostatic scans (Figure 5.24) were conducted to assess the results seen from Figure 6.1, or, more accurately, that the corrosion rate for Γ-Fe_3Zn_{10} was decreased in comparison to that of α-Fe(Zn). The given results indicated that when the coating contained some fraction of Γ-Fe_3Zn_{10}, annealed for 180 s or less (Figure 5.24 (a), (c), and (e)), the α-Fe(Zn) was found to be majorly intact regardless of applied potential, similar to what has been observed in previous literature [79]. Furthermore, some corrosion products were detected, likely acting as inhibitors to further corrosion attack [43, 67, 68]. In contrast, when the coating was devoid of Γ-Fe_3Zn_{10}, annealed for 240 s or longer (Figure 5.24 (b), (d), and (f)), significant coating damage was observed once the applied potential was within the anodic region determined for α-Fe(Zn). It was found that, when the sample had been annealed for a sufficiently long time, the coating layer was virtually nonexistent. In fact, some substrate attack was also witnessed when the sample was annealed for 420 s despite the fact that some α-Fe(Zn) still remained (Figure 5.24 (b)). This would indicate that when α-Fe(Zn) does not contain 30 wt% Zn (Figure 5.7**,** Figure 5.11), cathodic protection is extremely minor. These findings are consistent with the E_{corr} determined from the potentiodynamic polarization scans seen in Figure 5.18, whereby coatings that had been annealed for 180 s or less were found to be approximately 0.186 V_{SCE} more cathodic than the substrate material. Additionally, the corrosion rate of Γ-Fe_3Zn_{10} was found to be significantly slower than that of α-Fe(Zn), as determined from Figure 6.2, and as a result a coating that contains some critical volume fraction of Γ-Fe_3Zn_{10} can be expected to provide longer cathodic protection.

Galvanostatic polarization measurements (Figure 5.21) were found to be in good agreement with the conclusions drawn from the potentiodynamic polarization scans. As expected, the AR coated coupon was found to have a more active dissolution potential as opposed to the annealed samples, arising from the high Zn-content of the η-Zn coating layer. Owing to the increased Zn content within Γ-Fe_3Zn_{10} in comparison to α-Fe(Zn), the dissolution plateau associated with Γ-Fe_3Zn_{10} was found to be the second most active, occurring at approximately −0.812 V_{SCE}. This dissolution plateau was found to occur at a relatively constant value due to the fact that the composition within the phase does not change as a result of annealing time, consistent with the results found in previous literature [43, 79, 87]. It was found that as annealing time increased, and subsequently the fraction of Γ-Fe_3Zn_{10} within the coating decreased, that the dissolution plateau associated with Γ-Fe_3Zn_{10} decreased in duration until it was no longer present after annealing for 240 s at 900°C. As this phase was found to have the lowest corrosion rate from Figure 6.1, longer anodic dissolution times pertaining to Γ-Fe_3Zn_{10} will result in prolonged cathodic protection for the overall coating. These results have been found to be consistent with previous literature (Figure 2.16) [43]. From the galvanostatic data (Figure 5.21), the critical fraction of Γ-Fe_3Zn_{10} within the coating must occur somewhere between 180 s and 240 s of annealing. The galvanostatic polarization scans obtained for the transition window (Figure 5.22) were used to further determine the critical volume fraction of Γ-Fe_3Zn_{10} within the coating layer. As with all other annealing times, the anodic dissolution time indicative of Γ-Fe_3Zn_{10} gradually decreased with increasing annealing times until it was no longer present after 220 s of annealing at 900°C. The dissolution plateau of Γ-Fe_3Zn_{10} was found to last for approximately 1500 s when the sample was annealed for 210 s before full dissolution of the phase had occurred. However, in order to provide more robust cathodic protection, it can be inferred that the absolute minimum threshold value for Γ-Fe_3Zn_{10} occurs when the sample has been annealed at 900°C for 200 s, consistent with the findings from the OCP transients (Figure 5.16). Examination of the XRD results presented in Figure 5.6 reveals that this critical fraction is approximately 15 vol%.

Resultant of the increased Fe contents, the dissolution plateau for α-Fe(Zn) was found to be more noble in comparison to both the AR coated sample and mixed-phase coatings. It was found that the initial anodic dissolution plateaus occurred at approximately −0.686 V_{SCE}, and increased in nobility as dissolution time increased. This was a result of the compositional gradient that exists within α-Fe(Zn) due to the diffusional based growth mechanism by which it forms, whereby Zn content is highest towards the surface edge of the coating and gradually depletes as the coating/substrate interface is approached. This gradient was found to be the highest for the sample annealed at 700°C for 60 s, and gradually grew less pronounced when the sample was annealed at 900°C until it was virtually nonexistent after annealing for 360 s. These findings imply that the formed α-Fe(Zn) at both annealing temperatures is not completely saturated in Zn, contrary to what has been previously stated in literature [2, 43]. Final anodic dissolution plateaus indicative of α-Fe(Zn) were found to be approximately −0.633 V_{SCE}; a 53 mV increase from the initial value. Similar to the results seen from the potentiodynamic polarization scans, the final anodic dissolution plateau value associated with α-Fe(Zn) was found to be in close proximity to that of the substrate material, determined to be approximately −0.54 V_{SCE} from Figure 5.21. Based upon these results, the potential differences between each phase and the substrate material could be calculated to assess the driving force for cathodic protection. These values were found to be $\Delta E_{\Gamma-Fe_3Zn_{10}-\alpha Fe} = -0.272$ V and $\Delta E_{\alpha-Fe(Zn)-\alpha Fe} = -0.146$ V for coatings that contained significant fractions of Γ-Fe_3Zn_{10} and α-Fe(Zn), respectively. As concluded previously, coatings that contain at least 15 vol% Γ-Fe_3Zn_{10} will provide a larger driving force for cathodic protection than coatings that do not meet this minimum threshold value. Furthermore, when the minimum volume fraction of 15 vol% Γ-Fe_3Zn_{10} is obtained, a compositional gradient exists within the formed α-Fe(Zn).

The quantitative XRD analysis derived from the interrupted galvanostatic scans (Figure 5.25) was in good agreement with previous results indicating that longer annealing times result in a decreased resistance to corrosion. It was found that as annealing times increased, the relative phase fraction of corrosion products on the surface rose. The largest increase was found to occur when the sample had been annealed for 240 s or longer, with the inflection point occurring at approximately 210 s. Three predominant corrosion products were found to form preferentially due to the varying fractions of Γ-Fe_3Zn_{10} within the coating: hydrozincite, simonkolleite, and akaganeite. These results were found to be consistent with the results presented in this report and previous literature [43, 69]. As expected, it was found that akaganeite became the main corrosion product as annealing times increased due to the enrichment of Fe within the coating layer [43, 93]. Relative fractions of hydrozincite were found to remain approximately constant regardless of the phase ratio of Γ-Fe_3Zn_{10} within the coating layer, while simonkolleite was found to gradually decrease with increasing annealing time (Figure 5.26). This is, again, a result of decreasing Zn contents within the coating layer leading to decreased Zn-based corrosion products. As annealing time increased and the major corrosion product that was found on the surface switched from hydrozincite to akaganeite, the fraction of corrosion products rose substantially, indicating the necessity of Zn-based corrosion products to decrease the rate of corrosion. This is likely due to the enhanced stability of Zn-based corrosion products, as well as their ability to act as a barrier against oxygen diffusion [43].

Further interrupted galvanostatic polarization measurements (Figure 5.27) provided insight into how the coating layer dissolved in response to the electrolyte. Due to the more electronegative behaviour of Γ-Fe_3Zn_{10}, it was found to preferentially dissolve in the beginning stages of corrosion attack (Figure 5.27 (a)), consistent with previous results reported by Autengruber et. al [43] and Mutgi [79]. It was only once the phase had fully dissolved that dissolution of α-Fe(Zn) began to occur (Figure 5.27 (b)). It can be seen that localized areas of α-Fe(Zn) dissolved at a faster rate than other grains, likely a result of the compositional gradient within the phase determined by GDOES (Figure 5.4) and XRD (Figure 5.5). As expected, no substrate attack was observed throughout the test; the coating layer should continue to sacrificially corrode until it is no longer present (Figure 5.27 (c)). These results have also been reported in previous literature [43, 79].

SAM-AES analysis (Figure 5.28, Figure 5.29) was, as expected, in good agreement with the XRD results obtained for samples that underwent interrupted galvanostatic polarization scans. Cross-sectional analysis (Figure 5.28) of samples annealed for 180 s or less also indicated higher Zn and O enrichment at the surface of the coating along with C and Cl, indicative of hydrozincite and simonkolleite, respectively. As the contrast within this layer changes minimally, it is probable that this layer contains little porosity and, as a result, would serve as a barrier to the mass transport of oxygen, thereby limiting the current density [67, 109]. This layer was no longer present once annealing times were 240 s or longer (Figure 5.29); instead, gaps within the O map were seen. This would indicate not only increased porosity of akaganeite, but also that the electrons are being consistently supplied from akageneite to reduce oxygen to OH^- [78]. This is consistent with the XRD results (Figure 5.25), which indicated that as annealing times increased and the Fe content of the coating layer increased, the dominant corrosion products would change from simonkolleite and hydrozincite to akaganeite.

The TEM results (Figure 5.30) were able to better spatially resolve the formed corrosion products on a sample annealed for 60 s at 900°C that was subjected to interrupted galvanostatic polarization testing. Two main corrosion products were observed: one which was more globular in structure, and another that was found to be rod-like. The nanostructures and EELS spectra (Figure 5.31) of these corrosion products have been found to coincide with that seen in literature for hydrozincite and akaganeite, respectively [96-99]. From the EELS maps (Figure 5.30), it can be seen that the majority of corrosion products within the nanostructure coincide with hydrozincite, consistent with that previously seen from XRD (Figure 5.25) and SAM-AES (Figure 5.28, Figure 5.29). Thus, it is again likely that hydrozincite and simonkolleite act as oxygen barriers and decrease the overall rate of corrosion of the coating layer [43].

Galvanic corrosion tests (Figure 5.32) were able to determine the cathodic protection efficacy as a function of the amount of Γ-Fe_3Zn_{10} within the coating layer. All annealing times portrayed positive current densities, indicative of the fact that the substrate was noble to all coatings [110]. Therefore, all annealing times can be concluded to provide some form of sacrificial protection to the substrate. It was found that as annealing time increased, and subsequently the fraction of Γ-Fe_3Zn_{10} decreased, that the coupling current density increased. These results are consistent with the fact that Γ-Fe_3Zn_{10} provides a larger driving force for cathodic protection than α-Fe(Zn) such that average coupling currents (Figure 5.33) were lower for samples that contained fractions of at least 15 vol% Γ-Fe_3Zn_{10}. It was also found that the average galvanic current density for the sample annealed for 180 s increased partway through the scan. This is thought to be a result of preferential dissolution of Γ-Fe_3Zn_{10} whereby it is fully consumed after approximately 48 000 s due to the fact that the second average current density coincided with that found for samples that contained only α-Fe(Zn). Moreover, the fluctuations within the scans were found to increase as annealing times increased, indicative of increased corrosion rates [100]. These fluctuations have been attributed to the initiation of corrosion followed by repassivation [101, 111]. These results are consistent with that seen previously in Figure 6.1, whereby i_{gc} for

Γ-Fe_3Zn_{10} was found to be two orders of magnitude lower than that found for α-Fe(Zn). These results are, again, consistent with the previous findings (Figure 5.22) that some fraction of Γ-Fe_3Zn_{10} is necessary within the coating to provide robust cathodic protection.

Previous literature has often stated that cathodic protection can be achieved when the α-Fe(Zn) within the coating contains at least 30 wt% [2, 8]. The present results, however, indicate this to be unlikely due to a number of reasons. First and foremost, XRD and SEM analysis found that the α-Fe(Zn) produced within this study typically had a maximum solubility of Zn of 25-28 wt%; these results are consistent with findings that α-Fe(Zn) contains 20-26 wt% Zn at 900°C [4]. GDOES (Figure 5.4) results and bulk XRD/SEM (Figure 5.7**,** Figure 5.11) analyses found that this minimum Zn content threshold was not met when the sample was annealed at 900°C for 240 s or longer. In addition, the anodic dissolution potential indicative of α-Fe(Zn) was found to rise as dissolution time increased. These results have been attributed to the concentration gradient of Zn within the phase, such that total Zn decreases as the coating/substrate interface is approached, resultant of the diffusional based growth mechanism of α-Fe(Zn). Corrosion product formation was found to rapidly increase when the sample was annealed for 240 s or more, representative of a diminished ability to provide robust cathodic protection. Furthermore, a limiting current density was observed when samples contained some fraction of Γ-Fe_3Zn_{10}; this phenomenon was not present when coatings were comprised primarily of α-Fe(Zn). This was found to be a result of Zn-based corrosion products acting as a barrier to oxygen diffusion, further decreasing the corrosion rate of mixed phase coatings.

These given results are consistent with how the Zn content within the coating layer affects the electrochemical potential, as seen in Figure 6.3. It can be seen that when the coating contains less than 15 vol% Γ-Fe_3Zn_{10}, the driving force for cathodic protection is severely diminished. It can thus be concluded that this critical volume fraction of Γ-Fe_3Zn_{10} is required within the coating to provide robust cathodic protection. This percentage has been found to occur when the sample is annealed for 200 s at 900°C.

As a caveat, the presence of Γ-Fe_3Zn_{10} within the coating layer at room temperature is indicative of the presence of Zn(Fe) liquid at the austenitization temperature. More specifically, this presence of liquid phase at the stamping temperature has been found to result in LME during DHPF processes [36, 37, 59]. As a result, the necessity of avoiding or mitigating LME during DHPF with the use of Zn-based coatings is fundamentally in conflict with the requirement of obtaining robust cathodic protection, which has been found to require approximately 15 vol% Γ-Fe_3Zn_{10} and subsequently Zn(Fe) liquid at forming temperatures. Therefore, the processing window to achieve robust cathodic protection with Zn-based DHPF coatings is extremely narrow when the conventional 22MnB5 substrate is used.

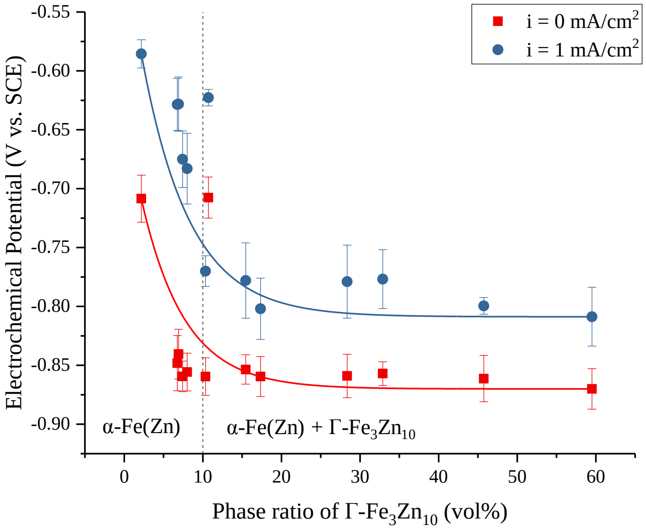

Figure 6.3: Effect of the fraction of Γ-Fe$_3$Zn$_{10}$ on the E$_{corr}$ (i = 0 mA/cm^2) and initial dissolution potential arrest (i = +1 mA/cm^2).

7 CONCLUSIONS AND RECOMMENDATIONS FOR FUTURE WORK

7.1 Conclusions

The microstructural evolution of the coatings at 900°C and its effect on the electrochemical properties of continuously galvanized DHPF coatings on conventional 22MnB5 substrates was explored in the attempt to determine a processing route that could achieve robust cathodic protection while avoiding LME. The key findings of the present research are summarized as follows:

- UTS was found to be independent of annealing time for the uncoated substrate material and always met the industrial target mechanical properties of $\sigma_{UTS} \geq 1500$ MPa. In contrast, UTS was found to decrease as a result of increasing annealing time for the GI70 coated samples such that the target mechanical properties were not met when the sample was annealed for 180 s or longer at 900°C. This is likely a result of microcracking within α-Fe(Zn) and a reduction in the cross-sectional area of the substrate.
- The bulk Zn content within the annealed coating layers was found to decrease with increasing annealing times until it was less than 30 wt% Zn after annealing for 240 s at 900°C.
- The volume fraction of α-Fe(Zn) within the coatings at room temperature increased with increasing annealing time at 900°C, while the overall fraction of Γ-Fe_3Zn_{10} decreased until it was depleted after 240 s of annealing time. These trends were found to be parabolic in nature, consistent with diffusion-based growth.
- Potentiodynamic polarization scans determined that the differences in E_{corr} between the mixed phase Γ-Fe_3Zn_{10} + α-Fe(Zn) coatings, the α-Fe(Zn) and the uncoated 22MnB5 substrate were $\Delta E_{\Gamma-Fe_3Zn_{10}-\alpha Fe} = -0.186\text{ V}$ and $\Delta E_{\alpha-Fe(Zn)-\alpha Fe} = -0.033\text{ V}$, respectively. These results indicate a significantly larger driving force for cathodic protection from coatings that contain a significant fraction of Γ-Fe_3Zn_{10} as opposed to coatings that consist almost entirely of α-Fe(Zn).

- The predicted corrosion current density determined for the Γ-Fe_3Zn_{10} + α-Fe(Zn) coatings was two orders of magnitude lower than that found for α-Fe(Zn)-only coatings, indicating that coatings that contain some fraction of Γ-Fe_3Zn_{10} will corrode at a significantly slower rate.
- Coatings annealed for 220 s or longer were found to have a significant increase in the fraction of formed corrosion products in comparison to coatings that were annealed for 210 s or less. The dominant corrosion product was found to switch from hydrozincite for samples with fractions of greater than 10 vol% Γ-Fe_3Zn_{10} to akaganeite when the coating contained fractions of greater than 85 vol% α-Fe(Zn). Zn-based corrosion products have often been found to be insoluble, thereby providing a more effective oxygen barrier. This secondary barrier film further reduces the corrosion rate. It is, therefore, necessary to have some critical fraction of Γ-Fe_3Zn_{10} to achieve robust cathodic protection.
- It was found that the critical volume fraction of Γ-Fe_3Zn_{10} necessary within the annealed coating to provide robust cathodic protection to the 22MnB5 substrate is approximately 15 vol%. Thus, robust cathodic protection can be linked to a processing window of annealing at 900°C for 200 s or less.
- Globally, the above findings lead to the conclusion that it is necessary for there to be some Zn(Fe) liquid present at the 900°C 22MnB5 DHPF temperature for the solidified coating to contain at least 15 vol% Γ-Fe_3Zn_{10} such that the coating will provide robust cathodic protection. This requirement is fundamentally in conflict

with the need to avoid the presence of a liquid during forming to mitigate LME. As a result, the processing window to achieve robust cathodic protection for continuously galvanized coatings on DHPF 22MnB5 is extremely narrow and unlikely to be practical in an industrial environment.

7.2 Future Work

Based upon the conclusions drawn from the present work, some future work can be recommended.

- Presently, the reason for microcracking of α-Fe(Zn) is not well established. It is recommended that EBSD, TEM, and APT be performed along prior austenitic grain boundaries to assess if it is a result of liquid Zn accumulation that weakens the cohesion between grains.
- Outdoor exposure tests should be conducted to determine how well the coating performs under environmental conditions and to confirm the critical volume fraction of Γ-Fe_3Zn_{10}.
- A new substrate material must be designed such that forming may be performed below the peritectic temperature of 782°C while still achieving a fully martensitic microstructure. This change will ensure that the coating will be fully solidified prior to hot stamping, and as such a robust, cathodically protective Γ-Fe_3Zn_{10} + α-Fe(Zn) coating may be obtained while avoiding the presence of liquid during stamping and avoiding LME.

- DHPF tests in both a planar and U-shaped die must be performed to assess coating adhesion and microstructural development. These tests will ensure that microcracking and LME have been drastically reduced as a result of the new steel grade. Furthermore, electrochemical testing should be performed on the deformed samples to assess corrosion protection after forming.
- Hydrogen embrittlement is a well-known contributor to the premature failure of martensitic steels. Therefore, hydrogen desorption experiments should be performed on both the substrate material and GI70 coated substrates prior to and subsequent to deformation to determine the susceptibility to reversible and irreversible hydrogen traps.
- Cyclic salt spray testing must be performed on the new steel grade after it has been coated and experimentally hardened. Salt spray testing should be performed on non-scribed and scribed samples, as well as samples that have had half of their coating removed to assess the cathodic protection efficacy of the coating.

8 REFERENCES

[1] Karbasian, H., & Tekkaya, A.E. (2010). A review on hot stamping. Journal of Materials Processing Technology, 210(15), 2103.

[2] Fan, D.W., & De Cooman, B.C. (2012). State-of-the-Knowledge on Coating Systems for Hot Stamped Parts. Steel Research International, 83(5), 412.

[3] "22MnB5 Boron alloyed quenched and tempered steel," Salzgitter Flachstahl GmbH, Salzgitter, Germany, 2008, available from: https://www.salzgitterflachstahl.de/fileadmin/mediadb/szfg/informationsmaterial/produktinformationen/warmgewalzte_produkte/eng/22mnb5.pdf

[4] Dosdat, L., Petitjean, J., Vietoris, T., & Clauzeau, O. (2011). Corrosion Resistance of Different Metallic Coatings on Press-Hardened Steels for Automotive. Steel Research International, 82(6), 726.

[5] Grigorieva, R., Drillet, P., Mataigne, J.M., & Barges, P., Galvatech 2011 Conference Proceedings: Zinc Coated Steel Sheets for Press Hardening Applications, June 21-24, 2011, Genoa, Italy.

[6] Fan, D.W., Kim, H.S., Oh, J.K., & Chin, K.G. (2010). Coating degradation in hot press forming. ISIJ International, 50(4), 561.

[7] Gui, Z.X., Wang, K., Zhang, Y.S., & Zhu, B. (2014). Cracking and interfacial debonding of the Al–Si coating in hot stamping of pre-coated boron steel. Applied Surface Science, 316, 595.

[8] Faderl, J., Kolnberger, S., Rosner, M., & Kurz, T., Galvatech 2011 Conference Proceedings: Zinc Coated Steel Sheets for Press Hardening Applications, June 21-24, 2011, Genoa, Italy.

[9] Drillet, P., Grigorieva, R., & Leuillier, G., Galvatech 2011 Conference Proceedings: Zinc Coated Steel Sheets for Press Hardening Applications, June 21-24, 2011, Genoa, Italy.

[10] Patent WO 2012/028224 Al: “Method for Hot-Forming a Coated Metal Part and Formed Part”.

[11] Krieg, R., Vimalanandan, A., & Rohwerder, M. (2014). Corrosion of zinc and Zn-Mg alloys with varying microstructures and magnesium contents. Journal of The Electrochemical Society, 161(3), C156.

[12] Patent WO 2011/023418 A1: “Method for Producing a Steel Component Provided with a Metal Coating Protecting Against Corrosion and Steel Component”.

[13] Kondratiuk, J., Kuhn, P., Köyer, M., Meurer, M., & Horstmann, J., Galvatech 2011 Conference Proceedings: Zinc Coated Steel Sheets for Press Hardening Applications, June 21-24, 2011, Genoa, Italy.

[14] Belanger, P., Hall, J.N., Coryell, J.J., & Singh, J.P.: International Symposium on New Developments in Advanced High-Strength Sheet Steels, June 23-27, 2013, Vail, Colorado, USA.

[15] Akioka, K., Nishibata, T., Imai, K., Takayama, T., & Nakata, M., Galvatech 2011 Conference Proceedings: Zinc Coated Steel Sheets for Press Hardening Applications, June 21-24, 2011, Genoa, Italy.

[16] Li, J., Yang, H., Zhang, S., Liu, X., & Ha, W., Galvatech 2013 Conference Proceedings: Automotive Applications, September 23-27, 2013, Beijing, China.

[17] Horvath, C.D, Enloe, C.M., Singh, J.P., & Coryell, J.J: International Symposium on New Developments in Advanced High-Strength Sheet Steels, May 30-June 2, 2017, Keystone, Colorado, USA.

[18] Swartzell, T.A.: Great Designs in Steel Conference, May 11, 2016, Livonia, Michigan, USA.

[19] Taylor, K.A., & Hansen, S.S. (1990). The Boron hardenability effect in thermomechanically processed, direct-quenched 0.2 Pct C steels. Metallurgical Transactions A, 21(6), 1697.

[20] Jones, D.A. (1992). Principles and Prevention of Corrosion. Macmillan.

[21] Marder, A.R. (2000). The metallurgy of zinc-coated steel. Progress in Materials Science, 45(3), 191.

[22] Silva, E.A., “Private Communication,” 2005.

[23] Baril, E., & L'Espérance, G. (1999). Studies of the morphology of the Al-rich interfacial layer formed during the hot dip galvanizing of steel sheet. Metallurgical and Materials Transactions A, 30(13), 681.

[24] McDermid, J.R., Kaye, M.H., & Thompson, W.T. (2007). Fe solubility in the Zn-rich corner of the Zn-Al-Fe system for use in continuous galvanizing and galvannealing. Metallurgical and Materials Transactions B, 38(2), 215.

[25] Mandal, G.K., Balasubramaniam, R., & Mehrotra, S.P. (2009). Theoretical investigation of the interfacial reactions during hot-dip galvanizing of steel. Metallurgical and Materials Transactions A, 40(3), 637.

[26] Kolleck, R., Veit, R., Merklein, M., Lechler, J., & Geiger, M. (2009). Investigation on induction heating for hot stamping of boron alloyed steels. CIRP Annals, 58(1), 275.

[27] Paar, U., Becker, H.H., Alsmann, M., CHS^2 2008 Conference Proceedings: Hot Sheet Metal Forming of High-Performance Steel, October 22-24, 2008, Kassel, Germany.

[28] Shibli, S.M.A., Meena, B.N., & Remya, R. (2015). A review on recent approaches in the field of hot dip zinc galvanizing process. Surface and Coatings Technology, 262, 210.

[29] Suehiro, M., Maki, J., Kusumi, K., Ohgami, M., & Miyakoshi, T. (2003). Properties of aluminized steels for hot-forming (No. 2003-01-2853). SAE Technical Paper.

[30] Grauer, S.J., Caron, E.J.F.R., Chester, N.L., Wells, M.A., & Daun, K.J. (2015). Investigation of melting in the Al–Si coating of a boron steel sheet by differential scanning calorimetry. Journal of Materials Processing Technology, 216, 89.

[31] Maki, J., Kurosaki, M., Kusumi, K, & Abe, M., CHS^2 2011 Conference Proceedings: Hot Sheet Metal Forming of High-Performance Steel, June 13-17, 2011, Kassel, Germany.

[32] Xiong, W., Kong, Y., Du, Y., Liu, Z.K., Sellby, M., & Sun, W.H. (2009). CALPHAD 33, 433.

[33] Pokorny, P., Kolisko, J., Balik, L., & Novak, P. (2015). Description of structure of Fe-Zn intermetalic compounds present in hot-dip galvanized coatings on steel. Metalurgija, 54(4), 707.

[34] Reumont, G., Vogt, J.B., Iost, A., & Foct, J. (2001). The effects of an Fe–Zn intermetallic-containing coating on the stress corrosion cracking behavior of a hot-dip galvanized steel. Surface and Coatings Technology, 139(2), 265.

[35] Autengruber, R., Luckeneder, G., Kolnberger, S., Faderl, J., & Hassel, A.W. (2012). Surface and Coating Analysis of Press-Hardened Hot-Dip Galvanized Steel Sheet. Steel Research International, 83(11), 1005.

[36] De Cooman, B.C., Jung, W., Jo, K.R., Sulistiyo, D.H, Cho, L., Galvatech 2017 Conference Proceedings: Zinc Coated Steel Sheets for Press Hardening Applications, November 12-16, 2017, Tokyo, Japan.

[37] Janik, V., Lan, Y., Beentjes, P., Norman, D., Hensen, G., & Sridhar, S. (2016). Zn diffusion and α-Fe(Zn) layer growth during annealing of Zn-coated B steel. Metallurgical and Materials Transactions A, 47(1), 400.

[38] Wilkinson, D.S. (2000). Mass Transport in Solids and Fluids. Cambridge University Press.

[39] Lee, C.W., Fan, D.W., Lee, S.J., & De Cooman, B.C., Galvatech 2011 Conference Proceedings: Challenges in Galvanizing Advanced High Strength Steels, June 21-24, 2011, Genova, Italy.

[40] Hayashi, S., Sekimoto, T., Honda, K., Kinoshita, T., Tanaka, K., Ushioda, K., & Ukai, S. (2009). The effect of S and Mn on the high-temperature oxidation and scale spallation behavior of low-carbon steels. ISIJ International, 49(12), 1938.

[41] Mrowec, S. (1967). On the mechanism of high temperature oxidation of metals and alloys. Corrosion Science, 7(9), 563.

[42] Hassel, A.W., Galvatech 2017 Conference Proceedings: Zinc Coated Steel Sheets for Press Hardening Applications, November 12-16, 2017, Tokyo, Japan.

[43] Autengruber, R., Luckeneder, G., & Hassel, A.W. (2012). Corrosion of press-hardened galvanized steel. Corrosion Science, 63, 12-19.

[44] Lazik, S., Esling, C., & Wegria, J. (1995). Cracking in Zinc Layers on Continuous Galvanized Sheets: A Review. Texture, Stress, and Microstructure, 23(3), 131-147.

[45] Cho, L., Kang, H., Lee, C., & De Cooman, B.C. (2014). Microstructure of liquid metal embrittlement cracks on Zn-coated 22MnB5 press-hardened steel. Scripta Materialia, 90, 25.

[46] Kang, H., Cho, L., Lee, C., & De Cooman, B.C. (2016). Zn penetration in liquid metal embrittled TWIP steel. Metallurgical and Materials Transactions A, 47(6), 2885.

[47] Rostoker, W., McCaughey, J.M., & Markus, H. (1960). Embrittlement by Liquid Metals, Reinhold Publ. Corp., New York.

[48] Rehbinder, P.A., & Shchukin, E.D. (1972). Surface phenomena in solids during deformation and fracture processes. Progress in Surface Science, 3, 97.

[49] Stoloff, N.S. & Johnston, T.L. (1963). Crack Propagation in a Liquid Metal Environment. Acta Metallurgica, 11, 251.

[50] Westwood, A.R.C., & Kamdar, M.H. (1963). Concerning liquid metal embrittlement, particularly of zinc monocrystals by mercury. Philosophical Magazine, 8(89), 787.

[51] Robertson, W.M. (1966). Propagation of a Crack Filled with Liquid Metal. North American Aviation Science Center, Thousand Oaks, Calif.

[52] Lynch, S.P. (1994). Failures of structures and components by environmentally assisted cracking. Engineering Failure Analysis, 1(2), 77.

[53] Popovich, V.V. (1979). Mechanisms of liquid-metal embrittlement. Fiziko-khimicheskaya Mekhanika Materialov, 15(5), 11.

[54] Hancock, P.C., & Ives, M.B. (1971). The role of plastic deformation in liquid metal embrittlement. Canadian Metallurgical Quarterly, 10(3), 207.

[55] Krishtal, M.A. (1970). The Formation of Dislocations in Metals on Diffusion of Surface-Active Substances in Connection with the Effect of Adsorption Embrittlement. In Soviet Physics Doklady (Vol. 15, p. 614).

[56] Gordon, P., & An, H.H. (1982). The mechanisms of crack initiation and crack propagation in metal-induced embrittlement of metals. Metallurgical Transactions A, 13(3), 457.

[57] Klinger, L., & Rabkin, E. (2010). Strains and stresses caused by penetrative wetting of grain boundaries by the liquid phase. Scripta Materialia, 62(12), 918.

[58] Beal, C., Kleber, X., Fabregue, D., & Bouzekri, M. (2012). Embrittlement of a zinc coated high manganese TWIP steel. Materials Science and Engineering: A, 543, 76.

[59] Lee, C.W., Fan, D.W., Sohn, I.R., Lee, S.J., & De Cooman, B.C. (2012). Liquid-metal-induced embrittlement of Zn-coated hot stamping steel. Metallurgical and Materials Transactions A, 43(13), 5122.

[60] Lee, C.W., Choi, W.S., Cho, L., Cho, Y.R., & De Cooman, B.C. (2015). Liquid-Metal-Induced Embrittlement Related Microcrack Propagation on Zn-coated Press Hardening Steel. ISIJ International, 55(1), 264.

[61] Kojima, N. et al., CHS^2 2011 Conference Proceedings: Hot Sheet Metal Forming of High-Performance Steel, June 13-17, 2011, Kassel, Germany.

[62] Faderl, J., CHS^2 2009 Conference Proceedings: Hot Sheet Metal Forming of High-Performance Steel, June 15-17, 2009, Luleå, Sweden.

[63] Akioka, K. et al., Galvatech 2011 Conference Proceedings: Challenges in Galvanizing Advanced High Strength Steels, June 21-24, 2011, Genova, Italy.

[64] Genderen, M.J.V, Verloop, W.C., Loiseaux, J., & Hensen, G.C., CHS^2 2011 Conference Proceedings: Hot Sheet Metal Forming of High-Performance Steel, June 13-17, 2011, Kassel, Germany.

[65] Smith, J.F., ASM Handbook, ASM International, Materials Park, Ohio 1999, 2.206.

[66] Lee, H.H., & Hiam, D. (1989). Corrosion resistance of galvannealed steel. Corrosion, 45(10), 852.

[67] Yadav, A.P., Katayama, H., Noda, K., Masuda, H., Nishikata, A., & Tsuru, T. (2007). Effect of Fe–Zn alloy layer on the corrosion resistance of galvanized steel in chloride containing environments. Corrosion Science, 49(9), 3716.

[68] Thébault, F., Vuillemin, B., Oltra, R., Ogle, K., & Allely, C. (2008). Investigation of self-healing mechanism on galvanized steels cut edges by coupling SVET and numerical modeling. Electrochimica Acta, 53(16), 5226.

[69] Zhu, F., Persson, D., Thierry, D., & Taxen, C. (2000). Formation of corrosion products on open and confined zinc surfaces exposed to periodic wet/dry conditions. Corrosion, 56(12), 1256.

[70] Krieg, R., Vimalanandan, A., & Rohwerder, M. (2014). Corrosion of zinc and Zn-Mg alloys with varying microstructures and magnesium contents. Journal of The Electrochemical Society, 161(3), C156.

[71] dos Santos, A.P., Manhabosco, S.M., Rodrigues, J.S., & Dick, L.F.P. (2015). Comparative study of the corrosion behavior of galvanized, galvannealed and Zn55Al coated interstitial free steels. Surface and Coatings Technology, 279, 150.

[72] Dafydd, H., Worsley, D.A., & McMurray, H.N. (2005). The kinetics and mechanism of cathodic oxygen reduction on zinc and zinc–aluminium alloy galvanized coatings. Corrosion Science, 47(12), 3006.

[73] Ogle, K., Morel, S., & Jacquet, D. (2006). Observation of self-healing functions on the cut edge of galvanized steel using SVET and pH microscopy. Journal of the Electrochemical Society, 153(1), B1.

[74] Ligier, V., Wéry, M., Hihn, J. Y., Faucheu, J., & Tachez, M. (1999). Formation of the main atmospheric zinc end products: $NaZn_4Cl(OH)_6SO_4 \cdot 6H_2O$, $Zn_4SO_4(OH)_6 \cdot nH_2O$ and $Zn_4Cl_2(OH)_4SO_4 \cdot 5H_2O$ in $[Cl^-][SO_4^{2-}][HCO_3^-][H_2O_2]$ electrolytes. Corrosion Science, 41(6), 1139.

[75] LeBozec, N., Thierry, D., Rohwerder, M., Persson, D., Luckeneder, G., & Luxem, L. (2013). Effect of carbon dioxide on the atmospheric corrosion of Zn–Mg–Al coated steel. Corrosion Science, 74, 379.

[76] Qu, Q., Yan, C., Wan, Y., & Cao, C. (2002). Effects of NaCl and SO_2 on the initial atmospheric corrosion of zinc. Corrosion Science, 44(12), 2789.

[77] LeBozec, N., Thierry, D., Peltola, A., Luxem, L., Luckeneder, G., Marchiaro, G., & Rohwerder, M. (2013). Corrosion performance of Zn–Mg–Al coated steel in accelerated corrosion tests used in the automotive industry and field exposures. Materials and Corrosion, 64(11), 969.

[78] Xiao, H., Ye, W., Song, X., Ma, Y., & Li, Y. (2017). Evolution of Akaganeite in Rust Layers Formed on Steel Submitted to Wet/Dry Cyclic Tests. Materials, 10(11), 1262.

[79] Mutgi, A.V. (2015). Effect of Chemical Composition and Microstructure of Zn and Al-based Coatings on Electrochemical Response in Corrosive Environments. Masters Thesis, Delft University of Technology.

[80] "22MnB5 Boron alloyed quenched and tempered steel," Salzgitter Flachstahl GmbH, Salzgitter, Germany, 2008, available from: https://www.salzgitter-flachstahl.de/fileadmin/mediadb/szfg/informationsmaterial/produktinformationen/warmgewalzte_produkte/eng/22mnb5.pdf

[81] "ASTM A90/A90M-13, Standard Test Method for Weight [Mass] of Coating on Iron and Steel Articles with Zinc or Zinc-Alloy Coatings," ASTM International, West Conshohocken, PA, 2013.

[82] "ASTM E8/E8M-16a: Standard Test Methods for Tension Testing of Metallic Materials," ASTM International, West Conshohocken, PA, 2016.

[83] Davis, J. R., Tensile testing, 2nd Edition, ASM International, 2004.

[84] Available from: http://www.eels.info/atlas/.

[85] "ASTM G5-14, Standard Reference Test Method for Making Potentiodynamic Anodic Polarization Measurements," ASTM International, West Conshohocken, PA, 2014.

[86] Zhong, W., Galvatech 2001 Conference Proceedings: Zinc Coated Steel Sheets for Press Hardening Applications, June 26-28, 2011, Brussels, Belgium.

[87] Schachinger, E.D., Kolnberger, S., & Faderl, J., CHS^2 Conference Proceedings: Hot Sheet Metal Forming of High-Performance Steel, June 4-7, 2017, Atlanta, GA., USA.

[88] Kurz, T., Luckeneder, G., Manzenreiter, T., Schwinghammer, H., & Sommer, A. (2015). Zinc Coated Press-Hardening Steel-Challenges and Solutions (No. 2015-01-0565). SAE Technical Paper.

[89] Belanger, P., Lopez Lage, M., Romero Ruiz, L., & Isaksson, K., CHS^2 Conference Proceedings: Hot Sheet Metal Forming of High-Performance Steel, June 4-7, 2017, Atlanta, GA., USA.

[90] Pavlina, E.J., Van Tyne, C.J. (2008) Correlation of Yield Strength and Tensile Strength with Hardness for Steels. ASM International, 17, 888.

[91] Krauss, G. (1999). Martensite in steel: strength and structure. Materials Science and Engineering: A, 273, 40.

[92] Giorgi, M.L., Durighello, P., Nicolle, R., & Guillot, J.B. (2004). Dissolution kinetics of iron in liquid zinc. Journal of Materials Science, 39(18), 5803.

[93] Rémazeilles, C., & Refait, P. (2007). On the formation of β-FeOOH (akaganéite) in chloride-containing environments. Corrosion Science, 49(2), 844.

[94] Volovitch, P., Allely, C., & Ogle, K. (2009). Understanding corrosion via corrosion product characterization: I. Case study of the role of Mg alloying in Zn–Mg coating on steel. Corrosion Science, 51(6), 1251.

[95] Volovitch, P., Vu, T.N., Allély, C., Aal, A.A., & Ogle, K. (2011). Understanding corrosion via corrosion product characterization: II. Role of alloying elements in

improving the corrosion resistance of Zn–Al–Mg coatings on steel. Corrosion Science, 53(8), 2437.

[96] Chowdhury, M., Mpongwana, N., Cummings, F., Fester, V., & Ntwampe, S. (2016). β-FeOOH/TiO_2 Heterojunction for Visible Light-Driven Photocatalytic Inactivation of E. coli. In Semiconductor Photocatalysis-Materials, Mechanisms and Applications. InTech.

[97] Yan, C., & Xue, D. (2008). Synthesis of designed templates for novel semiconductor materials with hollow structures. Functional Materials Letters, 1(01), 37.

[98] Wahab, R., Ansari, S. G., Kim, Y. S., Dar, M.A., & Shin, H.S. (2008). Synthesis and characterization of hydrozincite and its conversion into zinc oxide nanoparticles. Journal of Alloys and Compounds, 461(1-2), 66.

[99] De Giudici, G., Podda, F., Sanna, R., Musu, E., Tombolini, R., Cannas, C., & Casu, M. (2009). Structural properties of biologically controlled hydrozincite: An HRTEM and NMR spectroscopic study. American Mineralogist, 94(11-12), 1698.

[100] Cottis, R. A. (2001). Interpretation of electrochemical noise data. Corrosion, 57(3), 265.

[101] Song, G., Johannesson, B., Hapugoda, S., & StJohn, D. (2004). Galvanic corrosion of magnesium alloy AZ91D in contact with an aluminium alloy, steel and zinc. Corrosion Science, 46(4), 955.

[102] Naderi, M. (2008). Hot stamping of ultra high strength steels. Doctoral Theses, RWTH. Aachen.

[103] Tekkaya, A.E., Karbasian, H., Homberg, W., & Kleiner, M. (2007). Thermo-mechanical coupled simulation of hot stamping components for process design. Production Engineering, 1(1), 85.

[104] Hensen, G., et al., CHS^2 Conference Proceedings: Hot Sheet Metal Forming of High-Performance Steel, June 9-12, 2013, Luleå, Sweden.

[105] Fleischanderl, M., Kolnberger, S., Faderl, J., Landl, G., Raab, A.E., Brandstatter, W., Patent US20070256808, 2007.

[106] Kelsch, R., Sommer, A., Schwinghammer, H., Radlmayr, K., Kurz, T., Luckeneder, G., & Faderl, J., CHS^2 Conference Proceedings: Hot Sheet Metal Forming of High-Performance Steel, June 4-7, 2017, Atlanta, GA., USA.

[107] Muto, I., Sato, K., & Hara, N. (2010). Scanning Kelvin probe analysis of cut edge corrosion on prepainted galvanized steel with chromate-containing epoxy primer. ECS Transactions, 25(29), 59.

[108] Frankel, G.S. (2016). Fundamentals of corrosion kinetics. In Active Protective Coatings (pp. 17-32). Springer, Dordrecht.

[109] Zhang, Y.X., & Jia, Y. (2014). A facile solution approach for the synthesis of akaganéite (β FeOOH) nanorods and their ion-exchange mechanism toward As (V) ions. Applied Surface Science, 290, 102.

[110] Grosgogeat, B., Reclaru, L., Lissac, M., & Dalard, F. (1999). Measurement and evaluation of galvanic corrosion between titanium/Ti6Al4V implants and dental alloys by electrochemical techniques and auger spectrometry. Biomaterials, 20(10), 933-941.

[111] Cao, F.H., Zhang, Z., Su, J.X., Shi, Y.Y., & Zhang, J.Q. (2006). Electrochemical noise analysis of LY12-T3 in EXCO solution by discrete wavelet transform technique. Electrochimica Acta, 51(7), 1359.

Appendix A: Sample Preparation

Table A.1: Metallographic preparation for FE-SEM.

Surface	**Suspension**	**Lubricant**	**rpm**	**Force (N)**	**Time**
SiC paper, #320		Water	300	30	As needed
SiC paper, #600		Water	300	30	2 min
SiC paper, #1200		Water	Hand grinding*	Hand grinding	As needed
MD-Dac	Waterfree DP-Susp, 3 μm	DP-Blue	150	25	4 min
MD-Dur	Waterfree DP-Susp, 1 μm	DP-Blue	150	20	4 min
OP-Chem		1:1 OPS + ethylene glycol	150	15	40 s

*It should be noted that all grinding and polishing steps should be performed on an automatic polisher except for grinding with 1200 grit SiC paper. Instead, samples should be hand ground to maximise edge retention. The sample should be held such that the coating edge is held parallel to the grinding paper. Grinding should continue until no scratches from the previous grit can be seen under a light optical microscope (LOM), and until all scratches introduced from the 1200 grit SiC paper are in the same direction. It is also important to not overgrind or overpolish the samples as cracking of the coating may occur.

After each polishing step, samples were swabbed with a cotton ball soaked in ethanol, ultrasonicated in ethanol for 2 minutes on the edge of the mount, then blown dry with a hot air stream. After final polishing using OPS, samples were swabbed with a cotton ball soaked in ethylene glycol, ultransonicated in ethanol for 2 minutes on the edge of the mount, blown dry with a hot air stream, rinsed with isopropanol, then blown dry again with a hot air stream. It is of the utmost importance to ensure that no water comes into contact with the sample surface during polishing as water may cause corrosion of the coating.

These steps may be repeated to observe the microstructure of the substrate material, but as the Zn-layer is no longer of interest, it is not critical to remain waterfree. Etching should be done with 2% nital for a period of 5 s to reveal good contrast between the grains.

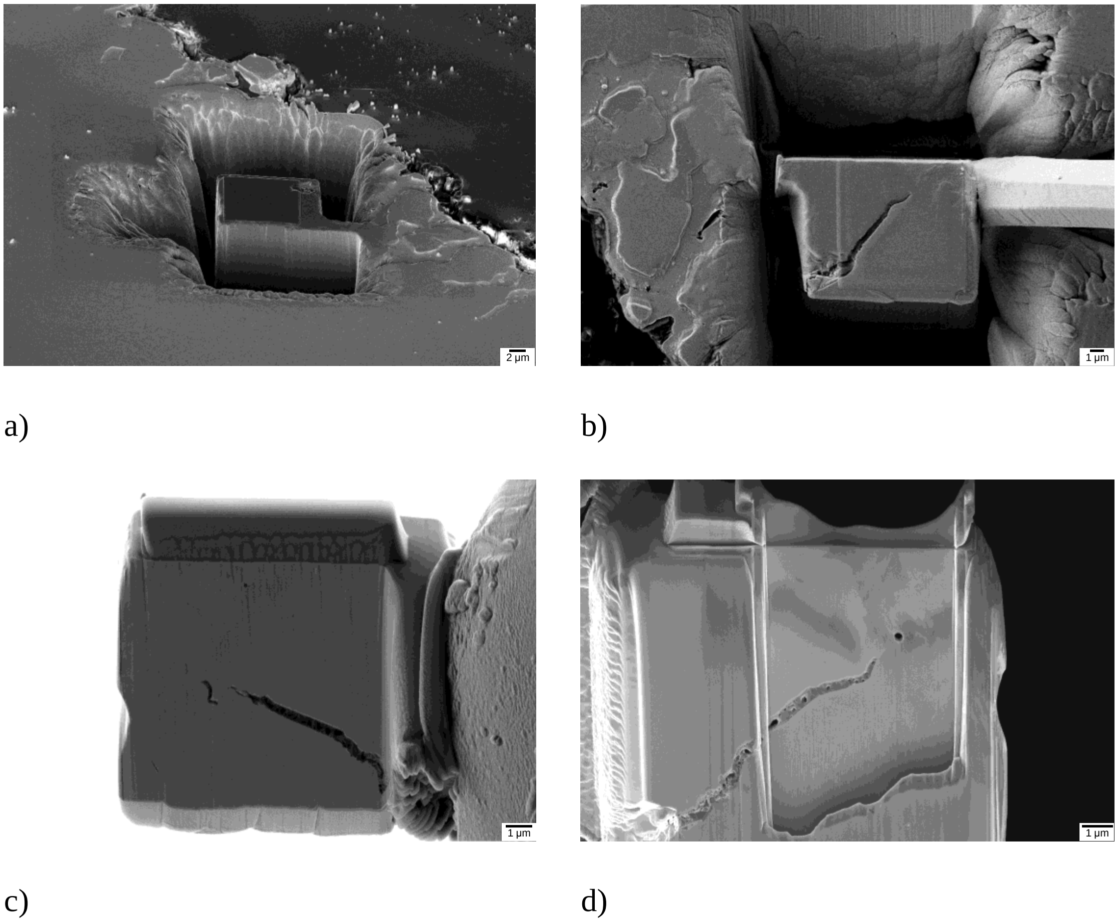

Figure A.1: FIB sample preparation stages of corroded sample depicting a) milling of trenches around area of interest, b) welding of sample to the probe, c) welding of sample to Cu grid and removal of probe, and d) sample thinning to produce electron transparent windows

Appendix B: Microstructural and Mechanical Properties

In order to determine the Zn content from the XRD data, the wt% of Zn within the phases needed to be calculated. These calculations are outlined in equations (B.1) and (B.2) for Γ-Fe_3Zn_{10} and ZnO, respectively. The wt% of Zn within α-Fe(Zn) was determined using the refined lattice parameter taken from the fitted curves using Rietveld refinement, and was determined to be 25 wt%. Here, M_{Zn} is the molar mass of Zn (65.38 g/mol), M_{Fe} is the molar mass of Fe (55.845 g/mol), and M_O is the molar mass of O (15.9994 g/mol).

$$wt\%\ Zn = \frac{10M_{Zn}}{10M_{Zn} + 3M_{Fe}} \tag{B.1}$$

$$wt\%\ Zn = \frac{M_{Zn}}{M_{Zn} + M_O} \tag{B.2}$$

Once the wt% of Zn within each phase had been determined, the Zn content for the corresponding microstructures could be calculated using equation (B.3). Here, $w_{\Gamma-Fe_3Zn_{10}}$, $w_{\alpha-Fe(Zn)}v_{\alpha-Fe(Zn)}$, and $w_{ZnO}v_{ZnO}$ correspond to the wt% of Zn within each phase as expressed above, $v_{\Gamma-Fe_3Zn_{10}}$ corresponds to the volume fraction of Γ-Fe_3Zn_{10} as determined by XRD, $v_{\alpha-Fe(Zn)}$ is the volume fraction of α-Fe(Zn) as determined by XRD, and v_{ZnO} is the volume fraction of ZnO as determined by XRD.

$$Zn\ content = w_{\Gamma-Fe_3Zn_{10}}v_{\Gamma-Fe_3Zn_{10}} + w_{\alpha-Fe(Zn)}v_{\alpha-Fe(Zn)} + w_{ZnO}v_{ZnO} \tag{B.3}$$

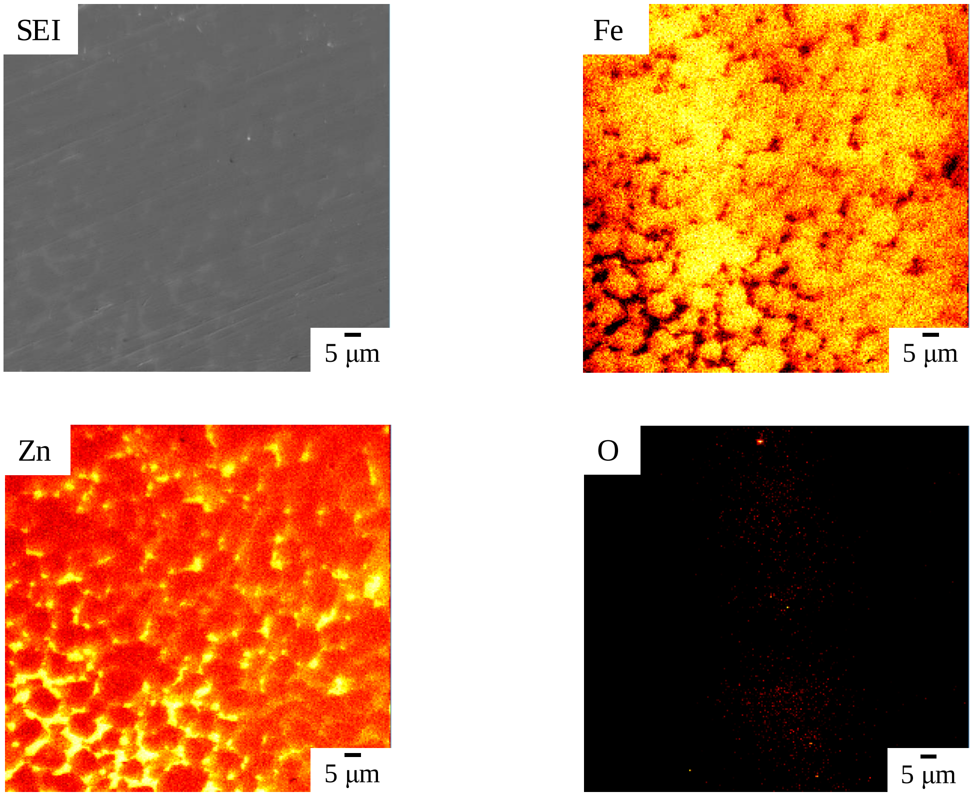

Figure B.1: SAM-AES elemental mapping of a GI70 sample annealed for 60 s at 900°C in plan view.

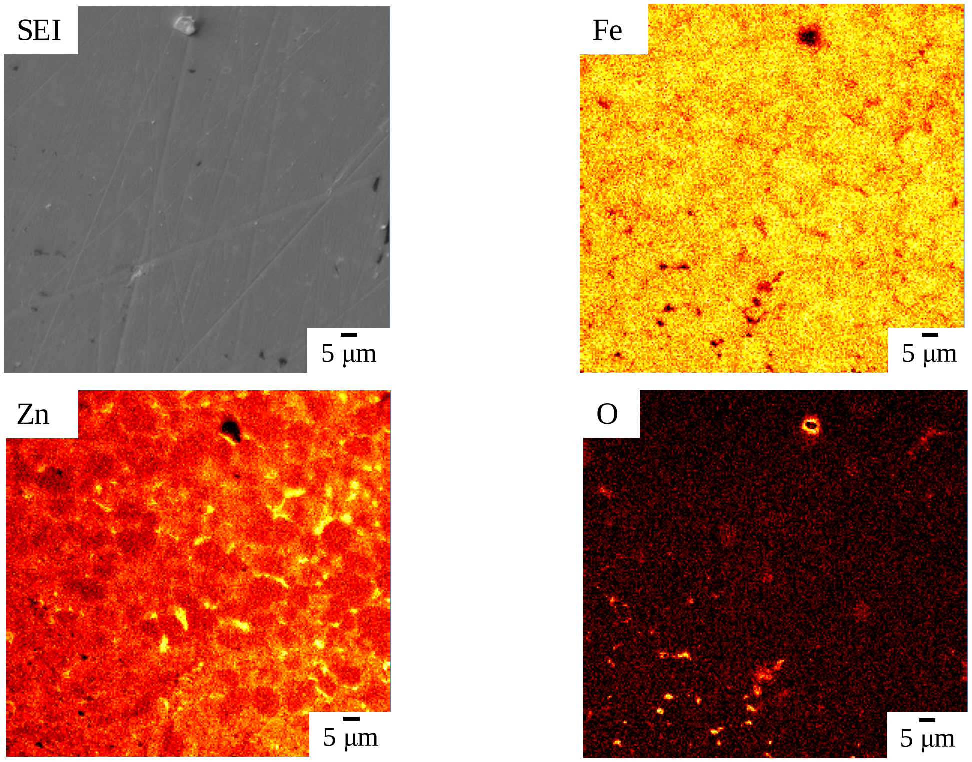

Figure B.2: SAM-AES elemental mapping of a GI70 sample annealed for 120 s at 900°C in plan view.

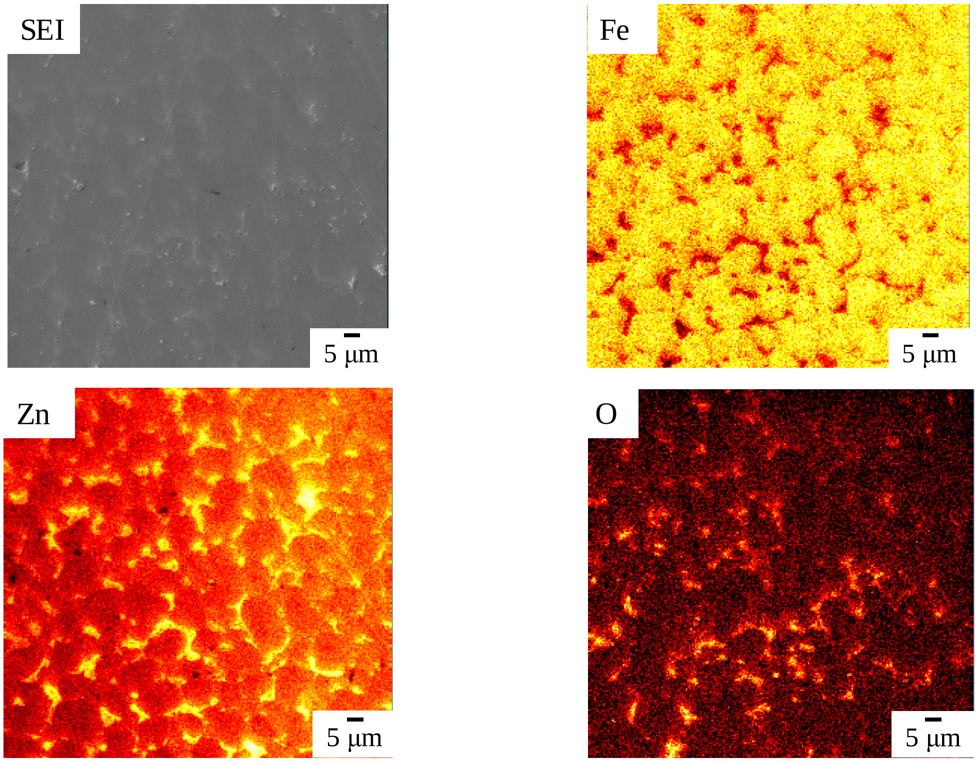

Figure B.3: SAM-AES elemental mapping of a GI70 sample annealed for 180 s at 900°C in plan view.

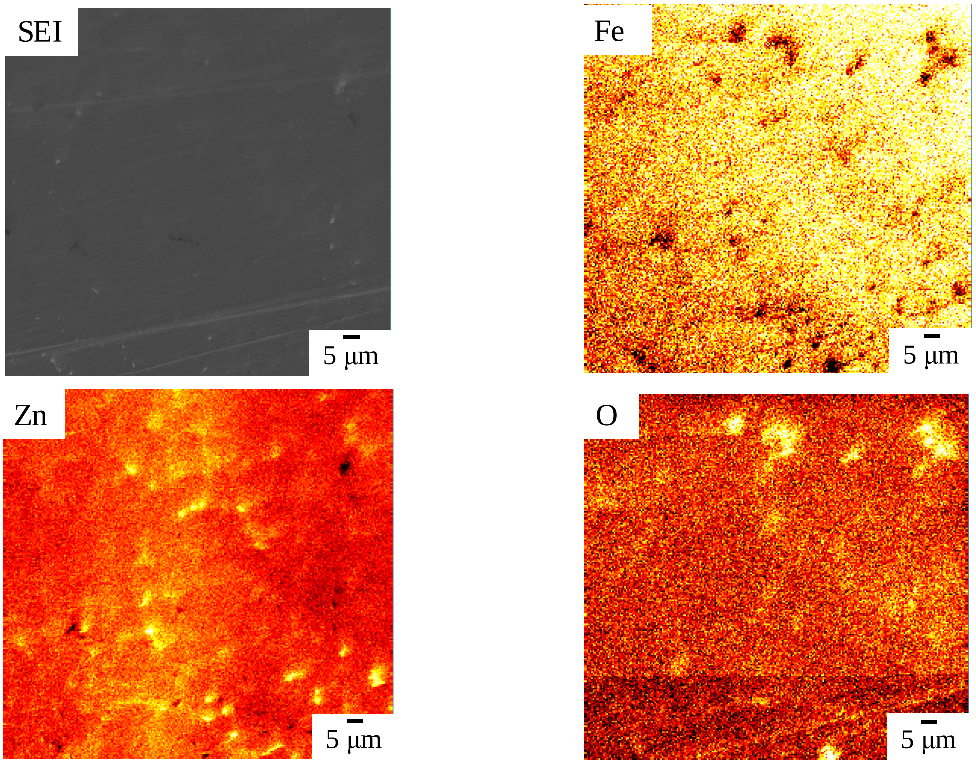

Figure B.4: SAM-AES elemental mapping of a GI70 sample annealed for 240 s at 900°C in plan view.

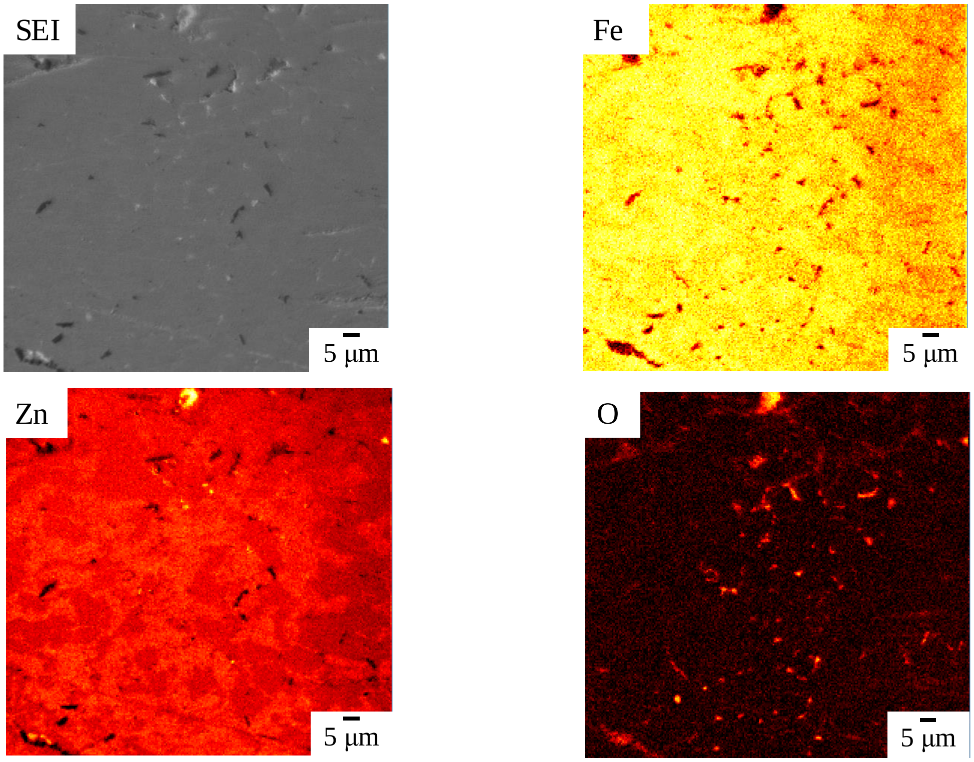

Figure B.5: SAM-AES elemental mapping of a GI70 sample annealed for 300 s at 900°C in plan view.

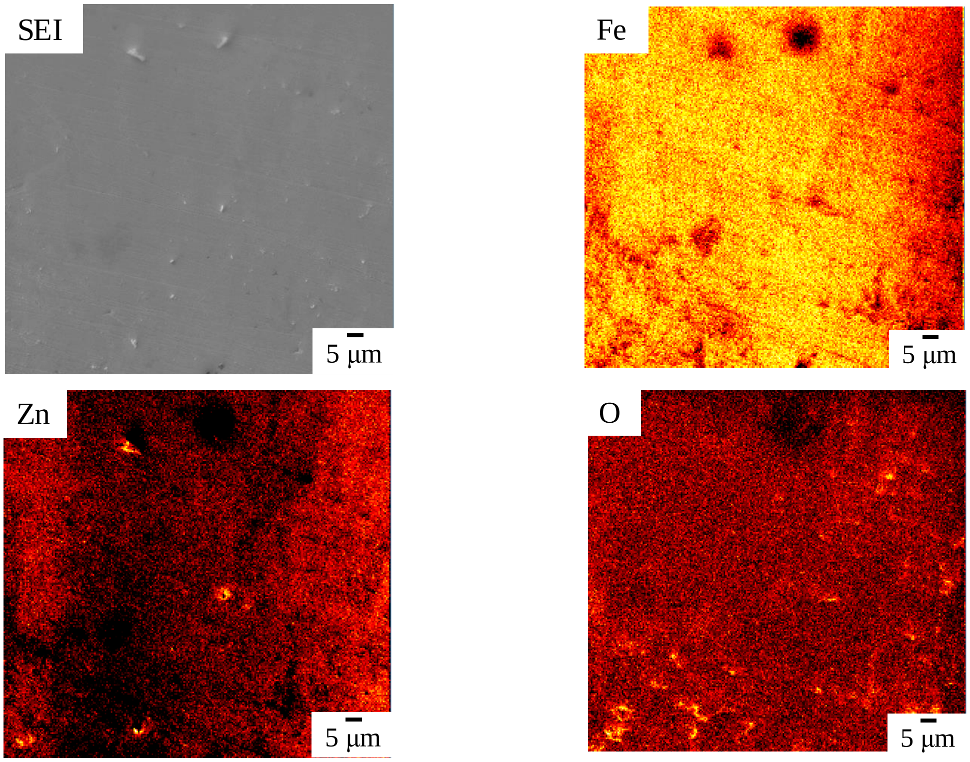

Figure B.6: SAM-AES elemental mapping of a GI70 sample annealed for 360 s at 900°C in plan view.

Appendix C: Electrochemical Polarization Measurements

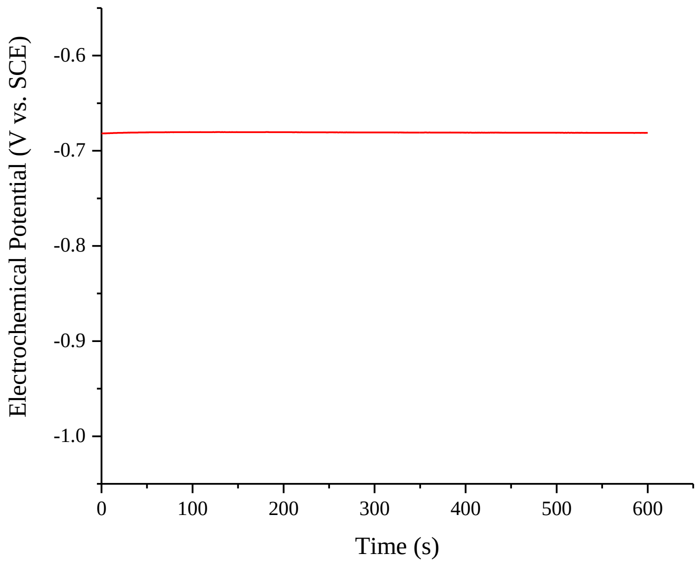

Figure C.1: OCP results for uncoated 22MnB5.

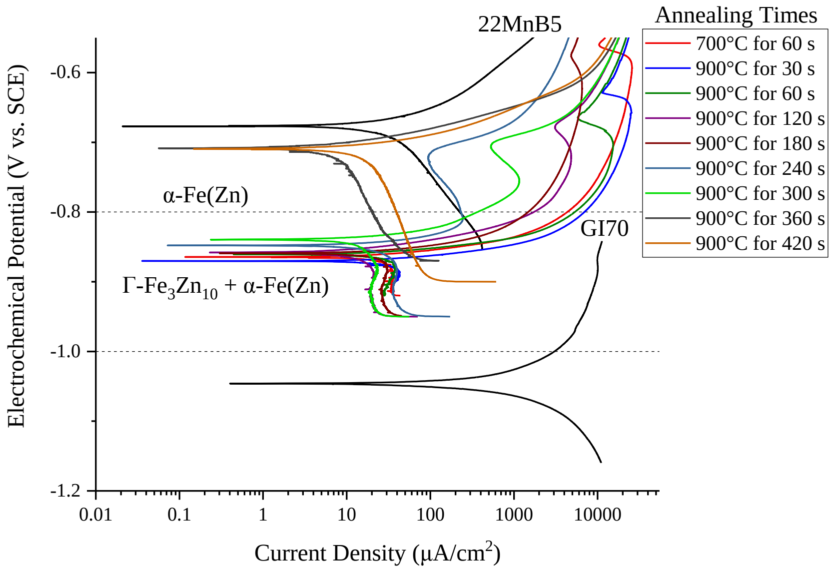

Figure C.2: Potentiodynamic polarization scans for all annealing times at 900°C.

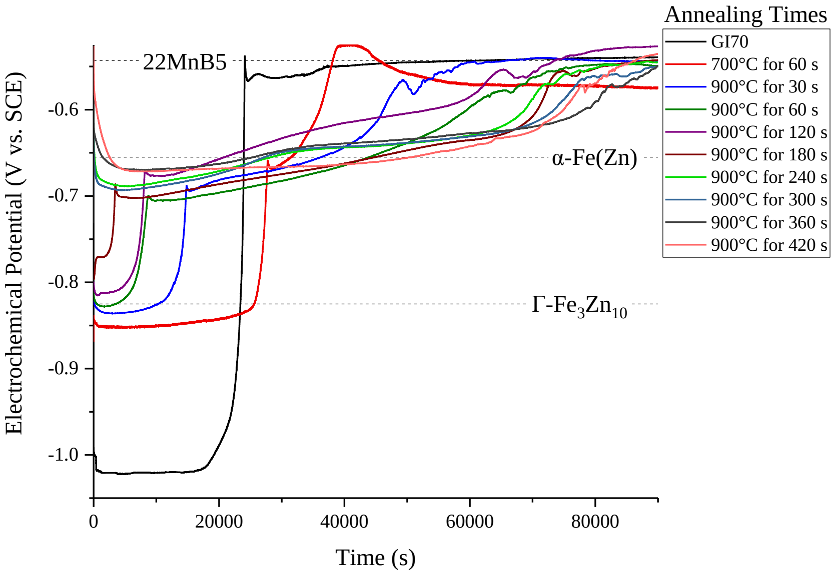

Figure C.3: Galvanostatic polarization transients at i = +1 mA/cm^2 for all annealing times at 900°C.

Appendix D: Electrochemical Properties

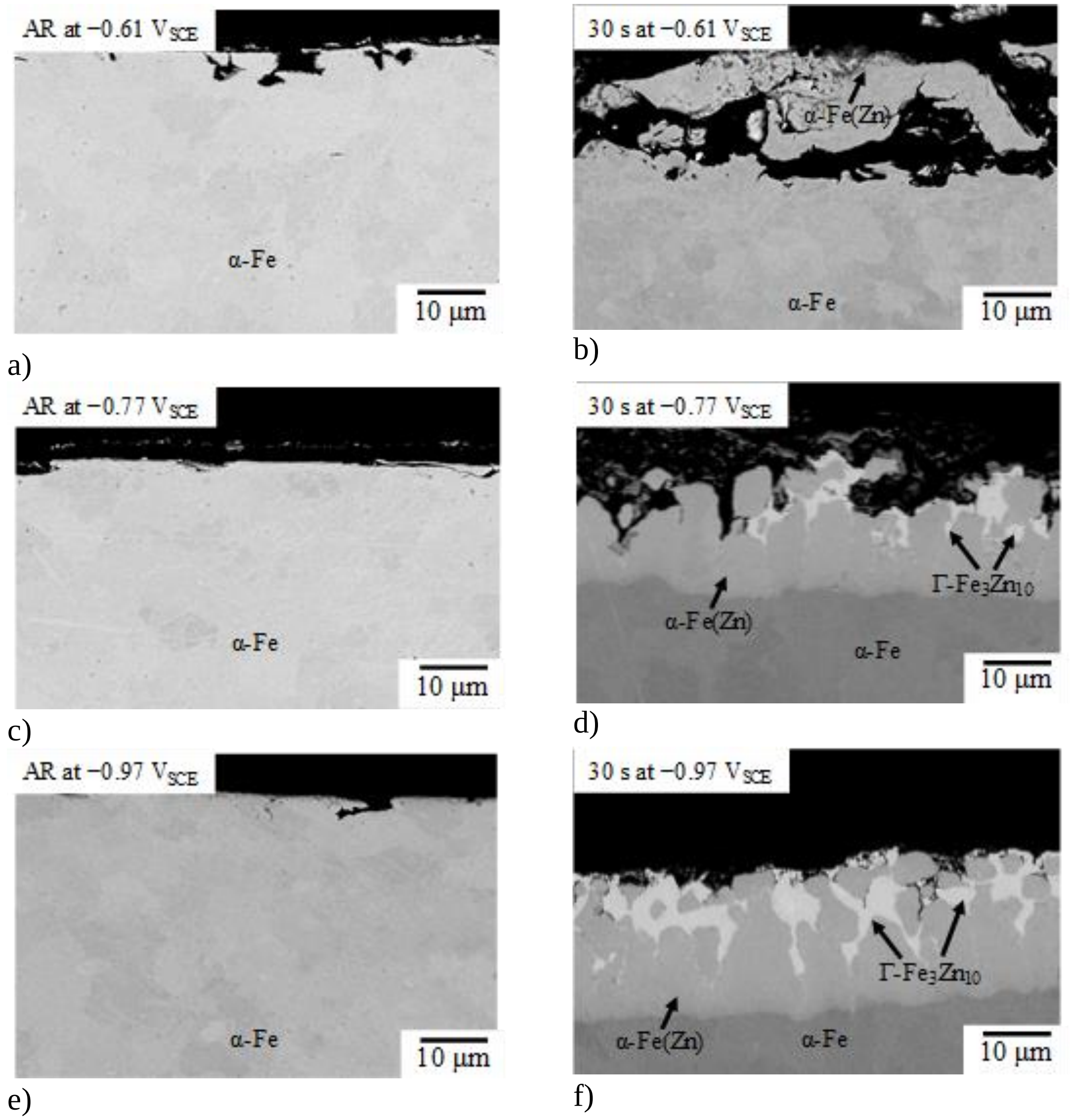

Figure D.1: Cross-sectional BSE SEM images after potentiostatic testing at for a a) AR GI70 sample held at −0.61 V$_{SCE}$, b) GI70 sample annealed at 900°C for 30 s held at −0.61 V$_{SCE}$, c) AR GI70 sample held at −0.77 V$_{SCE}$, d) GI70 sample annealed at 900°C for 30 s held at −0.77 V$_{SCE}$, e) AR GI70 sample held at −0.97 V$_{SCE}$, and f) GI70 sample annealed at 900°C for 30 s held at −0.97 V$_{SCE}$.

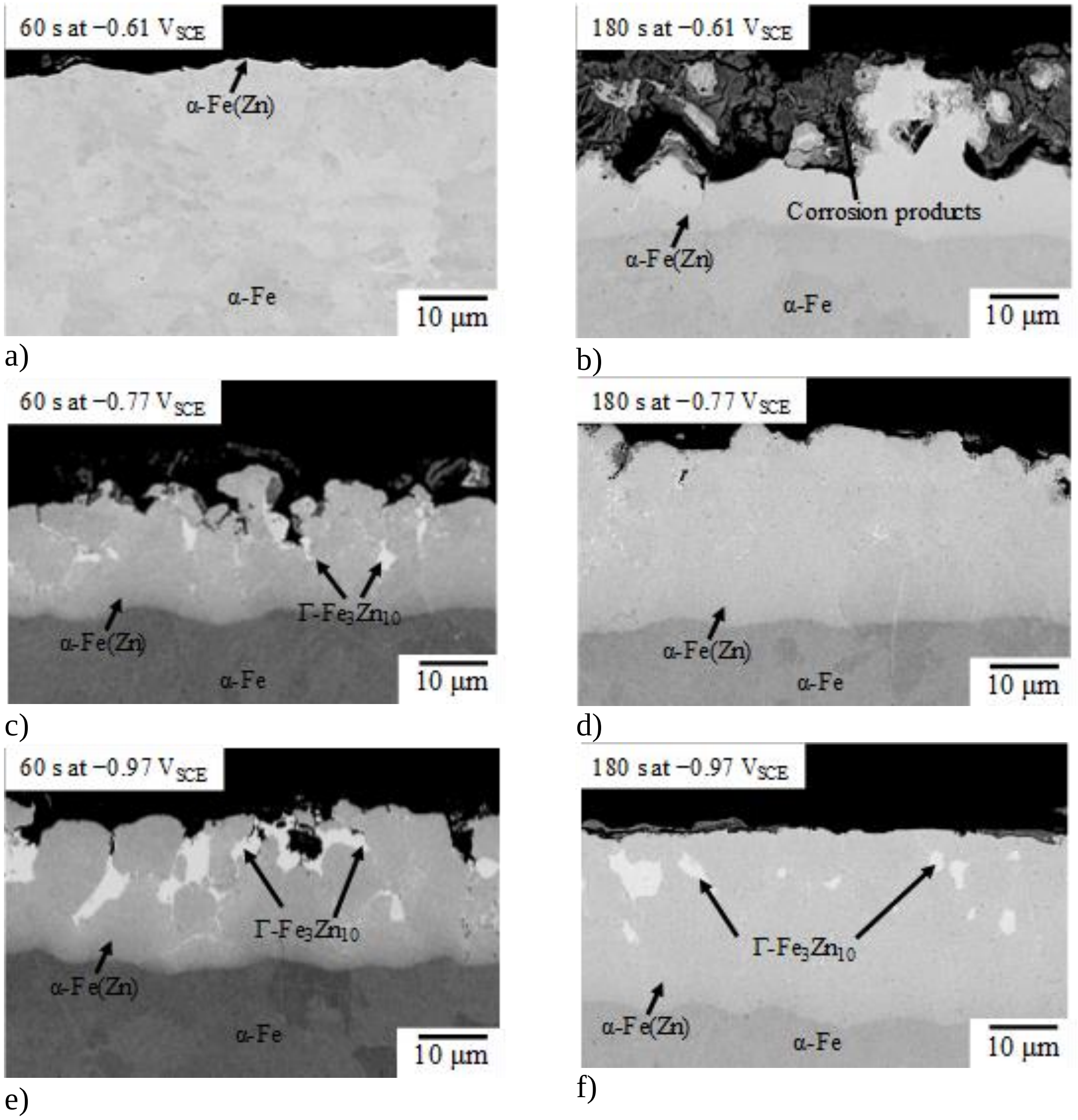

Figure D.2: Cross-sectional BSE SEM images after potentiostatic testing at for a a) GI70 sample annealed at 900°C for 60 s held at −0.61 V$_{SCE}$, b) GI70 sample annealed at 900°C for 180 s held at −0.61 V$_{SCE}$, c) GI70 sample annealed at 900°C for 60 s held at −0.77 V$_{SCE}$, d) GI70 sample annealed at 900°C for 180 s held at −0.77 V$_{SCE}$, e) GI70 sample annealed at 900°C for 60 s held at −0.97 V$_{SCE}$, and f) GI70 sample annealed at 900°C for 180 s held at −0.97 V$_{SCE}$.

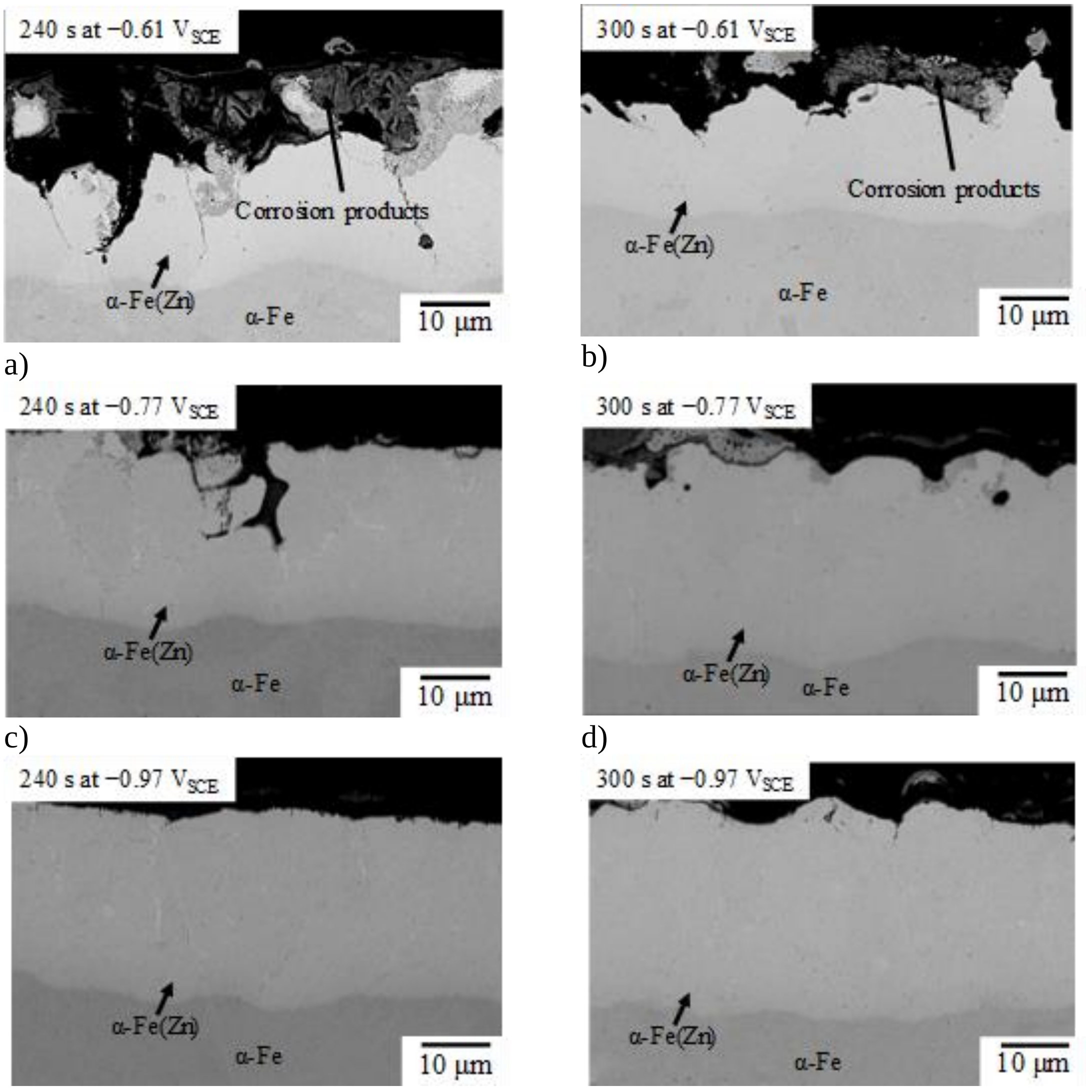

a) b)

c) d)

e) f)

Figure D.3: Cross-sectional BSE SEM images after potentiostatic testing at for a a) GI70 sample annealed at 900°C for 240 s held at −0.61 V_{SCE}, b) GI70 sample annealed at 900°C for 300 s held at −0.61 V_{SCE}, c) GI70 sample annealed at 900°C for 240 s held at −0.77 V_{SCE}, d) GI70 sample annealed at 900°C for 300 s held at −0.77 V_{SCE}, e) GI70 sample annealed at 900°C for 240 s held at −0.97 V_{SCE}, and f) GI70 sample annealed at 900°C for 300 s held at −0.97 V_{SCE}.

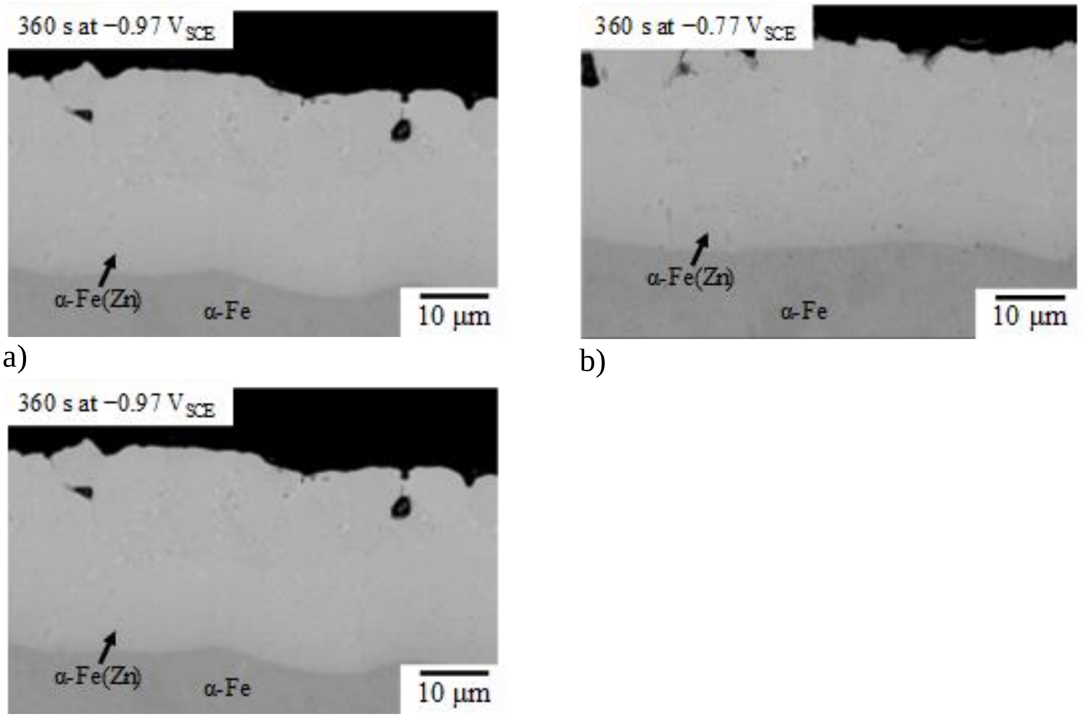

a)

b)

c)

Figure D.4: Cross-sectional BSE SEM images after potentiostatic testing at for a a) GI70 sample annealed at 900°C for 360 s held at −0.61 V_{SCE}, b) GI70 sample annealed at 900°C for 360 s held at −0.77 V_{SCE}, c) GI70 sample annealed at 900°C for 360 s held at −0.97 V_{SCE}.

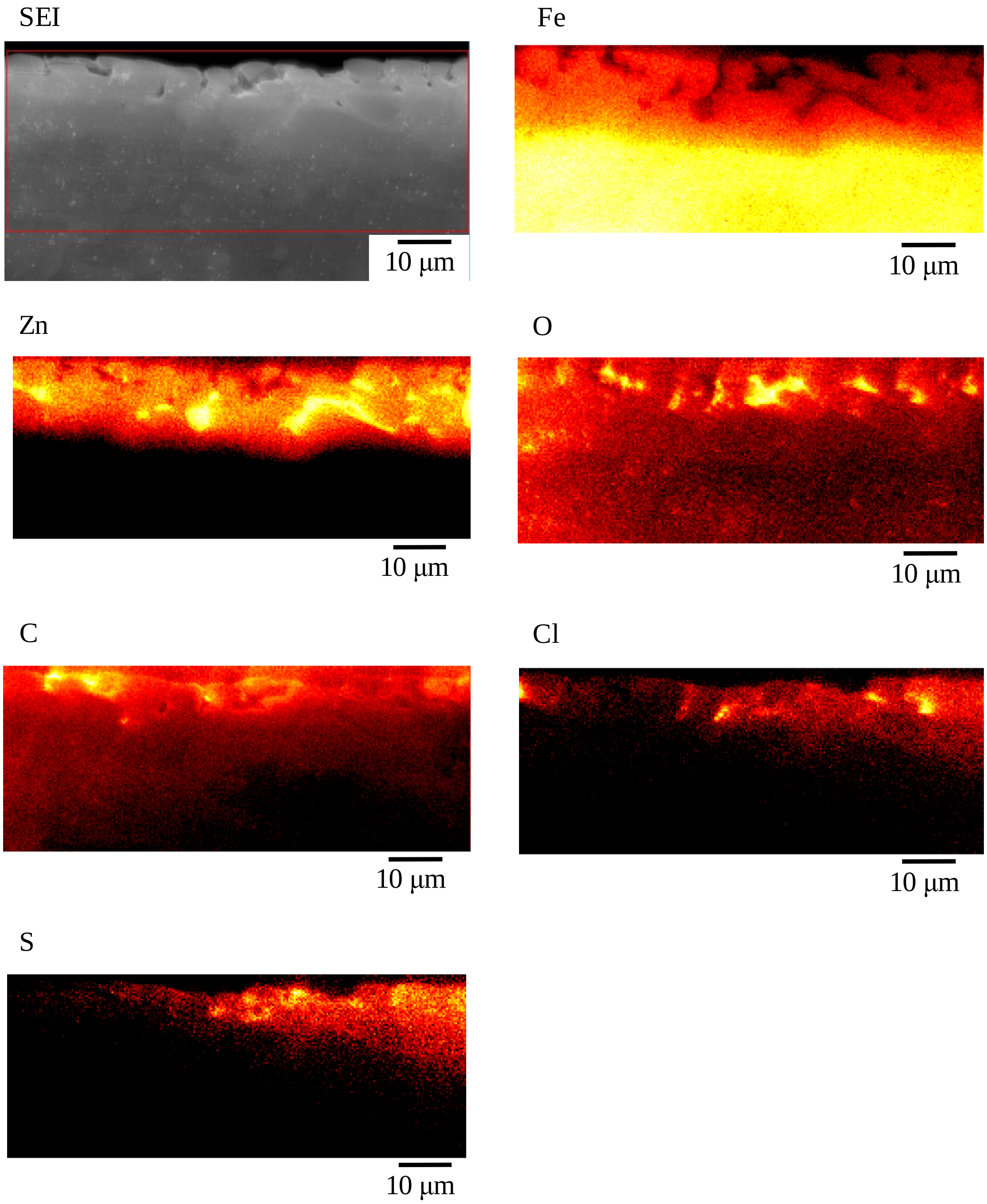

Figure D.5: Cross-sectional view SAM-AES map images of GI70 sample annealed at 900°C for 60 s.

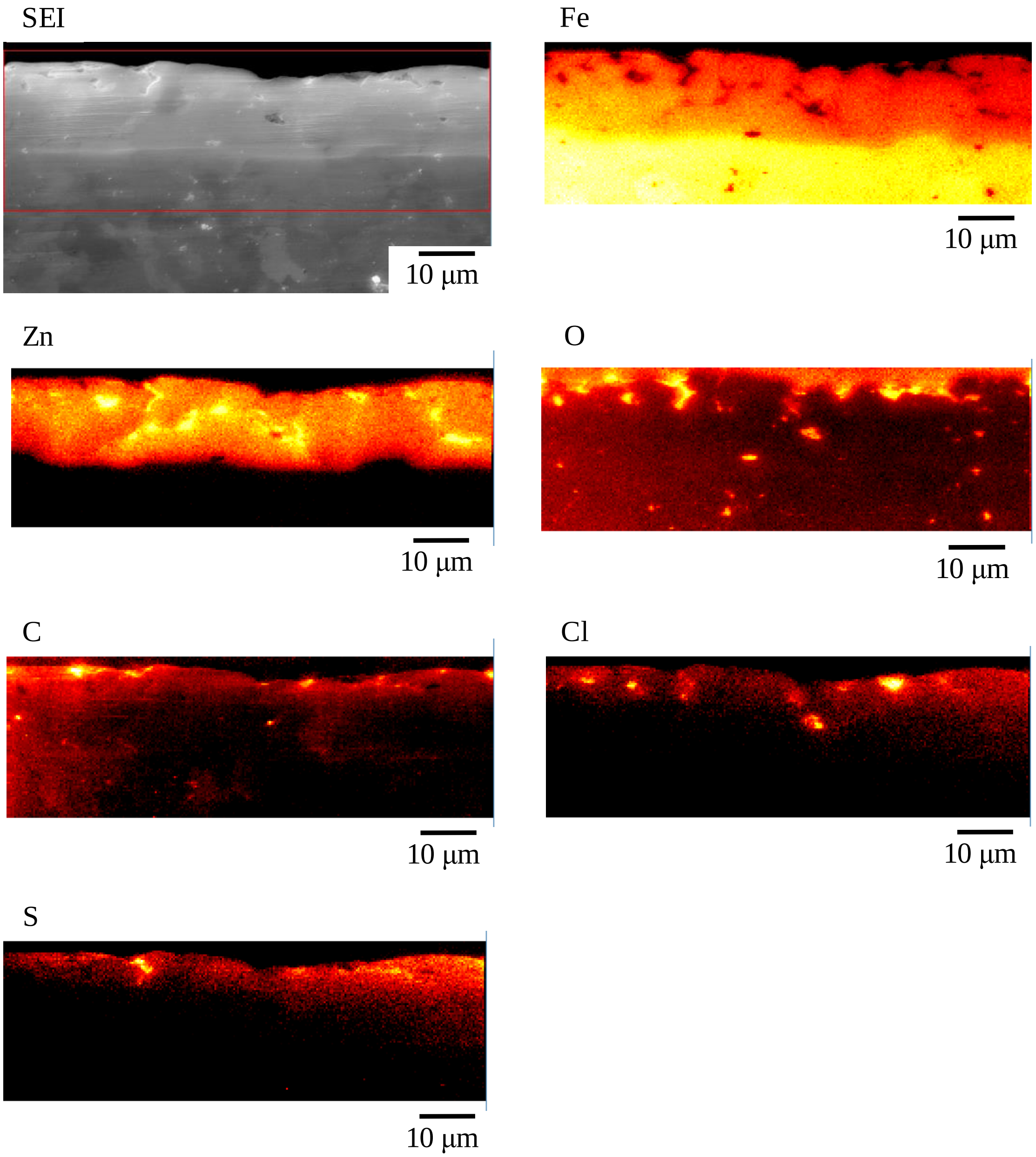

Figure D.6: Cross-sectional view SAM-AES map images of GI70 sample annealed at 900°C for 120 s.

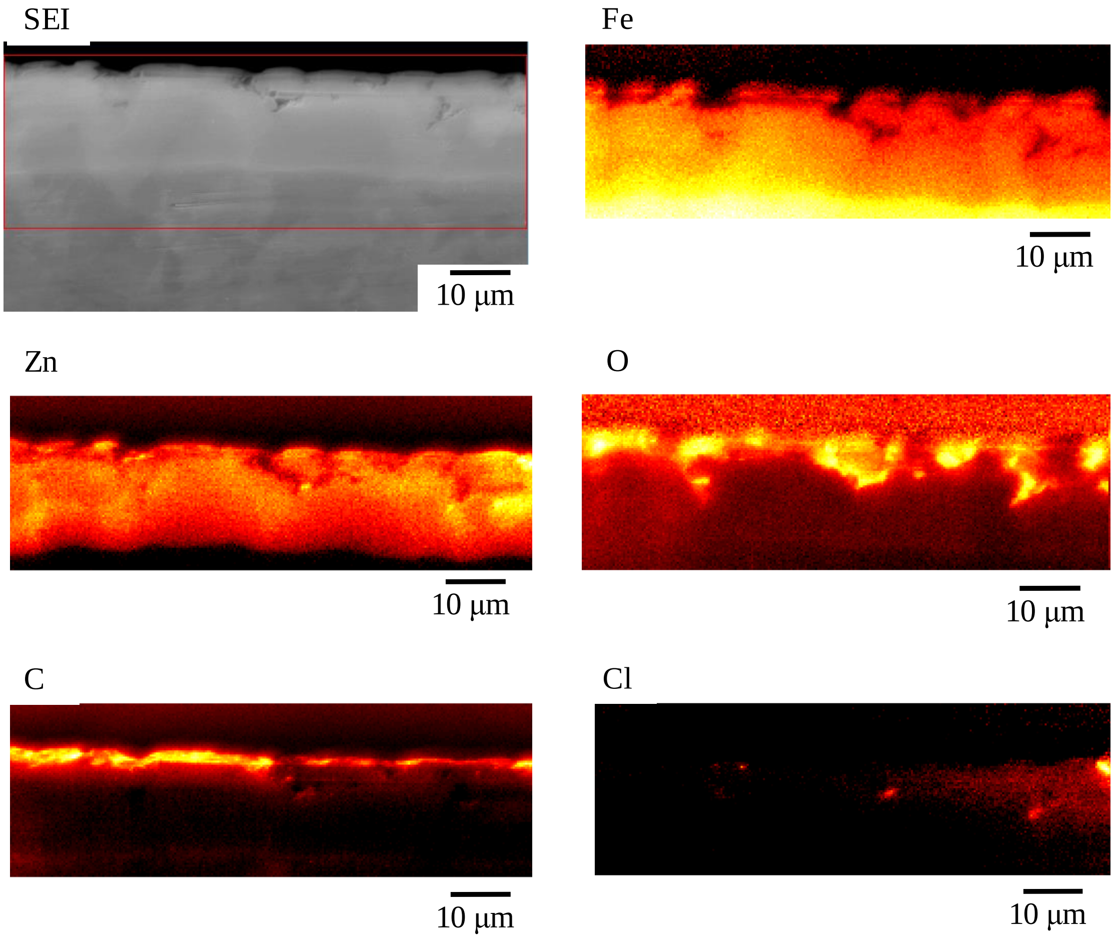

Figure D.7: Cross-sectional view SAM-AES map images of GI70 sample annealed at 900°C for 180 s.

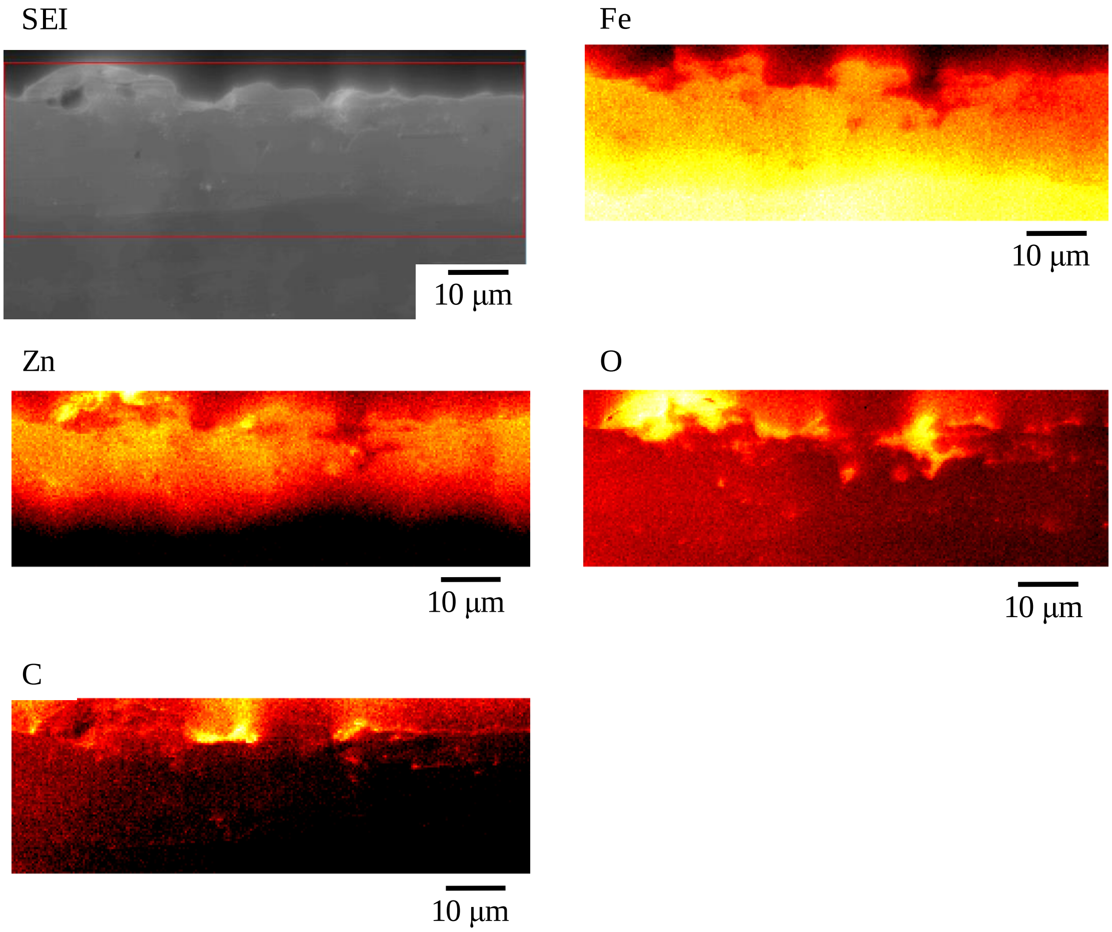

Figure D.8: Cross-sectional view SAM-AES map images of GI70 sample annealed at 900°C for 300 s.

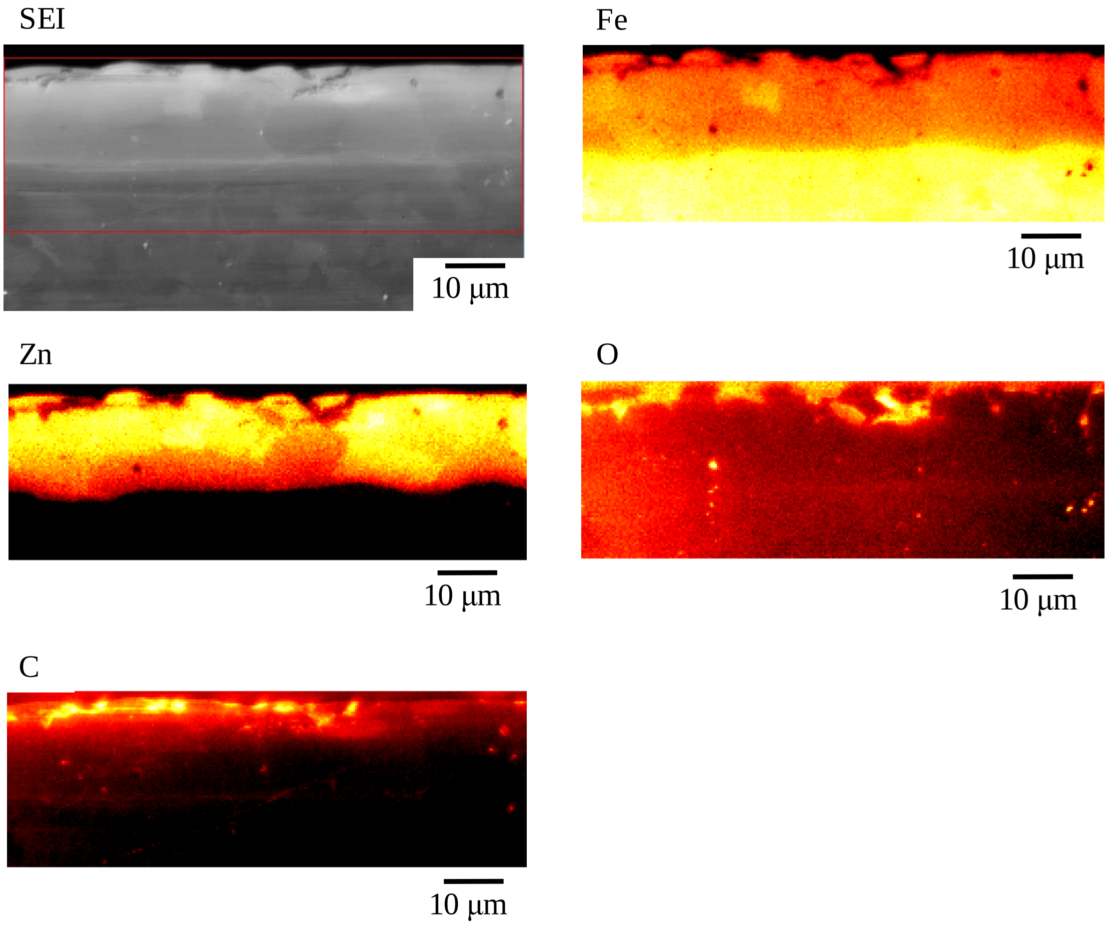

Figure D.9: Cross-sectional view SAM-AES map images of GI70 sample annealed at 900°C for 360 s.

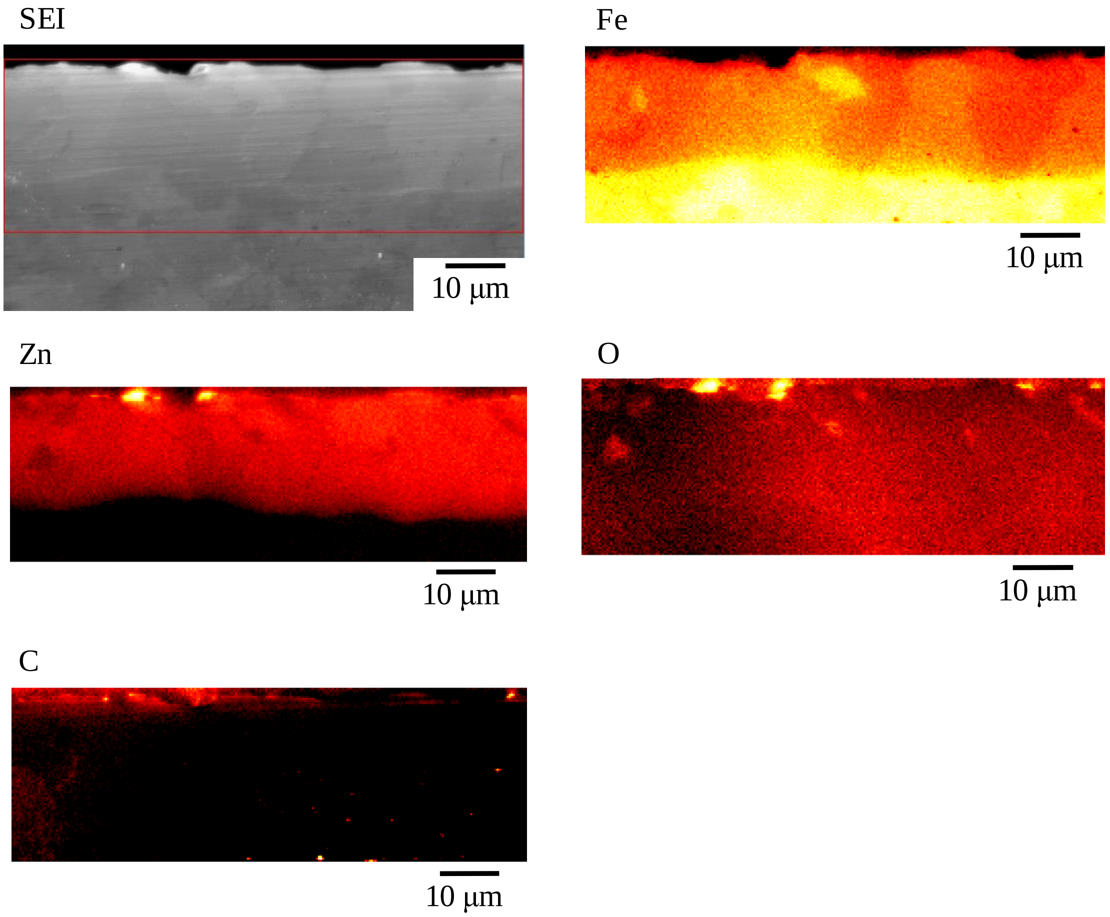

Figure D.10: Cross-sectional view SAM-AES map images of GI70 sample annealed at 900°C for 420 s.

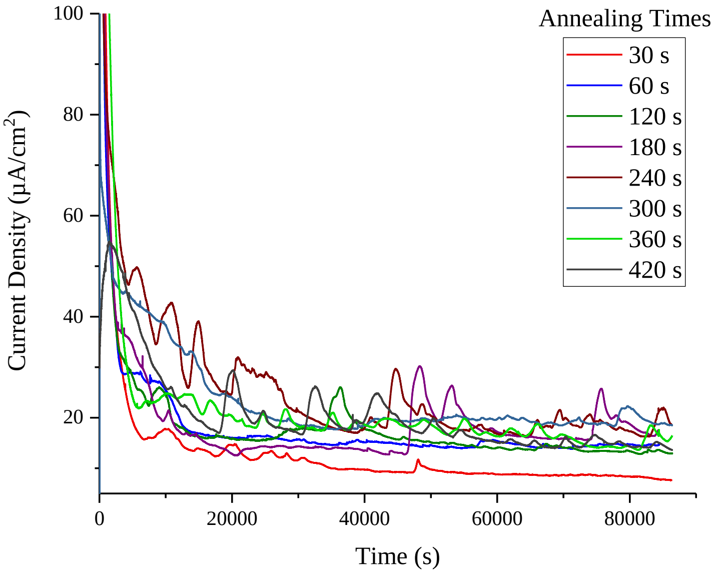

Figure D.11: Galvanic corrosion scans for all annealing times at 900°C.